GNSS Integrity Monitoring assisted by Signal Processing techniques in Harsh Environments

ScuDo
Scuola di Dottorato ~ Doctoral School
WHAT YOU ARE, TAKES YOU FAR

Doctoral Dissertation
Doctoral Program in Electronics Engineering (29^{th}cycle)

GNSS Integrity Monitoring assisted by Signal Processing techniques in Harsh Environments

By

Mattia Berardo

******

Supervisor(s):
Prof. Letizia Lo Presti, Supervisor

Doctoral Examination Committee:
Olivier Julien, Referee, ENAC (Ecole Nationale de l'Aviation Civile)
Robert Eric Phelts, Referee, Stanford University
Prof. Fabio Dovis, Polytechnic of Turin
Prof. Gustavo Belforte, Polytechnic of Turin
Prof. Ernestina Cianca, University of Rome Tor Vergata

Politecnico di Torino
2017

Declaration

I hereby declare that, the contents and organization of this dissertation constitute my own original work and does not compromise in any way the rights of third parties, including those relating to the security of personal data.

Mattia Berardo
2017

* This dissertation is presented in partial fulfillment of the requirements for **Ph.D. degree** in the Graduate School of Politecnico di Torino (ScuDo).

I would like to dedicate this thesis to my parents, my sister and Maria

Hic Sunt Leones
[Latin phrase used by ancient Roman and Medieval cartographers]

Acknowledgements

The author would like to express his gratitude to all of those who supported him during the Ph.D. program. Without the contribution of nice and smart people at Politecnico di Torino, this work would have not been possible. The author will never forget the opportunity of the great experience at the Stanford University. I would like to thank Prof. Letizia Lo Presti as the advisor of this work, gave the author the opportunity to be a member of the NavSAS group. Another special thanks goes to my colleagues, other PhD students, in particular to Esteban Garbin Manfredini and Hieu Tran Trung for the collaboration and Dr.Gianluca Falco for his precious suggestions. Finally, I would like to thank the NavSAS group also for the beautiful moments and the nice soccer match done during the PhD period.

Thanks to all the Stanford staff, in particular Sam Pullen, for suggestions and comments to the work.

The author wish to thank Ansaldo STS which supports this research work.

Un ringraziamento anche agli amici del treno per tutte le mattine passate da pendolari ae per le belle possibilità di confronto e divertimento. Un ringraziamento lo dedico alla mia famiglia e alla mia ragazza Maria per il loro prezioso sostegno.

Abstract

The Global Navigation Satellite Systems (GNSS) applications are growing and more pervasive in the modern society. The presence of multi-constellation GNSS receivers able to use signals coming from different systems like the american Global Positioning System (GPS), the european Galileo, the Chinese Beidou and the russian GLONASS, permits to have more accuracy in position solution. All the receivers provide always more reliable solution but it is important to monitor the possible presence of problems in the position computation. These problems could be caused by the presence of impairments given by unintentional sources like multipath generated by the environment or intentional sources like spoofing attacks.

In this thesis we focus on design algorithms at signal processing level used to assist Integrity operations in terms of Fault Detection and Exclusion (FDE). These are standalone algorithms all implemented in a software receiver without using external information. The first step was the creation of a detector for correlation distortion due to the multipath with his limitations. Once the detection is performed a quality index for the signal is computed and a decision about the exclusion of a specific Satellite Vehicle (SV) is taken. The exclusion could be not feasible so an alternative approach could be the inflation of the variance of the error models used in the position computation. The quality signal can be even used for spoofing applications and a novel mitigation technique is developed and presented. In addition, the mitigation of the multipath can be reached at pseudoranges level by using new method to compute the position solution.

The main contributions of this thesis are: the development of a multipath, or more in general, impaiments detector at signal processing level; the creation of an index to measure the quality of a signal based on the detector's output; the

description of a novel signal processing method for detection and mitigation of spoofing effects, based on the use of linear regression algorithms; An alternative method to compute the Position Velocity and Time (PVT) solution by using different well known algorithms in order to mitigate the effects of the multipath on the position domain.

Contents

List of Figures

List of Tables

List of Acronyms

ADC Analog to Digital Converter

AL Alarm Limit

AMCS Alternate Master Control Station

AWGN Additive White Gaussian Noise

BDE Barycenter Delay Estimation

BOC Binary Offset Code

BPSK Binary Phase Shift Key

CDMA Code Division Multiple Access

C/A Coarse/Acquisition

CAF Cross Ambiguity Function

CDF Cumulative Density Function

CLS Constraint Least Square

CS Commercial Service

DLL Delay Lock Loop

DoD Department of Defense

DOF Degree Of Freedom

DOP Dilution of Precision

DoT Department of Transportation

DTFT Discrete-Time Fourier Transform

ECEF Earth-Centered Earth Fixed

EGNOS European Geostationary Navigation Overlay System

ENU East-North-Up

FAA Federal Aviation Administration

FD Fault Detection

FDE Fault Detection and Exclusion

FDMA Frequency Division Multiple Access

FFT Fast Fourier Transform

FIR Finite Impulse Response

FOC Full Operational Capability

GA Ground Antennas

GAGAN GPS Aided Geo Augmented Navigation

GBAS Ground-Based Augmentation System

GCC Ground Control Center

GCS Ground Control Segment

GDOP Geometric Dilution of Precision

GNSS Global Navigation Satellite Systems

GPS Global Positioning System

GPS L1 C/A GPS L1 Coarse/Acquisition

GSS Galileo Sensor Stations

HPE Horizontal Position Error

HPL Horizontal Protection Level

IF Intermediate Frequency

IR Integrity Risk

ITU International Telecommunication Union

JPO Joint Program Office

KF Kalman Filter

LAAS Local Area Augmentation System

LAF Linear Adaptive Filter

LFSR Linear Feedback Shift Register

LASSO Least Absolute Shrinkage and Selection Operator

LHCP Left Hand Circularly Polarized

LOS Line Of Sight

LS Least Squares

LMS Least Mean Squares

MEDLL Multipath Estimating Delay Lock Loop

MEO Medium Earth Orbit

MP Multipath

MPDD Multipath Distance Detector

MCS Master Control Station

MEO Medium Earth Orbit

MS Monitoring Station

MSAS Multi-functional Satellite Augmentation System

MSE Mean Square Error

MSR Multipath to Signal Ratio

NASA National Aeronautics and Space Administration

OS Open Service

PAM Pulse Amplitude Modulation

PL Protection Level

PLL Phase Lock Loop

PDF Probability Density Function

PRN Pseudo Random Noise

PRS Public Regulated Service

PVT Position Velocity and Time

PPS Precise Positioning Service

QAM Quadrature Amplitude Modulation

RAIM Receiver Autonomous Integrity Monitoring

RF Radio-Frequency

RINEX Receiver Independent Exchange Format

RHCP Right Hand Circularly Polarized

RNP Required Navigation Performance

ROC Receiver Operating Characteristic

SAR Search And Rescue

SBAS Satellite-Based Augmentation System

SDR Software-Defined Radio

SIS Signal In Space

SNR Signal-to-Noise Ratio

SoL Safety of Life

SPS Standard Positioning Service

SQI Signal Quality Index

SQM Signal Quality Monitoring

SV Satellite Vehicle

TEXBAT Texas Anti Spoofing Test Battery

TJ Time Jumper

TOA Time Of Arrival

TTA Time To Alert

UERE User Equivalent Range Error

UHF Ultra High Frequency

VHF Very High Frequency

VPE Vertical Position Error

VPL Vertical Protection Level

WAAS Wide Area Augmentation System

WGN White Gaussian Noise

WLS Weighted Least Squares

Introduction

The research topic addressed in this PhD thesis is part of the research activities of Ansaldo STS, member of the Joint Undertaking (JU) shift2rail [1], for the renewal of the European rail signaling system. Ansaldo STS fully funded this PhD with the aim of investigating innovative techniques to ensure the integrity of position information provided by GNSS. In fact, it is known that the Innovation Programme 2 of shift2raiII includes the innovative use of the GNSS for train localization. It is therefore vital to ensure that this data is reliable. This same subject has been investigated for many years in aviation, but it is known that the techniques developed in that environment cannot be applied to the rail environment, which is very different, especially for the presence of multipath typical of land applications. In addition, the techniques described in the literature generally relate to the data provided by a commercial GNSS receiver, while in this thesis we want to explore the possibility of performing signal integrity checks at the correlation stage of a GNSS receiver by using signal processing methods. The funding of Ansaldo STS is specifically devoted to this kind of innovative methods of integrity, in view of the future development of GNSS ad hoc receivers for rail applications. An important contribution to this work has been done during a study period in GPS Research Lab in Stanford University, which cooperates with Ansaldo in topics related to train localization. In the remainder of the thesis we have considered a generic land environment affected by multipath and the main topic has been to investigate integrity techniques especially tailored to degraded environment.

GNSS systems were developed to provide positioning information to the users. These information, due to several impairments given by the environments, interference etc. could not be accurate. This thesis describes the work done during my PhD program, in the context of signal processing used to assist

Integrity operations in terms of FDE. Usually the problem of the faults detection is faced by specific algorithms called Receiver Autonomous Integrity Monitoring (RAIM). These algorithms work, for example, by searching possibles biases between the set of the satellites pseudoranges, verifying the consistency of the measurements. Another kind of measurements used for the detection purpose is in the position domain. In that case, several navigation solutions are computed by excluding different satellites from the solution to identify the possible bias so finding the fault free set of satellites.

The first step of this work has been the analysis of the RAIM algorithms proposed in literature and presented in the thesis. The second step consisted in the the adaptation or creation of signal processing techniques tailored to impairment detection. To approach this problem, different aspects of the GNSS receiver have been studied during the PhD.

The context considered in my work is for applications where the presence of environmental effects, like the MP, could affect the receiver in terms of accuracy, integrity, continuity or availability of the service. The considered architecture is a specific software receiver focused on the peculiarity of the land environment so, to have several rays coming from different directions to the receiver.

To provide better information for FDE, the output of the detector was integrated with others information to build a sort of quality index for the incoming signals. The exclusion is another important aspect investigated after the definition of a signal quality metric. The exclusion after the fault identification could give problems with lower number of SVs in view. The exclusion of a SV has always effect on the quality of the geometry. Especially in case of weak geometry, the exclusion of SVs from the navigation solution could be a source of error greater than the error given by possible detected distortions. A proposed solution is given.

The use of a quality metric based on correlation measurements can be useful in other contexts, for instance, scenarios where a spoofing attack is present. For this reason, the purpose of a part of the work is to use the metric that can be helpful to detect the spoofer and permit to exclude spoofed satellites. A detection scheme is also supported by a mitigation mechanism.

As already mentioned, MP can affect the navigation solution by providing a bias on the position. In this work, a comparison between the RAIM consistency tests based on Kalman Filter (KF) and LS in a MP environment was done. An algorithm is proposed to mitigate the effect of MP on the position solution.

Thesis outline

The thesis is organized as follows:

- The Chapter 1, a brief history of the GNSS technologies is given. Then, the chapter presents the working principles of the positioning systems, the signal structure of the GPS and Galileo systems and the general architecture of the GNSS receivers.
- In the Chapter 2 a general overview on the integrity concepts is provided. What is the integrity and main terms are introduced.
- The Chapter 3 is devoted to the presentation of the theory of the signal processing techniques used in this thesis for distortions detection. Then, the algorithm for the detection of MP is shown.
- In the Chapter 4, by using the output of the detector, a metric that evaluates the quality of the received signals is given. Potentially, this metric is used to perform exclusion of satellites with signals strongly degraded.
- In Chapter 5 the previous metric is used for the detection in case of a spoofing attack scenario. After the detection, a complete mitigation algorithm is presented.
- Chapter 6 shows some results about the comparison of the positioning and fault detection based on RAIM algorithm, computed by LS and KF in harsh environments. A hybrid approach is proposed.

Publications arising from this thesis

- M. Berardo and L. Lo Presti. "GNSS multipath detector based on linear adaptive filter". In Proceedings of the 28th International Technical Meeting of The Satellite Division of the Institute of Navigation (ION GNSS+ 2015), Tampa, Florida, pages 3077–3083, 2015.
- M. Berardo and S. Ugazio. "Multipath distance detector algorithm (MPDD): Enhancement and application to Galileo signals". In 2016 IEEE Metrology for Aerospace (MetroAeroSpace), pages 579–584, June 2016.
- M. Berardo and L. Lo Presti. "On the use of a signal quality index applying at tracking stage level to assist the RAIM system of a GNSS receiver". Sensors, 16(7):1029, 2016.
- M. Berardo, E. G. Manfredini, F. Dovis and L. Lo Presti, "A spoofing mitigation technique for dynamic applications," 2016 8th ESA Workshop on Satellite Navigation Technologies and European Workshop on GNSS Signals and Signal Processing (NAVITEC), Noordwijk, 2016, pp. 1-7. doi: 10.1109/NAVITEC.2016.7849353
- H. Trung Tran , M. Berardo , G. Belforte , L. Lo Presti, "Hybrid method for multipath-resiliant PVT determination using Kalman filter based algorithms", under review.

Chapter 1

Overview on GNSS systems

In the recent history, the concept of GNSS was born. GNSS is a term denoting a system based on the use of satellites for navigation purposes. Typically, GNSS indicates systems having a 24 hours coverage over the globe. GNSS is a fundamental part of the space industries of the world. The use of these systems is getting more important in the modern life from Safety of Life (SoL) applications to simple smartphone applications. The first and most famous satellite system is the American one: GPS. During the time other navigation systems were born around the world: the Russian GLONASS, the European Galileo, the Chinese Beidou etc. There are also regional systems which have not a global coverage but only specific geographical part of the planet.

1.1 History of Global Navigation Satellite Systems

In the early 1960s, U.S. Department of Defense (DoD), the National Aeronautics and Space Administration (NASA) and the Department of Transportation (DoT) were interested in building a satellite system for position determination. They needed a global, all-weather, 24-hour coverage and accuracies positioning and navigation system [2]. The NAVSTAR GPS was the answer to those requirements, the successor of other positioning system: US TRANSIT. It was realized with four to seven satellites in low-altitude polar orbits. It became

operational in 1964. However, due to its limitation, it has been necessary to develop another satellite navigation system. Before arriving to GPS, the U.S. Navy worked on a project to enhance the performance of TRANSIT and, at the same time, the U.S Air Force worked on a new satellite based positioning system called 621B [3]. 621B proposed for the first time the use of PRN modulation for ranging with digital signals. The GPS inherits the idea to use the PRN code. The main differences between some of these systems are shown in Table 1.1 [4]. The GPS program was approved in December 1973 and it was developed by the

Characteristic	Timation	621B	GPS
N. of SV	27	3 or 4 groups of 5	24 satellites and 3 spares
Orbits	12875 km (8 hour orbit, though the 12 hour orbit was also proposed	Geosynchronous or near geosynchronous or high altitude about 40000 km	20300 km, 12 hour orbits
Signal	sidetone range	Pseudo random sequence	Pseudo random sequence
Time settings of SV	Atomic clocks on each satellite - periodic updates from ground stations	No clocks on satellites - time transmitted from seven ground stations	Atomic clocks on each satellite - periodic updates from ground stations

Table 1.1 The basic configuration of Timation, 621B, and GPS [4]

GPS Joint Program Office (JPO) that is the responsable of the management of the contellation. GPS is a passive ranging system, that means, the users can not interact with the system, they simply receive broadcasted signals to determine their position. In this way the system can serve an unlimited number of users. The positioning method used by GPS and other modern GNSS system is the trilateration (see Section 1.1.1). GPS satisfies the requirement established in 1960 for an optimum positioning and it was declared fully operational on 27 april 1995 [5].

GPS is not the only GNSS system. In the meanwhile that U.S developed his system, Soviet Union worked at own system: GLONASS. GLONASS consists of 24 satellites on three inclined orbital planes and uses a Frequency Division Multiple Access (FDMA) technique.

Thanks to the experiences of american and russian, Europe decided to build own system, a new generation of GNSS. In 1999 the European Commission started the Galileo Project. The goal of Europe is to have own system able to provide worldwide coverage with higher accuracy to all users, advanced navigation signal. GPS and GLONASS were born as military-oriented systems, instead Galileo is the first system intended primarily for civilian use. The full precision is provided both to civil and military users. In this moment Galileo is in advanced stage of realization but not completed.

1.1.1 Trilateration in GNSS

The satellite navigation is based on the concept of trilateration. This method is based on measurements of distances to estimate the position. The user can compute his position by knowing the distances (or geometric range) between him and the position of three locations. The trilateration in the radionavigation use a physical principle that, in vacuum, the propagation of an electromagnetic wave has a constant and known speed that is the speed of light $c = 299792458$ m/s. Therefore, if the the time of flight or the Time Of Arrival (TOA) of the signal from known locations to the user can be measured, the distances can be calculated by multiplying that time with the speed of light. The main GNSS systems, like GPS or Galileo, are TOA systems. Once obtained the distances, the position, with trilateration technique, is computed by solving the system of equations

$$\begin{cases} \sqrt{(x_1-x)^2+(y_1-y)^2+(z_1-z)^2} = r_1 \\ \sqrt{(x_2-x)^2+(y_2-y)^2+(z_2-z)^2} = r_2 \\ \sqrt{(x_3-x)^2+(y_3-y)^2+(z_3-z)^2} = r_3 \end{cases} \tag{1.1}$$

The unknowns of the system in (1.1) are the coordinates of the user (x, y, z). The (x_k, y_k, z_k) with $k = 1, 2, 3$ are the coordinates of the known locations. The system represents the intersection of spheres in a 3D space with 3 equations and 3 unknowns. In case of positioning in a plane (2D case), 2 equations are needed and the problem of intersection of circles has to be solved. In case of GNSS systems, the satellites constellation is the set of locations with known positions, because it is possible to extract this information from the ephemeris.

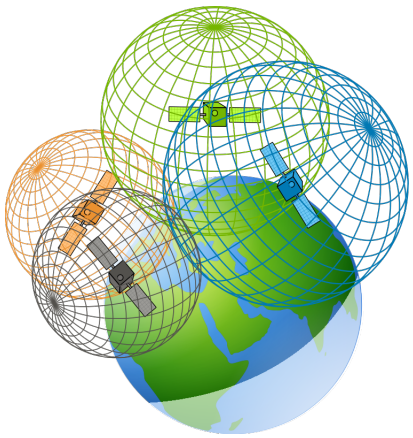

Fig. 1.1 Trilateration with four satellites [6].

Furthermore, as said, the distances are given by time measurements. This leads to hidden assumption in (1.1): the perfect synchronization between clock onboard the satellite and user clock. This situation is not real at all. To solve correctly the system it is necessary to have an additional equation to take into account the unknown referred to the clock difference (see Section 1.4).

In the real case, the signals propagate through the atmosphere (e.g ionosphere), they are affected by interference, reflections by the ground and other surfaces. All of these impairments have an impact on the estimation of the TOA, hence the distances (see Section 1.5).

1.2 System architecture

The signals transmitted by every GNSS satellite allow the users to determine his position on the earth surface. These systems are passive. Both GPS and Galileo satellite systems are based on the TOA concept, and users determine their position evaluating the time interval between the signal transmission and the signal reception.

Every single GNSS system is composed by three main segments:

- space segment (satellite constellation)
- control segment (also referred to as the ground segment)
- user segment (GNSS receivers)

1.2.1 Space segment

The space segment is composed by the satellites positioned in different orbital planes. The satellites are devoted to transmit signals, store and broadcast the navigation message keeped update by the control segment. The GNSS system is built to ensure to the user the minimum number of the satellites in view for positioning, from any point of the Earth's surface. The required number of satellites in view is at least four (see Section 1.1.1 and 1.4).

For example, in case of GPS, the nominal constellation is composed by 24 satellites, as in Fig. 1.2. The satellites are arranged in six orbital planes equally spaced and they are placed in a Medium Earth Orbit (MEO) orbit at an altitude of 20200 km and an inclination of 55° respect to the equator. The satellites have nearly circular orbits and a period of 11 hours, 58 minutes and 2 seconds [7]. The MEO orbit gives the possibility to have one satellite visible for several hours in each pass and the constellation has an adequate number of satellite to have a fully coverage of the Earth.

Galileo, in the Full Operational Capability (FOC) phase of the project, will consist of 24 satellites, in addition, 6 in-orbit spares intended to prevent any interruption in service [8]. The satellites are in MEO orbit at an altitude of 23222 km. Galileo has three orbital planes inclined at 56° with respect to the equator. The period is about 14 hours, 4 minutes and 45 seconds and guarantee at least six satellites in view from any point on the Earth. At the time of writing (end of 2016), Galileo constellation has 18 operative satellites in orbit, the last four have been launched in November 2016. The FOC is planned to be reached by 2020.

1.2.2 Control segment

The control, or ground, segment is the part responsible to keep correctly update the space segment (see Section 1.2.1). In particular the ground stations are devoted to control and maintain the configuration of the satellites. The ground stations are enabled to send messages to the satellites to correct possible drift on their orbit and keep update the navigation message for all the satellites.

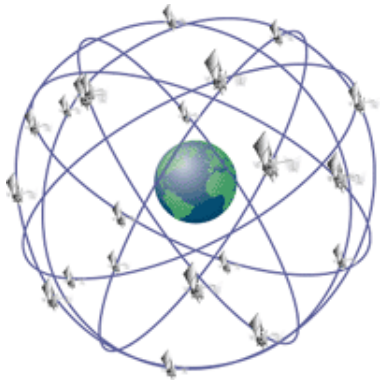

Fig. 1.2 Picture of GPS satellite constellation.

For example, in case of GPS, the control segment is a network of Monitoring Station (MS), a Master Control Station (MCS) and the Ground Antennas (GA). The MS are stations spread around the world which collect GPS data from all the satellites. The MCS is the core of the network, it collects all the data coming from the MS to estimate the ephemeris and clock errors. In Fig. 1.3 the Alternate Master Control Station (AMCS) is also shown, that is a functional backup station for the MCS. Finally, the GA uplink data to the satellites. The transmitted data include ephemerides and clock correction, so the navigation message is updated.

The positions of the ground stations around the world of the GPS control segment are shown in Fig. 1.3.

1.2.3 User segment

The user segment consists of GNSS receivers. A GNSS receiver is composed of an antenna, front-end, electronic part to elaborate the incoming signals and the data storage. The receiver has to be able to compute the PVT from the signals coming from the satellites. The receivers are used in many applications in different fields like agriculture, gaming, navigation, SoL, etc. applications. The applications discriminate the type of the receiver to be used. There are a lot of receivers available in the market from the most cheap and simple to very complex and performing.

Nowadays, several mass-market receivers are present in the smartphones with the possibility to integrate other position information from other sensors

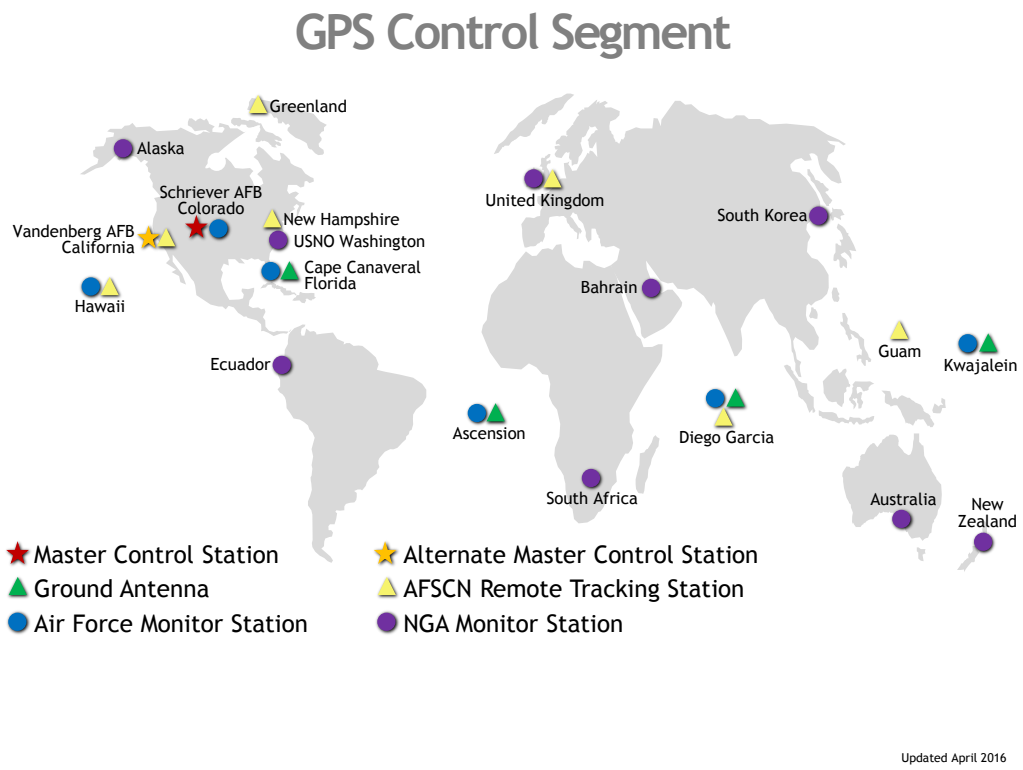

Fig. 1.3 The map of the ground stations for the GPS control segment. Figure taken from [9].

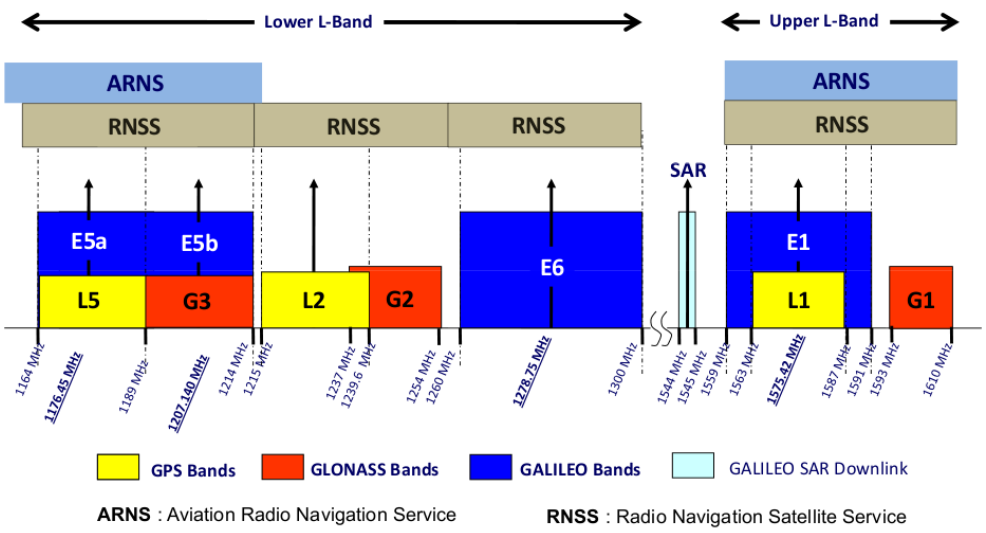

Fig. 1.4 Allocation of the frequencies for several GNSS systems [11].

and maps. The increasing number of new applications in GNSS fields leads to have a huge market and justify the recent choice of big company like Google to open the access to the pseudorange data estimated by the smartphone [10].

1.3 GNSS Signals

This section will describe the signals structure of the considered GNSS systems: GPS and Galileo.

The GNSS signals are transmitted continuously by the satellites at different frequencies in the L band that covers frequencies from 1 GHz to 2 GHz of the Ultra High Frequency (UHF) band [2]. Fig. 1.4 shows the current situation of the L band for GNSS systems. The signals contain the PRN codes, which are used to estimate the travel time from satellite to the receiver, and navigation data to get satellites coordinates.

1.3.1 GPS Signal structure

GPS satellites transmit two Binary Phase Shift Key (BPSK) modulated carriers on the L band. These frequencies are referred to as Link 1 (L1) and Link 2 (L2) and are derived from a common frequency, $f_0 = 10.23$ MHz [12]. L1 at

$f_{L1} = 154\, f_0 = 1575.42$ MHz and L2 at $f_{L2} = 120\, f_0 = 1227.6$ MHz. Each signal has a bandwidth approximately equal to 20.46 MHz. The Coarse/Acquisition (C/A) code occupies 2.046 MHz of L1 band. For civil use, the satellites transmit two other signals in addition to the C/A code on L1: L2C on L2 frequency (1227.6 MHz) and L5 on L5 frequency (1176.45 MHz). The encrypted signals transmitted by each satellite are four on both L1 and L2. In this thesis we consider only GPS L1 C/A. The signal is composed by two PRN spreading sequences modulated with a sinusoidal carrier and can be written as following:

$$y(t) = A\, C(t) d(t) \cos(2\pi f_{L1} t) + A\, C(t) p(t) \sin(2\pi f_{L1} t) \tag{1.2}$$

where:

- A is the amplitude of the signal;
- $C(t)$ is the PRN spreading code of GPS L1 C/A [13, 14]
- $d(t)$ is the bit navigation data;
- $p(t)$ is the Precise (P) code which has a rate of 10.23 MHz and only repeats once a week [13]. The P code is encrypted (P(Y)) and it is used essentially for DoD-authorized users applications;
- f_{L1} is the radiofrequency of the signal carrier at 1575.42 MHz;

The minimum received power level of the GPS signal into a 3 dB gain linear polarized antenna is specified to be -160.0 dBW for satellites with an elevation angle greater than five degrees [15]

GPS has two navigation services available:

- Standard Positioning Service (SPS), it is an open service, available for worldwide users. It is operative in single frequency in the frequency band L1.
- Precise Positioning Service (PPS), it is restricted to military and authorised users. The signals are encrypted and they are provided in two different frequency bands, L1 and L2.

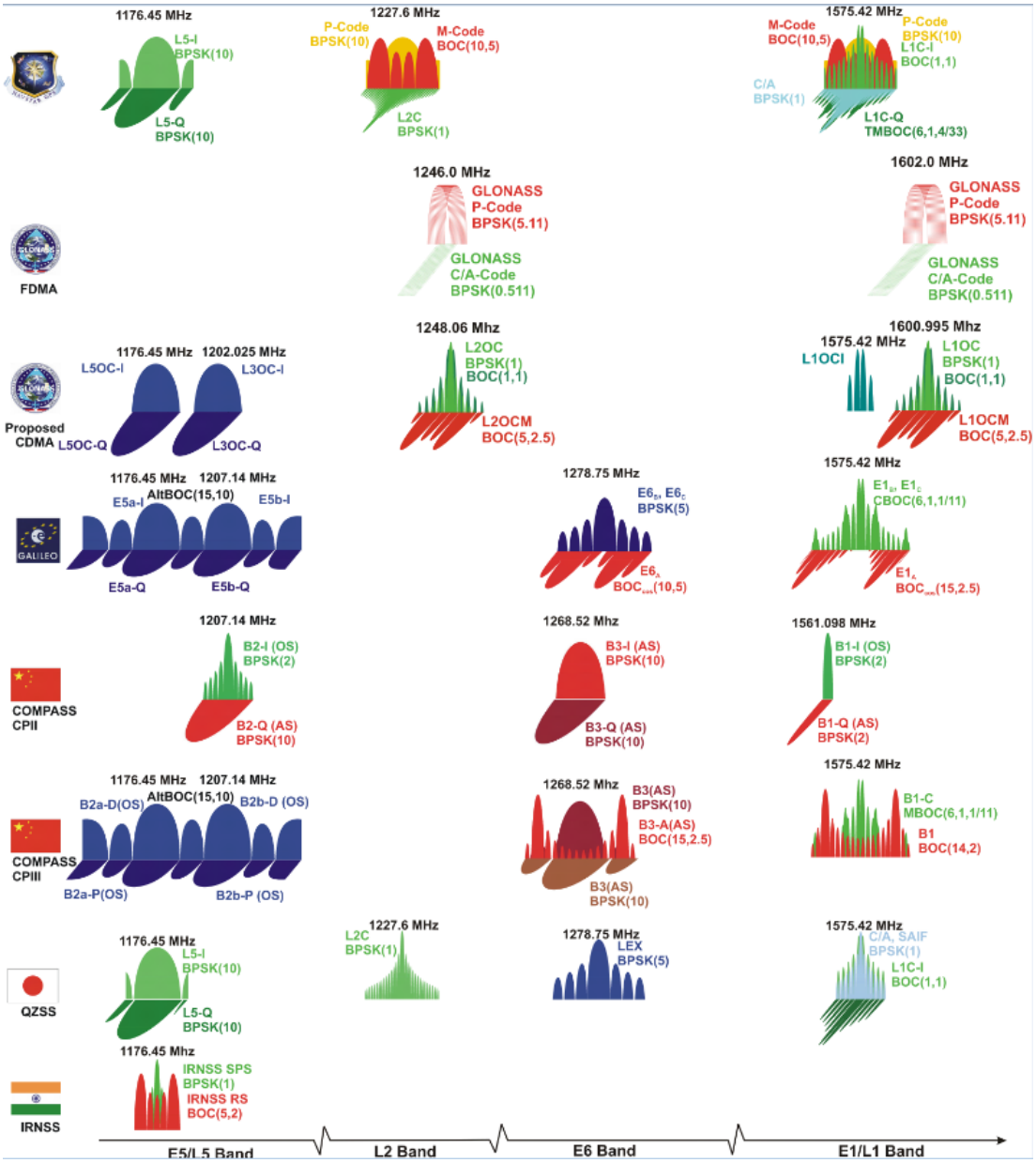

Fig. 1.5 Frequency bands used by the different GNSS systems [11].

Spreading codes for satellites navigation

The spreading sequence used in GPS L1 C/A is a Gold code, originally presented in [16]. The GPS signals are designed to look random. Each C/A code transmitted is generated using a Linear Feedback Shift Register (LFSR). The register generates a maximal length sequence of length $N = 2^n - 1$ elements. In case of GPS C/A code uses $n = 10$ so $N = 1023$. A Gold code is obtained by means of the summation of two maximum-length sequences. Every 1 ms the code is repeated, so the chip length is $1/1023 = 977.5$ ns $\approx 1\mu$s , in meters corresponds to a length of 300 m in ideal transmission conditions.

The time difference between the local code and the incoming code is computed by autocorrelation. This permits to maintain the receiver locked to the satellite code.

When the two signals are not matched in time, the ideal result of autocorrelation is zero. If the signals are matched in time, the correlation is at the maximum peak in module.

The Gold codes have the property that the autocorrelation is constant until we get to within one chip of the correct answer. In ideal case assuming no noise, within the window of ± 1 chip, the autocorrelation function looks like an equilateral triangle and, If it is normalized, its peak has value 1. For further details on the generation of the Gold codes, see [12].

1.3.2 Galileo Signal structure

The Galileo signal plan will provide five navigation service:

- Open Service (OS), similar to SPS service of GPS. It is free of charge and has up to three signal frequencies offered to the users worldwide.
- Public Regulated Service (PRS), is the service under governmental control, reserved for security authorities. The two transmitted signals are encrypted and more robust against jamming and spoofing attacks.
- Commercial Service (CS), provides two additional signals protected by commercial encryption and with higher data rates.

- Search And Rescue (SAR), Galileo supports this service for international COSPAS-SARSAT effort on humanitarian search and rescue activities
- SoL, contains integrity information. It improves the OS performance by providing timely warnings to the user when it fails to meet certain integrity requirement.

When Galileo systems will be full operative, Each satellites will transmit 10 signal in four frequency bands, namely on E1, E6, E5a and E5b, shown in Fig. 1.4. The carrier frequencies are 1575.420 MHz (E1), 1278.750 MHz (E6), 1176.450 MHz (E5a), 1207.140 MHz (E5b), 1191.795 MHz (E5=E5a+E5b), respectively [17]. The E5a and E5b signals are part of the E5 signal in its full bandwidth.

The Galileo system use a Code Division Multiple Access (CDMA) technique, as in case of GPS. The main difference from GPS is the use of Binary Offset Code (BOC) modulation and longer spreading code, so integration time. The OS of Galileo has a period of 4092 chips, that means an integration time of 4 ms. The idea of a BOC modulation is to multiply the PRN code by a digital sub-carrier obtained by take the sign of a sine or cosine waveform

$$b_{BOCs}(t) = C(t)\,\text{sign}\,[\sin(2\pi f_s t)]$$

$$b_{BOCc}(t) = C(t)\,\text{sign}\,[\cos(2\pi f_s t)]$$

where $C(t)$ is the PRN code at frequency f_c and f_s is the frequency of the sub-carrier. Typically, the BOC is defined as BOC(m,n) where $m = f_s/f_{cref}$, $n = f_c/f_{cref}$ and $f_{cref} = 1.023$ Mcps The use of a BOC modulation changes the shape of the Galileo correlation with respect to GPS. An example of Galileo correlation is shown in Fig. 3.39. For example, the BOC(1,1) has a narrower peak than the BPSK and has two side lobes. The signals can contain data and pilot channels. The pilot channels are data free signals and their purpose is to help the tracking of weak signals for data channels.

- E1 signal. E1 is a signal transmitted in the L1 band. E1b is the data signal and E1c is the data-free signal and it is also called a pilot signal. On the pilot signal a secondary code of length 25 chips extends the repetition interval to 100 ms. E1b contains unencrypted ranging codes

and navigation data accessible to all users. On E1 is used a Composite BOC CBOC(6,1,1/11) modulation. The E1 frequency band also contains a PRS signal (E1a).

- E6 signal. E6 is used for CS and it contains a data channel E6b and a pilot channel E6c. The ranging codes and data are encrypted. the E6 frequency band also contains a PRS signal component (E6a).
- E5a signal. E5a is a signal transmitted in the E5 band. E5a contains a data channel and a pilot channel. It has unencrypted ranging codes and navigation data which are accessible by all users.
- E5b signal. E5b is a signal transmitted in the E5 band. E5b contains a data channel and a pilot channel.It has unencrypted ranging codes and navigation data accessible to all users.
- E5 (composite) signal. The E5a and E5b signals are modulated onto a single E5 carrier using a technique known as Alternative BOC (AltBOC). The AltBOC is a modified version of a BOC with code rate of 10.23 MHz and a sub-carrier frequency of 15.345 MHz. AltBOC(15,10) is a wideband signal that is transmitted at 1191.795 MHz [17]. The composite of the E5a and E5b signals is denoted as E5 signal.

Galileo E1 OS

The signal model of Galileo E1 is described as a sum of E1a and E1b each one modulated with a CBOC scheme. The Galileo E1 OS is generated with 2 ranging codes and one data signal, the signal model can be written as following:

$$x_{E1}(t) = \frac{1}{\sqrt{2}} e_{E1B}(t) \left(\sqrt{10/11} b_{BOCs,f_b}(t) \right) + \left(\sqrt{1/11} b_{BOCs,f_c}(t) \right) - \frac{1}{\sqrt{2}} e_{E1C}(t) \left(\sqrt{10/11} b_{BOCs,f_b}(t) \right) - \left(\sqrt{1/11} b_{BOCs,f_c}(t) \right)$$

with $f_c = 1.023$ MHz and $f_b = 6.138$ MHz, and with

$$e_{E1B}(t) = c_{E1B}(t)\, d_{E1}(t),$$
$$e_{E1C}(t) = c_{E1C}(t).$$

where c_{E1B} and c_{E1C} are the ranging codes and d_{E1} is the data signal.

1.4 Position, velocity and time

In Sec. 1.1.1, we introduced the concept of trilateration used in the main GNSS systems. Previous Eq. (1.1) is modified to take into account several factors to get the user position $\mathbf{u} = (x_u, y_u, z_u)$ in Earth-Centered Earth Fixed (ECEF) coordinates.

First of all, we define the coordinates of the generic satellite $\mathbf{s} = (x_k, y_k, z_k)$. The geometric range, in vectorial notation, between the k-th satellite and the user is $r_k = \|\mathbf{s_k} - \mathbf{u}\|$.

As already discussed, the GNSS systems are based on TOA concept. Hence, the distance is computed by measuring the propagation time between satellite and user of the transmitted ranging code.

The user coordinates are unknown, while the satellites coordinates are contained in the navigation message. The geometric range r_k is the measurement in case of perfect synchronization between clocks. In Eq. (1.3) is shown the basic system of four equations (called navigation equations) that allows to get a solution for the user position, taking into account the receiver clock bias δb.

$$\begin{cases} \sqrt{(x_1 - x_u)^2 + (y_1 - y_u)^2 + (z_1 - z_u)^2} + c\,\Delta b = \rho_1 \\ \sqrt{(x_2 - x_u)^2 + (y_2 - y_u)^2 + (z_2 - z_u)^2} + c\,\Delta b = \rho_2 \\ \sqrt{(x_3 - x_u)^2 + (y_3 - y_u)^2 + (z_3 - z_u)^2} + c\,\Delta b = \rho_3 \\ \sqrt{(x_4 - x_u)^2 + (y_4 - y_u)^2 + (z_4 - z_u)^2} + c\,\Delta b = \rho_4 \end{cases} \tag{1.3}$$

This non linear system can be solved analytically [18] or, the solution can involve iterative methods like Least Mean Squares (LMS) or more complex like KF. Before to solve the system, it is applied a linearization of the equations. The idea of the linearization is, if we know approximately the user position $\hat{\mathbf{u}} = (\hat{x_u}, \hat{y_u}, \hat{z_u})$, we can get the offset $\Delta\mathbf{u} = (\Delta x_u, \Delta y_u, \Delta z_u)$ from the true position (x_u, y_u, z_u). Every single pseudorange is approximated as a Taylor expansion around the approximate position. It is possible to obtain $(\Delta x_u, \Delta y_u, \Delta z_u)$ as linear function of known coordinates, bias and pseudoranges measurements. Therefore, using

the approximate position

$$\sqrt{(x_k - \hat{x_u})^2 + (y_k - \hat{y_u})^2 + (z_k - \hat{z_u})^2} + c\,\Delta\hat{b} \simeq \rho_k$$

the system in (1.3) becomes

$$\begin{cases} a_{x_1}\Delta x_u + a_{y_1}\Delta y_u + a_{z_1}\Delta z_u - c\,\Delta b = \Delta\rho_1 \\ a_{x_2}\Delta x_u + a_{y_2}\Delta y_u + a_{z_2}\Delta z_u - c\,\Delta b = \Delta\rho_2 \\ a_{x_3}\Delta x_u + a_{y_3}\Delta y_u + a_{z_3}\Delta z_u - c\,\Delta b = \Delta\rho_3 \\ a_{x_4}\Delta x_u + a_{y_4}\Delta y_u + a_{z_4}\Delta z_u - c\,\Delta b = \Delta\rho_4 \end{cases}$$

where $\Delta\rho_k = \rho_k - \hat{\rho}_k$. The vector $\mathbf{a_k}$ is the Line Of Sight (LOS) direction of the unit vector pointing from the approximate user position to the k-th satellite:

$$\mathbf{a_k} = \frac{\mathbf{s_k} - \hat{\mathbf{u}}}{\|\mathbf{s_k} - \hat{\mathbf{u}}\|}$$

Then by collecting all the equation and quantity in the matrix notation, we have

$$\mathbf{\Delta}\rho = \begin{bmatrix} \Delta\rho_1 \\ \Delta\rho_2 \\ \Delta\rho_3 \\ \Delta\rho_4 \end{bmatrix}$$

then, the so-called geometry matrix

$$\mathbf{H} = \begin{bmatrix} a_{x_1} & a_{y_1} & a_{z_1} & 1 \\ a_{x_2} & a_{y_2} & a_{z_2} & 1 \\ a_{x_3} & a_{y_3} & a_{z_3} & 1 \\ a_{x_4} & a_{y_4} & a_{z_4} & 1 \end{bmatrix} \tag{1.4}$$

and the vector of the increment

$$\Delta\mathbf{x} = \begin{bmatrix} \Delta x_u \\ \Delta y_u \\ \Delta z_u \\ -\Delta b \end{bmatrix}$$

Furthermore, the system can be rewritten as

$$\mathbf{\Delta}\rho = \mathbf{H}\Delta\mathbf{x}$$

In case of four satellites, the simplest solution is an inversion matrix problem

$$\Delta\mathbf{x} = \mathbf{H}^{-1}\mathbf{\Delta}\rho$$

Generally we have more than four satellites in view so, in this case, to solve the system, we could use LMS. LMS is used to solve overdetermined systems with more equations than unknown and the solution is given by

$$\Delta\mathbf{x} = (\mathbf{H}^T\mathbf{H})^{-1}\mathbf{H}^T\mathbf{\Delta}\rho \tag{1.5}$$

1.4.1 Carrier-Phase Measurement

Carrier phase measurements is another way to compute the pseudorange without exploiting the code phase measurements. The carrier phase measurements consist on the estimation of the difference between the phase of the receiver local carrier and the carrier received from a satellite at the instant of the measurement. It is an indirect and ambiguous measurement of the signal transit time [2]. The measurement is expressed in units of cycles. This measurement has higher precision than code phase, but the whole number of cycles between satellite and receiver is unknown and it needs to be estimated, this is called Integer ambiguity.

The counting mechanism is based on the Doppler frequency shift, this because the variation in carrier phase, between two consecutive time instants, can be derived by integrating over the interval of the epoch.

For each epoch, the phase of the carrier is accumulated following the model in (1.6) [3].

$$\phi_n = \phi_{n-1} + \int_{t_{n-1}}^{t_n} f_D(\tau)\, d\tau + \phi_f \tag{1.6}$$

where n is the discrete time epoch, ϕ_n is the accumulated phase at epoch n, f_D is the Doppler frequency of the carrier, ϕ_f is the fractional part of the accumulated phase given by the carrier-phase tracking loop of the receiver.

It is possible to have very high precision on the navigation solution because the resolution depends on the wavelength λ of the carrier. In case of GPS L1 C/A $\lambda \approx 19$ cm.

Without taking into account the code, the main problems of the carrier phase solution are given by the Integer ambiguity, that makes ambiguous the measurements (maybe precise but presence of bias in the solution) and the cycle slips (presence of jumps in the solution).

In the thesis, in particular in Chapter 6, we are not interested in carrier phase measurements but to another concept: carrier smoothing.

Carrier-smoothing solution

The solution given by the pseudorange computed with the code measurements are noisy but unambiguous thanks to the characteristics of the code. Thanks to the carrier measurements, which are precise but ambiguous, it is possible to smooth the code measurements. The algorithm proposed in literature is the Hatch filter expressed as follows [7, 2]:

$$\hat{\rho}_i(k) = \frac{1}{n}\,\rho_i(k) + \frac{n-1}{n}\,[\rho_i(\hat{k-1}) + (\phi_i(k) - \phi_i(k-1))] \tag{1.7}$$

where the index i is referred to the SV and k is the generic discrete time instant. The $\rho_i(k)$ and $\phi_i(k)$ are the code-based pseudorange and the carrier measurements in meters. Then, $\hat{\rho}_i(k)$ is the smoothed pseudorange in output of the filter.

The filter, at the beginning, has a transient and it has to be initialized, so $\hat{\rho}_i(1) = \rho_i(1)$ where $n = k$ when $k < n$ and $n = N$ when $k \geq N$. N is the length of the filter.

The algorithm suffers the problem of the cycle slips. Cycle slips are errors in the cycle counting given by the problems on the incoming signal like scintillation, MP etc. Therefore, the Hatch filter in (1.7) needs to be reset at the initial state every time a cycle slip occurs.

Segment Source	Error Source	1 σ Error (m)
Space/control	Broadcast clock	1.1
	L1 P(Y)-L1 C/A group delay	0.3
	Broadcast ephemeris	0.8
User	Ionospheric delay	7.0
	Tropospheric delay	0.2
	Receiver noise and resolution	0.1
	Multipath	0.2
System UERE	Total (RSS)	7.1

Table 1.2 Typical values for UERE budget [3].

1.5 Error budget

By using the measurement of the time of flight of a signal, the position and consequently the speed can be estimated. After the presentation of the system and how to estimate the receiver position, it's essential to have an idea of the several error sources which affect the accuracy of the position estimation. In Tab. 1.2 are collected the main error sources on the different segment of the GPS for SPS. It's remarkable to remind that the errors on the position depend on both pseudorange error (UERE) and the geometry factor, Dilution of Precision (DOP) between user and satellites.

1.5.1 Multipath

The MP is an interference generated by reflecting surface around the receiver. It is a replica of the original signal, typically delayed and attenuated. It is one of the main source of error difficult to handle and with different behaviour in different environments. The errors are different in frequency, for instance, the same surface can reflect differently L1 and L2 carrier. The satellites with low elevation are the ones most affected by the MP. It affects both code and carrier measurements. The interference given by the MP, can be attenuated using directional antennas, which could have particular radiation pattern that can reduce the gain from specific direction, e.g. from the ground (as in Fig. 1.12). Another way is to use long integration time or different architectures in the GNSS receivers to mitigate the impact of the MP [19, 20]. Due to the geometric nature of the MP, the error can be visible in the position domain. In

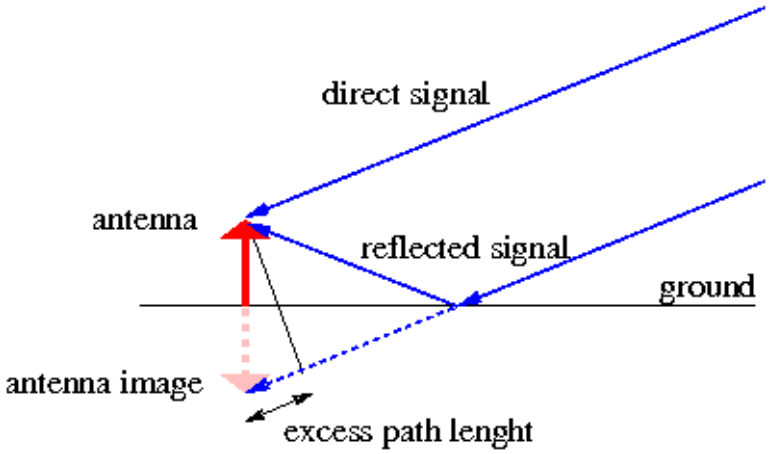

Fig. 1.6 Example of ground MP reflection [21].

particular, by collecting data with a static receiver for consecutive days and by observing the results. The same kind of errors are repeated anytime appears the same satellite-user geometry. The MP is one of the main impairments treated in this thesis.

1.5.2 Interference

The satellites of a GNSS constellation transmit the data by means of Radio-Frequency (RF) signals. As all wireless communication systems, they are vulnerable to the interference present in the environment where the signals are transmitted. These interferers might degrade the navigation solution or the receiver might lose the lock of the incoming signals [3]. Based on the comparison between bandwidth of the interferer and the GNSS signal, the interference can be either wideband or narrowband. The interference is classified as unintentional or intentional. The latter category can further be classified as jamming and spoofing. The jamming consists to the transmission of high power signal in the GNSS signal bandwidth to blind the user receiver and do not permit it to perform its operations. Instead, the goal of a spoofing is to mislead the receiver through the use of false GNSS signals in order to compute wrong position.

In this thesis, the spoofing problem is treated in Chapter 5. This topic was done in collaboration with another PhD student.

1.6 Receiver Architecture

Before introducing the receiver used in our experiments, it is necessary to give the notations and the model of the GNSS signal and channel. As previously mentioned, GNSS signal is transmitted by using CDMA format and, the received signal is under the power level of the noise. After downconversion and Analog to Digital Converter (ADC), a typical GPS L1 C/A sampled signal can be written as a combination of the Signal In Space (SIS)s of all the satellites in view, each one expressed by

$$y_m(nT_s) = \sqrt{2P_m}C_m(nT_s - \tau_m)d_m(nT_s - \tau_m)\cos(2\pi(f_{IF} + f_{d,m})nTs + \varphi_m) + n_0(nTs) \tag{1.8}$$

where:

- m is the index of a specific satellite;
- P_m is the received power;
- $C_m(\cdot)$ is the PRN spreading code;
- $d_m(\cdot)$ is the navigation data;
- f_{IF} is the intermediate frequency of the front-end;
- f_d is Doppler frequency;
- φ_m is a phase term;
- τ_m is the code delay;
- T_s is the sampling interval.
- The second term of the sum is a noise component $n_0(nTs)$, that is a discrete-time random process obtained by sampling the noise at the front-end output. Since the input noise may be assumed to be White Gaussian Noise (WGN) with power spectral density $S(f) = N_0/2$, at the front-end output $n_0(nTs)$ becomes a Gaussian discrete-time random process with zero mean and variance $\sigma^2 = N_0 B_{IF}$, where B_{IF} is the front-end bandwidth.

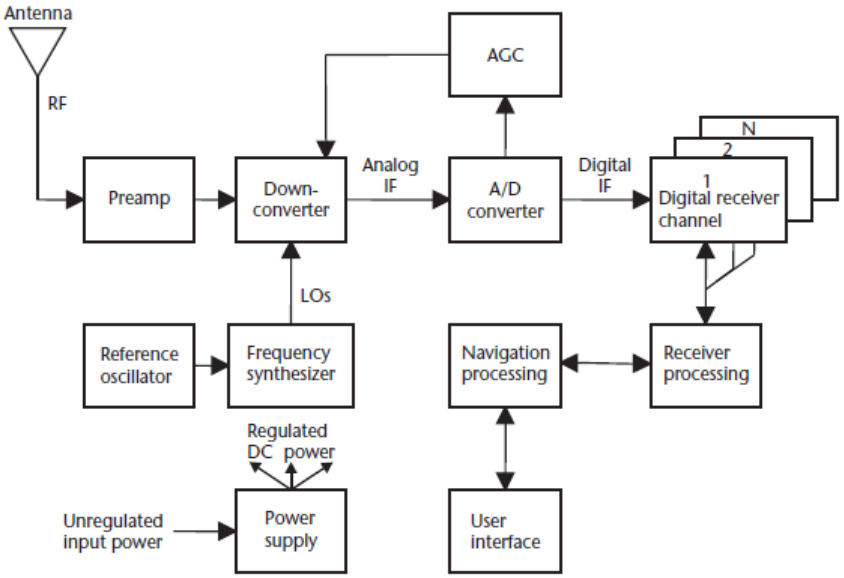

Fig. 1.7 General architecture of a GPS receiver taken from [3]

Therefore (1.8) represents a so called Additive White Gaussian Noise (AWGN) channel. Thanks to the code orthogonality, the receiver can discriminate different signals coming from different satellites. Therefore the analysis of the receiver can be done only considering the signal $y_m(nT_s)$.

To evaluate the amount of noise with respect to the signal, a fundamental parameter is the *carrier-to-noise* ratio, defined as $C/N_0 = P_m/N_0$. This ia an important metric. In general, higher C/N_0 we have, less noisy range measurements we get to have a better positioning.

The architecture of the software receiver used for the simulations is shown in Fig. 1.7. We are interested in the tracking stage, which gives results in the correlation domain of a single GNSS channel. Since tracking requires a preliminary acquisition stage, in the following also the acquisition system is described. The other parts before and after these stages (i.e downconversion, PVT computation) are not considered in this report. For example, the working frequencies of the front-end used in 3 are $f_{IF} = 4.130400$ MHz and $f_{sampling} = 16.367600$ MHz. The ratio between the sampling frequency f_s and the chip rate R_c is not an integer value, in order to takes advantage from the incommensurability of the code.

1.6.1 Acquisition stage

The aim of this stage is to conduct a rough search on a 2D space in order to give a coarse estimation of the code delay and Doppler frequency of the signal to verify the presence of the signal. The acquisition algorithms try to look for the maximum of the Cross Ambiguity Function (CAF), that theoretically is the point with the correct values of τ and f_d of the incoming signal (see the example in Fig. 1.8, which shows a normalized search space). The CAF is given by

$$S(\tau, F_D) = \frac{1}{N} \sum_{n=0}^{N-1} r(nT_s) C(nT_s - \tau) e^{-j2\pi F_D n} \tag{1.9}$$

where $r(nT_s)$ are the samples of the received signal, τ is a variable code delay and F_D is a variable Doppler frequency. The variable code delay is obtained by using a circular-shifted version of the local code $C(nT_s)$, thus (1.9) assumes the form of a Discrete-Time Fourier Transform (DTFT), which can be evaluated by using a Fast Fourier Transform (FFT) algorithm. The peak of the CAF can be identified once the samples of $S(\tau, F_D)$ are available. In our implementation, there are two steps for the acquisition: one uses a Doppler step larger than the second one, in order to have a fastest acquisition stage and to give a coarse estimation but with sufficient precision for the tracking stage. The second step starts only if the first one misses to acquire the signal.

1.6.2 Tracking stage

The goal of this stage is to maintain the incoming signal aligned with a local replica of the code and the carrier.

Code tracking

A classical method to align the incoming and the local code is to use a code tracking loop. In a GPS receiver the tracking loop is generally a DLL. To characterize the DLL, we need to design the integrators, the code loop discriminator, and the code loop filter. A generic block diagram of a code tracking is shown in Fig. 1.9. After the demodulation of the signal (1.8), obtained by multiplying it by two local carrier waves at frequency f_{IF}, one for each branch

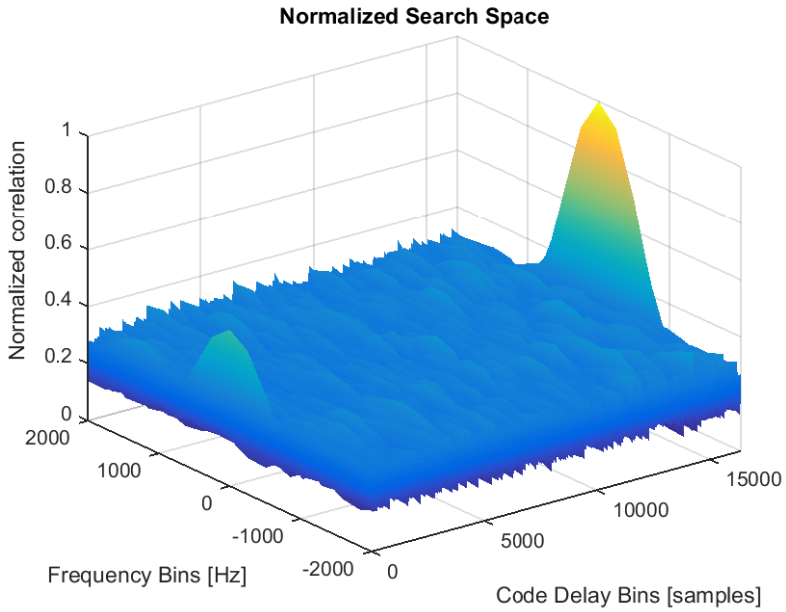

Fig. 1.8 example of Normalized search space at $C/N_0 = 45dBHz$

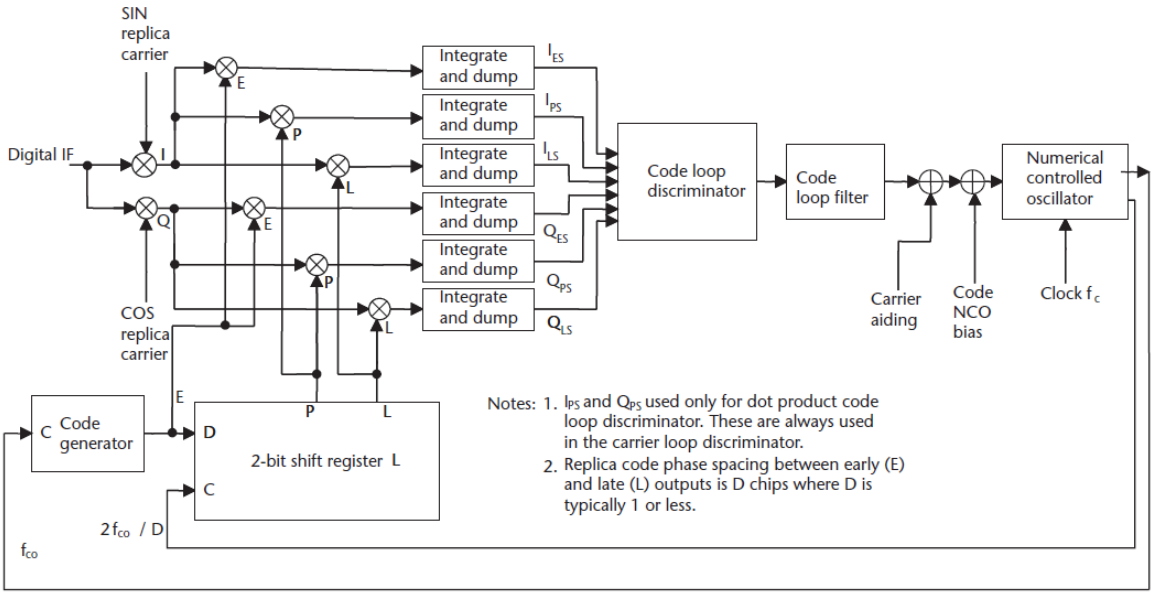

Fig. 1.9 model of GPS code tracking loop [3]

of the receiver (I and Q), the resulting signal is multiplied by three local codes (called early, prompt, late) shifted by $-1/2$, 0 and $+1/2$ chip time and the outputs are integrated and dumped to implement the correlator. The common DLL discriminators are divided in two classes:

- *coherent* ($(I_e - I_l)$), which requires a good estimation of the frequency and phase of the Intermediate Frequency (IF) carrier, because if the local carrier is in phase with the input signal, all the energy will be in the in-phase branch.
- *non-coherent*, which has to be used when there is a misalignment of the local carrier with the input carrier. In fact in this case the energy will be divided in two branches, and then the DLL must use both in-phase and in-quadrature branches.

In our experiments we use the following non-coherent DLL discriminator:

$$\frac{(I_e^2 + Q_e^2) - (I_l^2 + Q_l^2)}{(I_e^2 + Q_e^2) + (I_l^2 + Q_l^2)}$$

called *Normalised Early minus Late power*. The code loop filter, at the output of the discriminator, reduces the effects of the noise and has bandwidth $B_l = 2$ Hz, $\zeta = 0.707$, gain of the overall loop $K_0 K_d = K = 1$ and natural frequency $\omega_n = \frac{B_l}{0.53}$. Loop filter coefficients are $t_1 = \frac{K}{(\omega_n \cdot \omega_n)}$ and $t_2 = 2 \cdot \frac{\zeta}{\omega_n}$.

Costas loop

The aim of the Phase Lock Loop (PLL) is to keep locked the incoming signal, by means of a continue estimation, epoch by epoch, of the phase of the incoming carrier. An example is shown in the block diagram of Fig. 1.10 known as Costas loop, and based on two multiplications by local signals shifted each other by 90°, in the same way as in the DLL's branches. In other words, a Costas loop tries to maintain all the energy in the in-phase branch [2], as seen in Fig. 1.11. Typically, a PLL is sensitive to 180° phase shifts due to data bit transitions, for this reason it is important to have a PLL insensitive to this jump of phase. After the multiplication block, that generates frequency components at $2f_{IF}$ that are eliminated with a low pass filter, the output comes

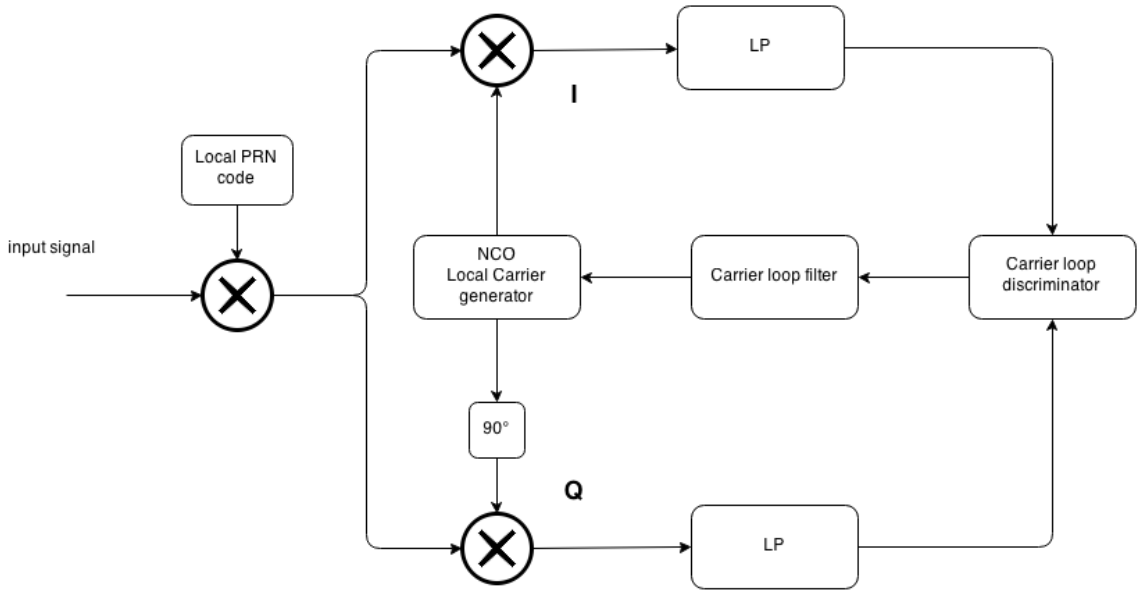

Fig. 1.10 Scheme of Costas Loop

into the PLL discriminator that returns a phase error

$$\phi_e = \tan^{-1}\left(\frac{Q}{I}\right)$$

Costas loop is insensitive because the discriminator provides $\phi_e = 0°$ in the cases the real error is 0 or $\pm 180°$.

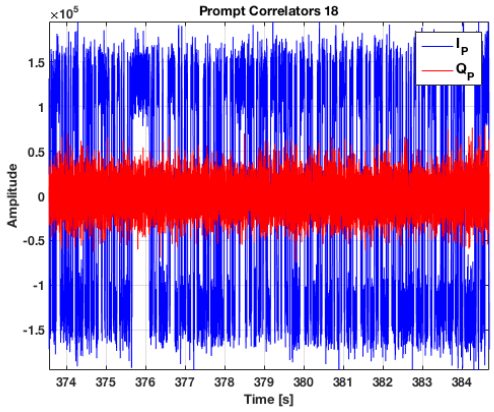

Fig. 1.11 Example of I and Q prompt correlators when the incoming signal is locked

Carrier and code tracking loop

DLL and PLL block diagrams are generally not separated, but the output of each loop is an input of the other one in order to keep the tracking of the incoming signal. The prompt correlator of the DLL helps to calculate ϕ_e and this last one helps to correct the phases of the local carrier for demodulation purpose. We chose an integration time equal to the C/A code periodicity, so at each iteration of the loop the tracking stage takes 1 ms of the signal in terms of number of raw samples, demodulates by multiplying the input signal by local carrier replicas at frequency f_{IF} and the results are used to compute 6 correlation points (I/Q and early, prompt and late).

Another important point is how to generate the local code and how to reach a resolution higher than T_s in the correlation domain to improve the estimate of the delay of the input signal. Thanks to the incommensurability of the code (the ratio between sampling frequency and the chip rate is not an integer value), the number of samples per each single chip is not constant, but could be N or $N+1$. For instance, in the simulation we used a sampling frequency of about ≈ 16 MHz, from which the number of samples per chip results in the *average*

$$\frac{T_{chip}}{T_s} = \frac{f_s}{f_{chip}} = 15.9996$$

where T_{chip} is the chip duration, and $f_{chip} = 1.023$ MHz. The PRN code is re-sampled every 1 ms by using the normalized sampling interval

$$\frac{T_s}{T_{chip}} = \frac{f_{chip}}{f_s}$$

and the correction term Δ_{f_c}, generated at the output of the DLL code loop filter, is used to update f_{chip} in the form

$$f_{chip}[n+1] = f_{chip}[n] + \Delta_{f_c}$$

The correlation points evaluated by the DLL can be written in the form $2N_{points}+1$, where N_{points} is the number of correlation points evaluated at the right or left side of the correlation peak. Another important parameter of a DLL is the *maximum spacing* d_{sp}, which is a quantity normalized with respect

to T_{chip}, from which the DLL resolution can be written as

$$R_{res} = \frac{d_{sp} T_{chip}}{N_{points}} \tag{1.10}$$

In a standard DLL, $N_{points} = 1$, so the total number of correlator points is $2N_{points} + 1 = 3$.

1.7 Narrow correlation

The GPS receivers usually use $d = 1.0$ chip early-late correlator spacing for the DLL in the tracking loop [22]. To reduce the multipath effects, the first approach to use is the narrow correlation technique. This technique has been developed for GPS receivers by NovAtel Inc. Instead of using a spacing $d = 1.0$ chip, in narrow correlation technique is typically used a value less than $d = 1.0$. The narrow correlator spacing also reduces the influence of the noise in a DLL. This because the impact of the noise is proportional to the chip spacing.

It has been noted that multipath effects in a DLL tend to dominate the error budget using the GPS L1 C/A. The multipath error envelope is illustrated in Fig. 1.12 where different value of chip spacing and a multipath relative amplitude is $\alpha = 0.5$. Compared to the spacing $d = 1.0$, the DLL performance can be enhanced significantly by using the narrow correlation technique. In Fig. 1.12 shows that the impact of the multipath decreases for values $d = 0.5$, $d = 0.3$ $d = 0.1$. This is because, due to multipath distortion, the correlation function near its peak is less severe than that at regions away from the peak [22].

1.8 Multipath Estimating Delay Lock Loop

This section provides an overview on one of the most important technique to mitigate the multipath implemented by NovAtel in the mid 1990s. This technique is called Multipath Estimating Delay Lock Loop (MEDLL) [23, 24]. The MEDLL applies Maximum Likelihood Estimation (MLE) in order to reduce both code and carrier multipath errors by using a receiver structure which

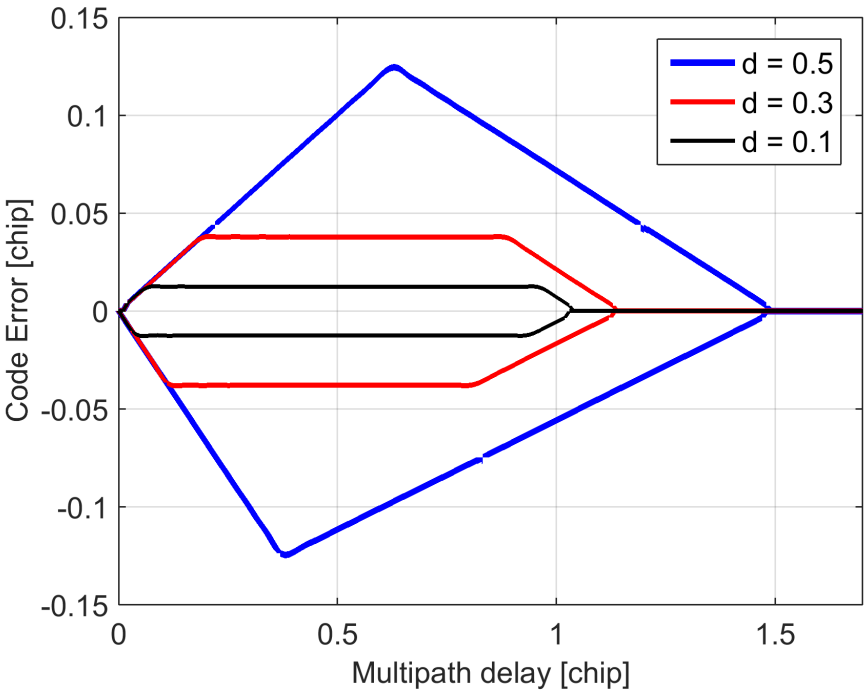

Fig. 1.12 Multipath Error Envelope with MSR = -6 dB. BPSK(1)and spacing $d = 0.5$, $d = 0.3$ $d = 0.1$

simultaneously estimates the parameters of LOS and multipath signals. The signal model considered for the received signal is

$$r(t) = \sum_{i=0}^{M} \alpha_i p(t-\tau_i)\cos(\omega t + \phi_i) + n(t) \tag{1.11}$$

where $r(t)$ is the sum of $M+1$ signals, $p(t)$ is the spreading code and the navigation data, $n(t)$ is the noise term and α_i, τ_i, ϕ_i are the amplitude, the time delay and phase of the i-th signal respectively. To get the LOS component, the index i is set to zero.

In a normal tracking loops, by using DLL and PLL, it is possible to have an estimation of τ_0 and ϕ_0 only. The approach followed by the MEDLL is to estimate the multipath parameters. The estimated signal $s(t)$ can be written as

$$s(t) = \sum_{i=0}^{M} \hat{\alpha}_i p(t-\hat{\tau}_i)\cos(\omega t + \hat{\phi}_i) \tag{1.12}$$

The correct estimation of the multipath parameters have to minimize the Mean Square Error (MSE):

$$L(\hat{\alpha}_i, \hat{\tau}_i, \hat{\phi}_i) = \int_{t-T}^{t} [r(t) - s(t)]^2 dt$$

The Eq. (1.12) can be solved by setting the partial derivatives $\partial L/\partial\hat{\alpha}_i$, $\partial L/\partial\hat{\tau}_i$, $\partial L/\partial\hat{\phi}_i$ to zero.

The MEDLL method finds a set of $M+1$ correlation functions (LOS and multipath components) which, if summed, they provide the best fit of the current measured correlation under the MSE criteria. The MEDLL decomposes in a sum of correlation functions the current correlation, then all the multipath components are subtracted from the current correlation and, the remaining correlation is then used to get a better estimation of the code tracking error.

To limit the computational load, NovAtel's first MEDLL receivers worked with 12 correlators per channel and assumed the existence of three signal components, one direct path plus two multipath components. [25].

Other mitigation techniques are presented in literature suitable to decompose the incoming signal into a set of LOS and multipath components like Multipath

Mitigation Technology (MMT) which assumes a model with the direct signal plus one single multipath component [26].

In Chapter 3 a novel method to estimate multipath components will be presented and some considerations about the difference will done.

1.9 Software receiver

For the purpose of this thesis, it was necessary to work with the data coming from the tracking loops which typically are internal data, not visible outside the receiver. To do that, a Software-Defined Radio (SDR) solution was chosen and most of the results come from a receivers using this approach. The SDR is a radio system where components have been implemented by using software on a computer or embedded system instead of to be hardware components. The main advantage of this approach is the possibility to easily reconfigure the architecture of the system. SDR is the approach that permits to handle all the receiver stages in order to check specific parameters or modify part of the receiver without any additional costs. This is important to design and test prototypes both in the context of a company or for academic research. The evolution of the communication systems and, more specific, the GNSS receivers is to reduce the number of the parts that now have to be realized in analogical. In particular the antenna and the front-end need to be analogical, then by means of an analogical to digital converter the signal pass from analogic to digital domain. The optimization of the software code in order to have an efficient and complex GNSS receiver is an actual research topic [27, 12, 28, 29].

Chapter 2

Integrity

To assess the quality of the positioning information it is necessary to define four parameters:

- accuracy: the accuracy of an estimated value (position, velocity, time, angles etc.) at a given time is defined as the degree of conformance between the estimated value and the true parameter. Accuracy is usually presented as a statistical measure of the performance of the system.
- continuity: is the capability of the whole system to work without any interruption during the period of an operation. More precisely, given a specified level of accuracy and integrity performance, continuity is the probability that the system is able to maintain this performance for the duration of the operation.
- availability: is the percentage of time that the system is able to provide services to the user.
- integrity: Integrity relates to the reliability of a measurement. It will be discussed deeply in this chapter.

These parameters are referred to as Required Navigation Performance (RNP) parameters[30, 31].

Integrity relates to the trust of the navigation information, the ability of a navigation system to provide timely warnings to users when navigation

information is unreliable so the system should not be used. To define this concept, the positioning systems, with integrity constraints, calculate the Protection Level (PL). PL, as introduced in Section 2.1.2, is a zone around the receiver with certain statistical characteristics, that guarantees a safety positioning of the receiver. To ensure the integrity, PL must to be ranged by a limit that guarantees the error between computed position and the true one is bounded. Integrity is a topic that in the last years increased its importance not only in the aviation but also in maritime and railways applications, and in general for SoL services and liability critical applications.

SoL systems generally adopt RAIM algorithms devoted to PL computation. RAIM systems also include methods able to identify satellites, whose signals present anomalies, in order to discard them from the navigation solution.

These RAIM systems are algorithms which work with data of the range or position domain, typical output of a GNSS receiver. However, the information about the anomalies is also detectable by analyzing the correlation of the single satellites. Therefore, fault detection by using signal processing techniques can be derived and it is one of the purpose of this thesis.

2.1 Trustworthy measurements

To discuss about integrity, we start by recalling some statistical concepts. In this section the concept of confidence level is recalled from the statistical point of view. Then, the main concepts related to the integrity are introduced. This helps to have a understanding of the terms used in the thesis.

2.1.1 Confidence interval

Let's start by defining the quantities:

$$x = x_t + \epsilon \tag{2.1}$$

where x_t is the true value of the parameter which needs to be estimated, x is a random variable which represents the estimate of x_t and ϵ is the error associated to the estimate and modeled as a random variable. From (2.1) it is

possible to state the probability of the event A that x exceeds a given threshold γ, so

$$P(A) = Prob(|\epsilon| > \gamma)$$

To establish this probability, a Probability Density Function (PDF) $f_\epsilon(e)$ of the error ϵ has to be known. Therefore the probability $P(A)$ can be expressed as

$$P(A) = \int_{-\inf}^{-\gamma} f_\epsilon(e)de + \int_{\gamma}^{\inf} f_\epsilon(e)de = 1 - \int_{-\gamma}^{\gamma} f_\epsilon(e)de \tag{2.2}$$

If $f_\epsilon(e)$ is a zero-mean Gaussian PDF with σ_ϵ^2, the $P(A)$ in equation (2.2) can be computed as

$$P(A) = \text{erfc}\left[\frac{\gamma}{\sqrt{2\,\sigma_\epsilon^2}}\right]$$

and can be solved for the threshold γ

$$\gamma = \sqrt{2\,\sigma_\epsilon^2}\,\text{erfc}^{-1}(P(A)) = k\,\sigma_\epsilon \tag{2.3}$$

where $k = \sqrt{2}\,\text{erfc}^{-1}(P(A))$. Therefore $P(A)$ is the probability of the absolute value of the error ϵ which exceeds the threshold γ, so ϵ is bounded to within the confidence interval $\pm\gamma$ with probability $1 - P(A)$.

2.1.2 Integrity risk and Protection Level

When we talk in terms of integrity, the probability $P(A)$ that $|\epsilon|$ exceeds $\gamma = k\,\sigma_\epsilon$ is called Integrity Risk (IR) or loss of integrity. The concept of the confidence interval $x - \gamma < x_t < x + \gamma$ in the language of integrity is called PL. PL is the radius of circumference in a plane or, of a sphere in a tridimensional space which has the center in the true position.

The concept of PL can be divided in Horizontal Protection Level (HPL) and Vertical Protection Level (VPL). The former is defined as the bound of the Horizontal Position Error (HPE) and the latter is defined as the bound of the Vertical Position Error (VPE). Depending on the case, these two definitions are used in different applications. In aviation domain, the vertical dimension is more critical than the horizontal one. Instead, for land applications, the situation is the opposite.

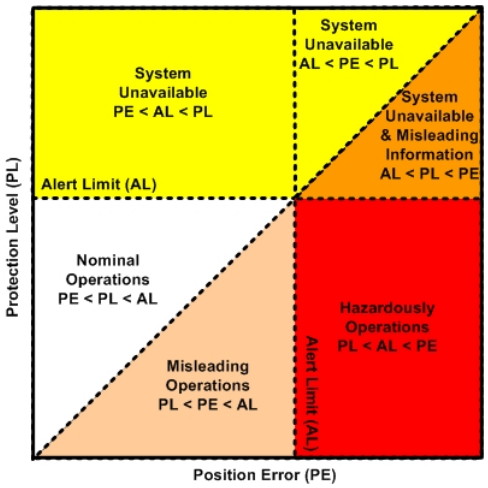

Fig. 2.1 Example of Stanford diagram [32]

Another important integrity parameter, similar to the PL, is the Alarm Limit (AL). The AL is the radius of an interval, with its centre being at the true position, which describes the region which is required to contain the indicated position with a probability $1 - P(A)$.

When an integrity event occurs, the systems has to provide timely warnings after the event. This time, called the Time To Alert (TTA), is the maximum allowable time elapsed from the onset of the estimation system being out of tolerance until the equipment enunciates the alarm [32].

The integrity, in a standalone GNSS receiver, is guaranteed by internal blocks called RAIM and FDE. By using redundancy of the satellite measurements, RAIM checks the consistency either of the pseudoranges or of the navigation solution [3]. In this thesis we focused in particular on the FDE in the presence of impairments given by the environments around the receiver. We present RAIM and FDE in Section 4.4.

One of the instruments useful to evaluate the performance of a system in terms of integrity is the Stanford diagram (or Stanford plot). It is a graphical tool to explain integrity concepts and their relations for assessing positioning system performance. This diagram provides a clear view of the system performance. For further reading see [33].

In Fig. 2.1 an example of the so-called Stanford Diagram or Stanford Plot is shown. Next, we look briefly at some of the main RAIM algorithms have been proposed in literature.

2.2 RAIM algorithms

The structure of the fault detection of a RAIM algorithm is based on statistical detection theory [34]. The hypothesis testing are two:

1. If a failure exist
2. if so, which is the SV responsible of the fault.

Once identified the faulty SV, it is eliminated from the navigation solution.

In this section, the main algorithms for RAIM purpose with snapshot scheme are presented, such as range comparison [35], Pseudorange residual or Residual Based (RB) [36], and parity method [37]. They provide snapshot schemes and yield identical results under the assumption of equal alarm rate, as shown in [38], where a detailed comparison of these methods is given. Other methods are not based on snapshot schemes, but current and previous measurements are used to take decision about the presence of faults [39]. All of these methods use the pseudorange measurements to detect failures, but it is not the only kind of measurements domain that could be used for this scope as in Section 2.2.4.

2.2.1 Range comparison

Suppose we have a situation with $N_{SV} > 4$ SV in view, it leads to have N_{SV} equations and four unknown (position in cartesian coordinates and clock bias) in vector $\hat{\mathbf{x}}$. The next step is to solve the system of the first four equations (in any arbitrary order), as in absence of noise. The solution is then used to predict the remaining $N_{SV} - 4$ pseudorange measurements $\hat{\boldsymbol{\rho}}$. After that, $\hat{\boldsymbol{\rho}}$ is compared with the actual measured pseudoranges $\boldsymbol{\rho}$ and, if either or both the differences (residuals) are over a certain threshold, a presence of a failure is declared. In case of $N_{SV} = 6$, there are two range residuals $\Delta\rho_1$ and $\Delta\rho_2$ and they can be seen as a coordinates $[\Delta\rho_1, \Delta\rho_2]$ of a point in a test-statistic plane

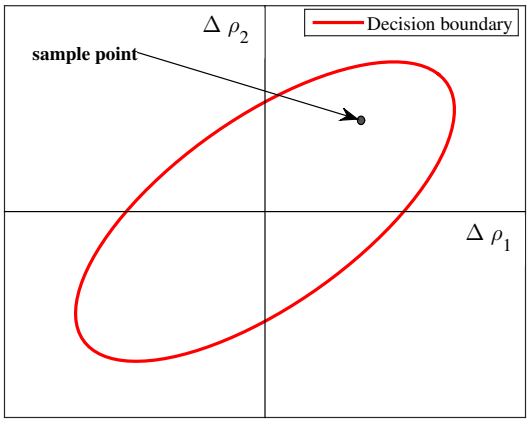

Fig. 2.2 Test statistic plane in case of six SV in view.

as in Fig. 2.2. Then, a decision rule or, graphically, a decision boundary that divides the plane has to be chosen. In case of noise with a Gaussian distribution, the contour of the decision boundary will be elliptical as in example in Fig. 2.2. The contour is chosen by setting the desired alarm rate. If a residual lies within the bound, there is no failure, otherwise a failure is present.

2.2.2 Least-squares residuals

This technique is used to ensure the integrity by checking the consistency of pseudorange measurements. If more than six SV are in view, it is possible to detect and to exclude faulty measurements as well. For this method, we start from the position estimated from Eq. (1.5). Once we get the position $\hat{\mathbf{x}}_{LMS}$ by solving LMS with pseudorange measurements $\boldsymbol{\rho} \in \mathbb{R}^{N_{SV}}$, we can estimate the pseudoranges simply by $\boldsymbol{\rho}_{LMS} = \mathbf{H} \cdot \hat{\mathbf{x}}_{LMS}$. After that, the pseudorange residuals are computed in this way

$$\mathbf{w} = \boldsymbol{\rho} - \boldsymbol{\rho}_{LMS} = [\mathbf{I} - \mathbf{H}(\mathbf{H}^{\mathbf{T}}\mathbf{H})^{-\mathbf{1}}\mathbf{H}^{\mathbf{T}}]\boldsymbol{\rho} \tag{2.4}$$

The vector $\mathbf{w}$ can be used to build a test statistic by means of a scalar product $t = \mathbf{w}^T\mathbf{w}$. If the noise processes that affect the pseudorange measurements are independent and have zero mean Gaussian distributions with same variances, the test statistic t is the sum of the squares of the elements of $\mathbf{w}$ and it

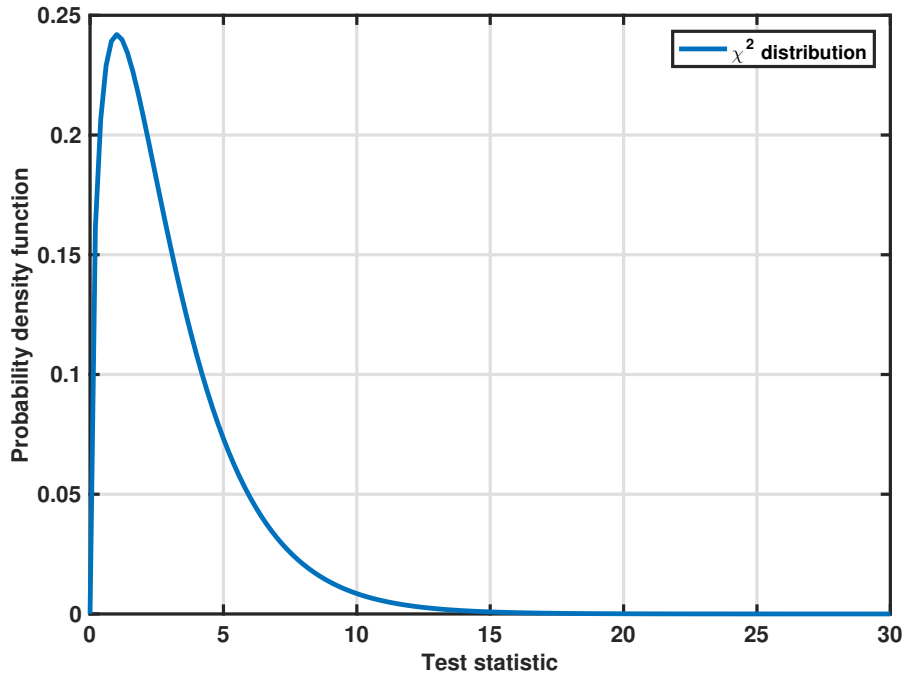

Fig. 2.3 Statistical distribution of the test statistic with three DOF.

has an unnormalized χ^2 distribution with $N_{SV} - 4$ DOF. An example of χ^2 distribution with three DOF can be seen in Fig. 2.3. The threshold used for the fault detection is calculated to meet the required probability of false alarm. Least-squares residuals method is easy to implement in a SDR and the test statistic is always a scalar value, regardless of the number of SV in view [34]. This method is explained in deep and used in Chapter 4 and 6.

2.2.3 Parity method

The parity method is more formal method compare to the previous ones [34, 3]. Starting from the navigation equation

$$\boldsymbol{\Delta\rho} = \mathbf{H}\boldsymbol{\Delta}\mathbf{x} + \epsilon$$

where ϵ is the noise error vector that affects the measurements and it could contain possibles biases. The method performs a linear transformation on the

pseudoranges vector $\boldsymbol{\rho}$ by means of the following relation

$$\begin{bmatrix} \hat{\boldsymbol{x}}_{LMS} \\ -- \\ \mathbf{p} \end{bmatrix} = \begin{bmatrix} (\mathbf{H^T H})^{-1}\mathbf{H^T} \\ -- \\ \mathbf{P} \end{bmatrix} \boldsymbol{\rho} \tag{2.5}$$

where $\mathbf{P} \in \mathbb{R}^{(N_{SV}-4)\times N_{SV}}$ and its rows are mutually orthogonal, mutually orthogonal to the columns of matrix $\mathbf{G}$ and unity in magnitude [34]. The upper part of the left part of the equation 2.5 are the coordinates and the clock bias in the vector $\hat{\boldsymbol{x}}_{LMS}$. The $\mathbf{p}$ vector, called parity vector, is the result of the transformation operated on $\boldsymbol{\rho}$ by the special matrix $\mathbf{P}$, so

$$\mathbf{p} = \mathbf{P}\mathbf{y}$$

The matrix $\mathbf{P}$ can be obtained by QR factorization of the geometry matrix H **??**. Under the assumption of the components of the noise ϵ are independent and zero mean Gaussian random variables, if there are no fault, then $\mathbf{E}[\mathbf{p}] = 0$ and the covariance matrix cov$\mathbf{p} = \mathbf{E}[\mathbf{p}\mathbf{p}^T] = \sigma^2\mathbf{I}$, where σ^2 are the variances associated to each element of ϵ. In the parity method we use the vector $\boldsymbol{p}$ as the test statistic. It can be shown that exist a relation between the parity vector $\mathbf{p}$ and the residual vector $\mathbf{w}$, indeed

$$\mathbf{p}^T\mathbf{p} = \mathbf{w}^T\mathbf{w}$$

so the dimension of the vectors can be different but the magnitudes are the same. This leads to have identical test statistic.

2.2.4 Solution Separation

Instead of using pseudorange measurements, the Solution Separation method [40] is based on the observation of the computed positions starting by the assumption that no more than one SV at a time can have a fault. If there are N_{SV} SV in view, it means there are N_{SV} possible subset obtained by omitting one SV at a time from the all-in view solution. If a failure exists, the faulty SV will miss in one of the subsets and, once the SV is excluded, a faulty free solution will obtained. if there is no fault present, the solutions should stay

bouded around the true position. Then,in the horizontal plane, the maximum observed solution separation can be used as a test statistic. It is a scalar non-negative value that has to be compared against a threshold to decide if the solution contain a faulty SV. In [41] is presented an heuristic method on how to set the threshold and assess the radial error protected.

The Solution Separation method can be further extended to include multiple hypotheses as in [42]. The Multiple Hypothesis Solution Separation is a RAIM algorithm based on the assumption to have more than one simultaneous faulty measurements.

2.3 Augmentation systems

The presented RAIM techniques works with measurements available at the receiver side without any help from external systems. Furthermore, nowadays, the positioning services based on the standalone GNSS receivers performance are not suitable for critical applications like in flight or maritime operations to meet accuracy or integrity user requirements. Thus, augmentation systems have been developed to increase the performance.

These systems introduce the concept of the augmentation of a navigation solution, in particular providing user differential corrections to improve accuracy, reliability, availability and to meet and guarantee particular integrity requirements. Augmentation systems can enhance the performance of a stand-alone receiver thanks to the use of information given by external sources.

To achieve this goal, the receiver may integrate external information of the augmentation system in its positioning calculation. The augmented systems broadcast messages containing several kinds of information like error corrections on clock drift, ephemeris, or ionospheric delay.

The Satellite-Based Augmentation System (SBAS) is one of the augmentation methods. Through the use of additional geostationary satellites, SBAS collects measurements from own ground stations, then the information messages are created and they are broadcasted by geostationary satellites covering large areas of the world. There are several SBAS implementations around the world: the american Wide Area Augmentation System (WAAS), the european Euro-

pean Geostationary Navigation Overlay System (EGNOS), the indian GPS Aided Geo Augmented Navigation (GAGAN) and the japanese Multi-functional Satellite Augmentation System (MSAS).

Other augmentation method is the Ground-Based Augmentation System (GBAS). These methods use radio terrestrial links to cover areas usually limited compared to the coverage of SBAS systems. GBAS provides differential corrections and integrity monitoring in the proximity of airport. The ground stations send messages in Very High Frequency (VHF) band. Another term used in the past by the american Federal Aviation Administration (FAA) referred to GBAS was Local Area Augmentation System (LAAS).

Chapter 3

Multipath Distance Detector Algorithm

In GNSS receivers local effects due to the environment around the antenna can introduce errors on the estimation of the true delay. A typical disturbing effect in urban environment is MP, due to the presence of buildings, moving obstacles like cars, tree and the ground. These disturbing effects could have an impact not only on the accuracy but on the integrity systems as well. In order to satisfy the requirement to detect the signal faults, in this chapter we propose a MP detector working with tracking measurements. The method is based on the well known results of the LAF theory, [43], and works at the correlation layer, so as to provide an early warning to the integrity algorithms. In the following of the chapter it is shown how the LAF coefficients can be used to detect the presence of MP and the validity of the method is proved by simulation.

The work presented in this chapter is focused on environmental effects like MP, that may change the estimation of the true delay of the GNSS signal or more in general, if MP occurs, the multiple reflections change the length of pseudoranges and consequently the estimated position will be wrong. The results presented in this chapter is an extension of the work in [44, 45], that proposes a detection method of the correlation distortions tailored to anomalies caused by MP. In literature, many MP mitigation techniques are described [46, 47], but here the objective is different, as we want to identify the possible

distortion, but not to fix it. The concept of the proposed algorithm comes from a method based on the theory of LAF, already adopted in [48, 49], but rearranged in order to make detection. To design and assess the performance of the detection algorithm, the LAF method was integrated in a SDR receiver and its performance was validated by simulation. These aspects are described in the remainder of the chapter.

This chapter shows the first approach used to start the research work, the presentation of the LAF theory and how to use that for correlation distortions. LAFs are based on methods of *least squares estimation*, are used to solve linear filtering problems without a priori information on the statistical characteristics of the input signal applied to the filter. The basic idea is to build a curve that "best" fit a measured set of N data points $d[1],\ldots,d[N]$. This curve is created as a linear combination of delayed versions of a given discrete-time sequence $u[n]$.

3.1 Linear Adaptive Filter model

An overview of some of *adaptive algorithms* can be find in [50], where adaptive techniques were presented for channel equalization. The algorithm proposed in this chapter is based on LAF [43, 51]. The idea is to represent a set of measured data $d[n]$ as the output of a linear Finite Impulse Response (FIR) filter corrupted by a measurement noise, modeled as Gaussian white random process. This implies that $d[n]$ can be written in the form

$$d[n] = \sum_{k=0}^{M-1} w_k^* u[n-k] + n_0[n] \tag{3.1}$$

where n is the discrete time, $u[n]$ is a given discrete-time input signal, and w_k^* are the unknown parameters of the FIR model that weight delayed versions of the input signal $u[n]$.

The problem is the estimation of the coefficients w_k^* of the FIR model. We introduce the *estimation error* $e[n]$ as the difference between the clean filter output $y[n]$, defined as

$$y[n] = \sum_{k=0}^{M-1} w_k^* u[n-k]$$

and the measured data $d[n]$. Therefore we can write

$$e[n] = d[n] - y[n] \tag{3.2}$$

and we estimate the coefficients w_k^* by adopting the LS method consisting in the minimization of the cost function:

$$\epsilon = \sum_{n=i_1}^{i_2} \mid e[n] \mid^2 \tag{3.3}$$

that is the error energy, where i_1 and i_2 are the limits of the sum. The values assigned to the limits depend on which kind of *data windowing* is chosen. This problem will be addressed in Section 3.1.1 and in Section 3.4.

3.1.1 Data windowing

In order to generate an input rectangular matrix $\mathbf{U}$ from $u[1], \ldots, u[N]$, it is possible to distinguish four different methods, depending on the values of i_1 and i_2 in (3.3). Here we are essentially interested on only two methods and at the end only one will be the correct choice in our application.

- *Covariance method*: this method makes no assumptions about the data outside the interval $[1, N]$, so u_1 and u_2 and $\mathbf{U}$ takes the form:

$$\mathbf{U^H} = \begin{bmatrix} u(M) & u(M+1) & \cdots & u(N) \\ u(M-1) & u(M) & \cdots & u(N-1) \\ \vdots & \vdots & \ddots & \vdots \\ u(1) & u(2) & \cdots & u(N-M+1) \end{bmatrix}$$

- *Autocorrelation method*: this method instead makes assumption that the data prior to time $i = 1$ and after $i = N$ are zero. The matrix $\mathbf{U}$ becomes:

$$\mathbf{U^H} = \begin{bmatrix} u(1) & u(2) & \cdots & u(M+1) & \cdots & u(N) & 0 & \cdots & 0 \\ 0 & u(1) & \cdots & u(M) & \cdots & u(N-1) & u(N) & \cdots & 0 \\ \vdots & \vdots & \vdots & \vdots & \ddots & \vdots & \vdots & \ddots & \vdots \\ 0 & 0 & \cdots & u(2) & \cdots & u(N-M+1) & u(N-M) & \cdots & u(N) \end{bmatrix}$$

The choice on what definition of **U** has to be preferred depends on the specific problem and the one adopted in our application will be indicated later

3.1.2 Normal equations and principle of orthogonality

To solve the *minimum error* problem, it is necessary to use the *principle of orthogonality*:

$$\sum_{n=M}^{N} w_k^* u[n-k] e_{min}^*[n] = 0, \qquad 0 \leq k \leq M-1 \tag{3.4}$$

which affirms that the minimum error time series $e_{min}[n]$ is orthogonal to the time series $u[n-k]$ applied to the taps of a transversal filter of length M for $k = 0, 1, \cdots, M-1$, when the filter is operating in least squares condition. We may derive the system of normal equations by substituting the expression

$$e_{min}(n) = d[n] - \sum_{k=0}^{M-1} w_k^* \cdot u[n-k] \tag{3.5}$$

in (3.4) from which we get

$$\sum_{t=0}^{M-1} w_t \sum_{n=M}^{N} u[n-k] u^*[n-t] = \sum_{n=M}^{N} u[n-k] d^*[n], \qquad k = 0, \cdots, M-1 \tag{3.6}$$

where the left side of the expression contains the time averaged autocorrelation function defined as

$$\phi[t,k] = \sum_{n=M}^{N} u[n-k] u[n-t], \qquad 0 \leq (t,k) \leq M-1 \tag{3.7}$$

while on the right side of (3.6), the summation

$$z[-k] = \sum_{n=M}^{N} u[n-k] d^*[n], \qquad 0 \leq k \leq M-1 \tag{3.8}$$

represents the cross-correlation between the tap inputs and the measured response.

By adopting these correlation terms, (3.6) may be written as

$$\sum_{t=0}^{M-1} w_t \phi[t,k] = z[-k], \qquad k = 0, \cdots, M-1 \tag{3.9}$$

that are the *normal equations* of the linear LS filter.

3.1.3 Re-formulation of normal equations

Now, in order to work with a matrix notation, we rewrite (3.9) by using the following definitions:

- an $M \times M$ time averaged correlation matrix

$$\mathbf{\Phi} = \begin{bmatrix} \phi(0,0) & \phi(1,0) & \cdots & \phi(M-1,0) \\ \phi(0,1) & \phi(1,1) & \cdots & \phi(M-1,1) \\ \vdots & \vdots & \ddots & \vdots \\ \phi(0,M-1) & \phi(1,M-1) & \cdots & \phi(M-1,M-1) \end{bmatrix}$$

- a vector $M \times 1$ that contains time-averaged cross correlation vector between $u[n]$ and $d[n]$: $\mathbf{z} = [z[0], z[-1], \cdots, z[-M+1]]^T$
- a vector $M \times 1$ that contains the coefficients of the least squares filter: $\hat{\mathbf{w}} = [w_0, w_1, \cdots, w_{M-1}]^T$

By using these vectors, the system of normal equations for linear least squares filters can be simply written as

$$\mathbf{\Phi w} = \mathbf{z}$$

In this way, the problem of estimation of $\mathbf{w}$ turns in an inversion matrix problem, that is

$$\mathbf{w} = \mathbf{\Phi}^{-1}\mathbf{z} \tag{3.10}$$

by assuming $\mathbf{\Phi}$ is nonsingular, therefore invertible.

3.2 LAF for multipath detection

The goal of this work is to develop a technique to detect the presence of the MP for integrity purpose, where the goal is to remove the signals affected by strong MP. The basic idea for the detection is to use information coming out from a LAF filter designed so as to decompose the correlations measured during the tracking step as a weighted sum of ideal correlations. To do this, we use the LAF theory previously presented.

The application of the LAF theory to the tracking to decompose the correlation, presents an analogy with the MEDLL already introduced in 1.8. The purpose of both techniques is to estimate the possible presence of the MP but, in case of MEDLL, the estimation is used to correct directly the tracking loops by mitigating the estimated MP. In puour case we want detect and not mitigate. Then the estimation process is different, LAF solves a LS minimization problem in order to find the amplitude and the delay of the reflected rays. Instead, the MEDLL uses a maximum likelihood estimation to find amplitude, the delay and phase of the reflected rays. Moreover, MEDLL generally starts with the assumptions of limited number of rays considered compare to LAF.

The capability of a LAF to model MP phenomena in a GNSS received SIS is described in [48, 49]. Here we use that approach with the specific goal of detecting the presence of MP in the signal of a single GNSS satellite. The method is described in the remainder of this section.

3.3 Multipath Distance Detector algorithm

The Multipath Distance Detector (MPDD) works in parallel with the tracking stage, because it uses the raw data after demodulation and takes delay correction terms calculated by the DLL.The DLL and its update mechanism will be discussed deeply in Chapter 4. The detector does not influence the normal operations of the receiver, but raises an alert when MP, or more in general, distortions affect the signal.

The MPDD algorithm [44] can be implemented inside a software receiver at the tracking stage level. To operate, it needs as input information the

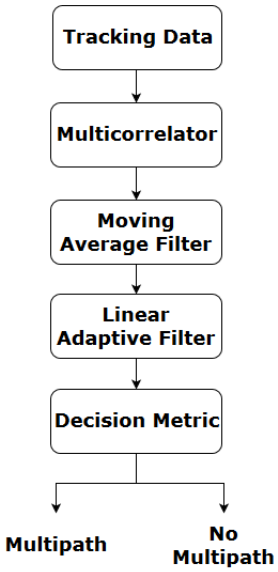

Fig. 3.1 Block scheme of MPDD algorithm.

DLL output; however, it has to be noted that does not provide corrections to the tracking loops. The block scheme of the algorithm with its fundamental components is shown in Fig. 3.1. where the input tracking data are the multicorrelator functions from the DLL. The multicorrelator functions are collected in time and then averaged, in order to limit the noise on one side, and to reduce the computational load on the other side. Then, the output of the average filter becomes the input of the LAF. The LAF decomposes the input multicorrelator signal as a weighted sum of ideal multicorrelation functions, then the weight coefficients are used by the decision metric, to take a decision about the presence/absence of MP.

The detector is composed by 4 elements:

1. Multicorrelator
2. Moving average filter
3. Linear adaptive filter
4. Decision metric

A section will be devoted to describe each of them, except for muticorrelator already described in chapter 1. We need a multicorrelator, but $N_{points} = 3$

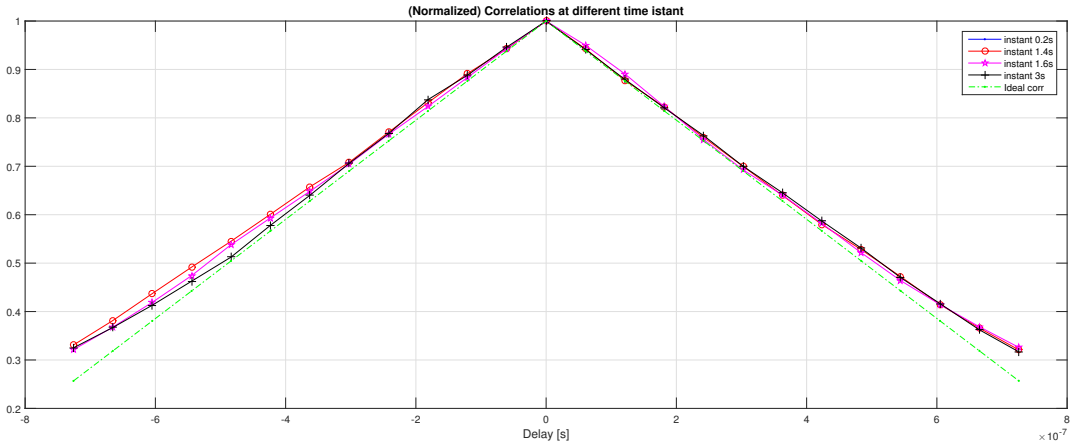

Fig. 3.2 Example of a multicorrelator. The green line represents ideal correlation.

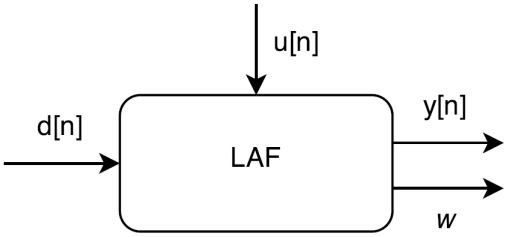

Fig. 3.3 Generic block scheme of a LAF.

points is not sufficient to implement a MPDD. Hence, LAF block needs a multicorrelator with a higher value of N_{points}, as seen in Fig. 3.2. This multicorrelator works independently from the correlator of the DLL, and its *maximum spacing* is $0.5\,T_{chip}$. For example, by using the data of the front-end used in Section 1.6.2, to have a resolution higher than T_s, at least $N_{points} = 16$, for instance, $N_{points} = 20$, so the total number of points of the multicorrelator is $N_{tot} = 41$. In the following we call *correlation sequence* the collection of correlation points obtained at each epoch at the output of the multicorrelator. The last component of the chain is the *Decision metric*, which is the innovative contribution of the present work. Therefore this part will be presented in the next section together with the discussion about the choices made on signals contained in the LAF vectors and matrices.

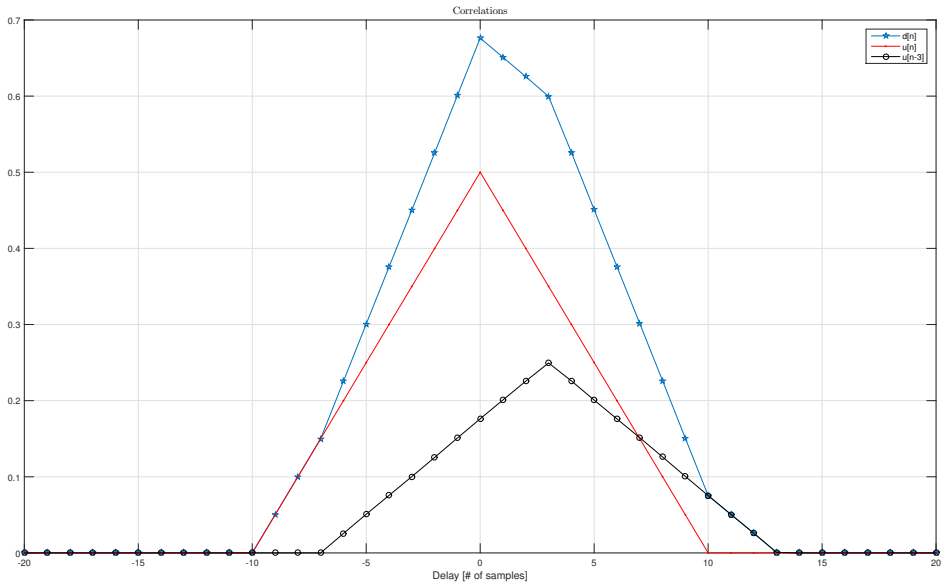

Fig. 3.4 Example of a correlation obtained with two delayed components of $u[n]$.

3.3.1 LAF component block

In section 3.1 it was introduced the theory of the LAF, that is valid for generic signals. Here we use the LAF scheme, depicted in Fig. 3.3, by adopting the method suggested in [48] and [49], where $d[n]$ is the measured correlation sequence and $u[n]$ is the ideal correlation sequence

$$u[n] = \sum_{m=-k}^{k} C_m^*(m \cdot \Delta sp) C_m((m+n) \cdot \Delta sp)$$

where Δsp is the resolution of the multicorrelator, that is in general different from T_s. With this scheme we are able to fit the measured correlation sequence with an approximated correlation $y[n]$, which is a weighted sum of delayed versions of the ideal correlation. An example is in Fig. 3.4, which shows a correlation obtained with two delayed components of $u[n]$.

The LAF method allows the estimation of the filter coefficient vector $\mathbf{w}$, which can be used to decide about the presence of possible MPs. Therefore a key point of the algorithm is the computation of the vector $\hat{\mathbf{w}}$, which can be

done by using (3.10), where

$$\mathbf{\Phi} = \mathbf{U}^H \mathbf{U}$$

$$\mathbf{z} = \mathbf{U}^H \mathbf{D}$$

and $\mathbf{D}$ is the windowed measured correlation from index M to N. The first point to note is that the length M of the LAF filter also impacts on the length of $\mathbf{D}$. Since $\mathbf{D} = [d[M], d[M+1], \cdots, d[N]]^T$, more taps we choose, less points of the measured correlation are used by the LAF algorithm. In our application we use a portion of the signal containing N_s samples and we measure $2N_s+1$ correlation points in the region around the peak. Since only the correlation samples from M to $N = 2N_s+1$ are used, M has to be lower than $(2N_s+1)/2$, in order to preserve the samples close to the peak. The value of M also determines the computational load due to the fact that the matrix to invert becomes bigger, as the filter becomes longer. The *M-to-N ratio* defined as

$$MNR = \frac{M}{2N+1}$$

must be chosen $\ll 50\%$. For instance, if $M = 10$ and $N = 20$, $MNR = 0.2439$. Notice that in our application we are not interested in the single components of $y[n]$, since our goal is not to mitigate MP effects, but rather to exclude satellites with severe MPs.

Energy analysis

First of all, it's important to underline what we expect from the $\mathbf{w}$ vector, that is, what we can infer from the vector about MP and more in general the presence of an undesired distortion in the measured correlation.

In an ideal static situation between transmitter and receiver with no Doppler, no MP and no noise effects, $\mathbf{w}$ will contain only the first component ($w[1]$) and the other coefficients are all zero. This because the measured correlation $\mathbf{D}$ exactly coincides with the ideal correlation except for a normalization term w_{LOS}. In all the other cases the presence of undesired components in the received SIS modifies all the elements of $\mathbf{w}$. In the presence of LOS and a single ray of MP with a specific delay and no noise, $w[1]$ and the element of $\mathbf{w}$ corresponding to the delay will be different from zero.

Noise complicates the identification of MP or other distortions, because spreads energy on all the elements of **w**. In order to mitigate this effect we use an averaged correlation sequence, as it will be explained in section 3.3.3.

Another consideration to take into account is that the MP delay is in general a quantity $\in \mathbb{R}$, while in the discrete-time domain only delay $\in \mathbb{N}$ can be represented. This means that the expression $y[n] = \sum w_k^* u[n-k]$ used by the LAF to represent the measured correlation can properly model only a finite set of possible delays, therefore the method has not an infinite resolution. For example a delay of 1 correlation sample is properly modeled by $u[n-1]$. Instead, it is probable that a real delay is not proportional to the resolution of the LAF filter or, in other words, the delay between two correlation samples cannot be modeled by a single replica of $u[n]$.

The delay is represented in that case by more than one elements of the **w** vector.

It is evident that the information about the presence of MP is contained in the signal:

$$y_{side}[n] = y[n] - w_{LOS} \cdot u[n]$$

that is the curve of side components, obtained by subtracting the approximated correlation and the 0-delayed ideal correlation weighted with the calculated LOS coefficient.

In order to have an idea of the information on MP possibly embedded in $y_{side}[n]$ some simulation experiments have been performed. A GPS signal with $C/N_0 = 45$ dBHz has been generated with no MP in the initial part, and a 1 ray MP added in the time interval (t_1, t_2), where $T_1 = 15$s and $t_2 = 20$s, with MSR $(MSR) = -6$dB. The simulation results are shown in Fig. 3.5 which shows the energy of the vectors at the LAF output. In the top left there is the evolution in time of the energy of the LOS component; in top right the evolution of the energy of the side components; in lower left and lower right respectively the energy of approximated correlation and measured one. As expected, the energy of the side components increases during the MP stage. We can say that in the correlation domain the energy of $y[n]$ well approximates the energy of $d[n]$.

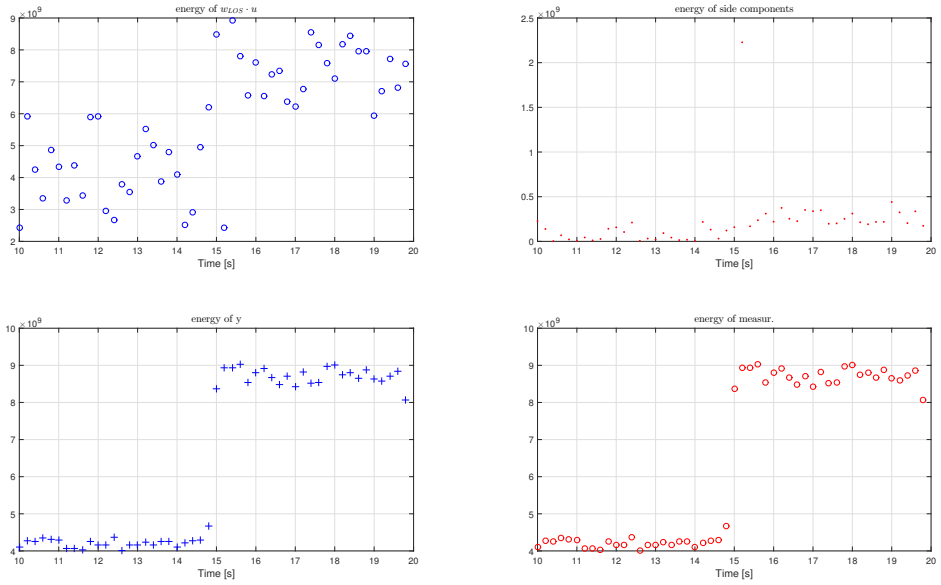

Fig. 3.5 Energy analysis of LAF input and output signals.

The energy of the error introduced in (3.5) is normalized over the energy of $d[n]$ and the expression is

$$E_e[n] = \sum_{n=-k}^{k} \frac{|d[n] - y[n]|^2}{|d[n]|^2}$$

This parameter is represented in Fig. 3.6, where we note that the energy of the relative error is on the order of 10^{-4} and it maintains constant its order of magnitude for both MP and no MP stage.

3.3.2 Decision metric

First of all, which type of information can we extract from **w** vector? LAF decomposes the signal as a linear sum of delayed ideal correlations; this means that, for instance, in the case we have LOS and another reflected ray delayed as in Fig. 3.4, only $u[n]$ and $u[n-3]$ are present in the measured correlation and the **w** vector should contain non-null values only in the first and third position. In the general case with a ray with a fractional delay, there will be an additional coefficient given by the filter in order to well approximate

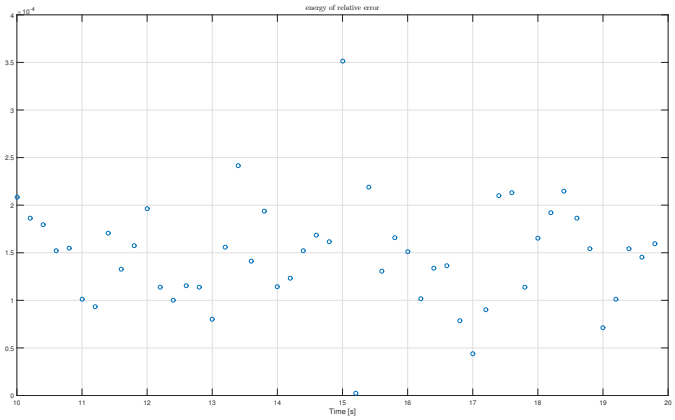

Fig. 3.6 Energy of the error between $d[n]$ and $y[n]$.

the input signal. In the presence of noise all coefficients are non-zero, since noise spreads energy into the whole vector, as shown in Fig. 3.7. The idea is not to use a simple threshold on the coefficients, but to find a way to use all information inside the $\mathbf{w}$ vector. The key point is to consider the $\mathbf{w}$ vector in a coefficients space, where we know that in the absence of noise and MP, the ideal LOS vector $M \times 1$ is $\mathbf{w}_{LOS} = \beta \cdot [1, 0, \ldots, 0]^T$ where β is only a normalization constant. An example can be seen in Fig. 3.8. After the computation of the vector coefficients at the output of the filter $\mathbf{w}_{out}$, the algorithm calculates the geometrical distance between $\mathbf{w}_{out}$ and a set of specific vectors, by using the square distance criterion. This dictionary of vectors contains possible binary combinations of vectors with dimension $M \times 1$ (potentially there is a very high number of entry in the dictionary). Therefore the dimension of the comparison set depends strictly on M, that increases its relevance not only as length of the filter. Inside the set there are "samples" vectors that represent several situations like only LOS, LOS and 1 ray or more of MP with different delays etc. When the distance between $\mathbf{w}_{out}$ and $\mathbf{w}_{LOS}$ is greater than other, the algorithm detect possible presence of distortions. In formula we have

$$E_{LOS} = \|\mathbf{w}_{out} - \mathbf{W}_{LOS}\|^2$$

and

$$E_k = \|\mathbf{w}_{out} - \mathbf{W}_k\|^2 \qquad k = 1, 2, \ldots N_v - 1$$

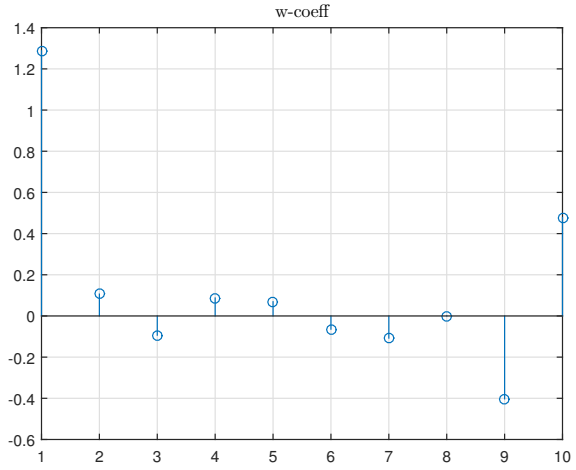

Fig. 3.7 $\mathbf{w}_{out}$ in case of only noise and $C/N_0 = 45$ dBHz.

and we decide that anomalies are present if

$$E_k < E_{LOS} \qquad k = 1, 2, ...N_v - 1$$

or

$$\min_{k=1,2,...N_v-1}(E_k, E_{LOS}) \neq E_{LOS}$$

where W is the matrix dictionary $M \times N_v$ that has sample vectors along the columns. A preliminary important consideration is that we consider the detection of MP in the presence of the LOS signal. This implies that all the normalized sample vectors have the first coefficient set to 1. The others remaining coefficients are multiplied by an additional parameter $\alpha \in (-1, 1) \setminus \{0\}$ that tunes the amplitude of the considered delayed replicas. The next problem will be to choose appropriate values for α. If $\mathbf{w}_{out}$ is recognized as a vector with MP, to raise an alert is not sufficient. The MP phenomenon is critical if it has strong distortion effects on correlation and its duration is more than few hundred milliseconds. In conclusion, the threshold is moved from coefficients to temporal duration.

Independently from the value of M and by keeping the number of correlation points constant, we will avoid to consider last two values of w, which are the most delayed replicas. The last two coefficients on the border have low C/N_0, the correlation is weak, so from the point of view of detection, we may reduce

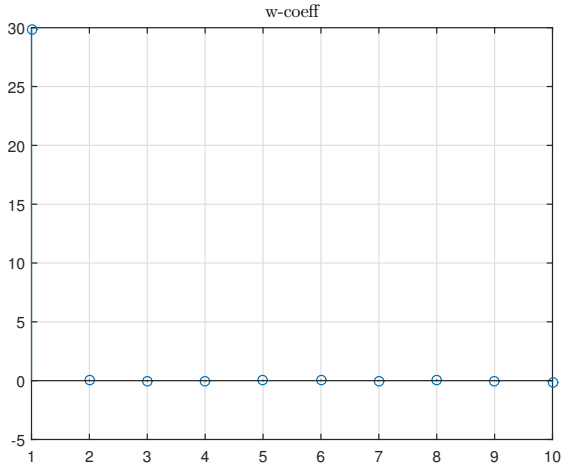

Fig. 3.8 w_{out} in case of no noise and no MP.

the effect of the noise by not using them. In the example in Fig. 3.9, with $C/N_0 = 42$ dBHz, without MP and $M = 10$, the power of the 9th and 10th component are consistent and the algorithm may confuse distortion caused by the noise for MP. The situation is more clear by viewing the vector $\mathbf{w}_{out}$ depicted in Fig. 3.10.

A possible strategy to improve the detection is to update the vectors on the dictionary, calculating the best ideal vectors by adding information about noise variance which is related to C/N_0. This implies the existence of several dictionaries specified for at least sample values of C/N_0. i.e. 40, 42, 45 dBHz.

Example

Let's suppose to work in condition with LOS and 1 reflected ray (with less power). We choose $M = 8$, so $\mathbf{w}_{out}$ is 8×1; the set should contain $N_v = 2^M = 256$ vectors, but they are less than this number, in fact $M_{new} = M - 2 = 6$, that implies $N_v = 2^6 = 64$ vectors. Now, we consider that we have an environment that receives always the LOS consequently, we remove all the vectors that don't have 1 as a first coefficient but 0, so N_v will be halved. Eventually, are needed 32 distance calculations to establish if there is distortion within the time window.

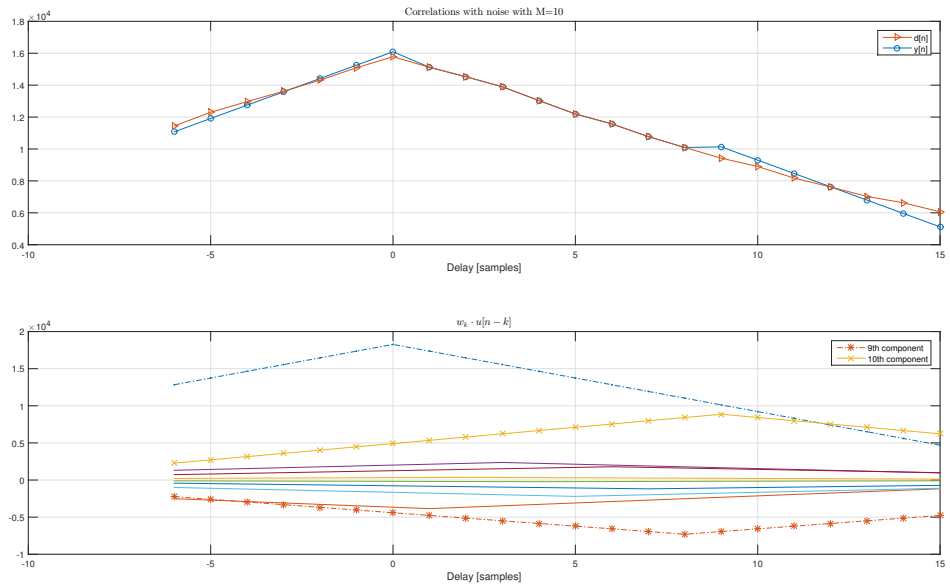

Fig. 3.9 Weighted replica and w_{out} in case of only noise and $C/N_0 = 42$ dBHz.

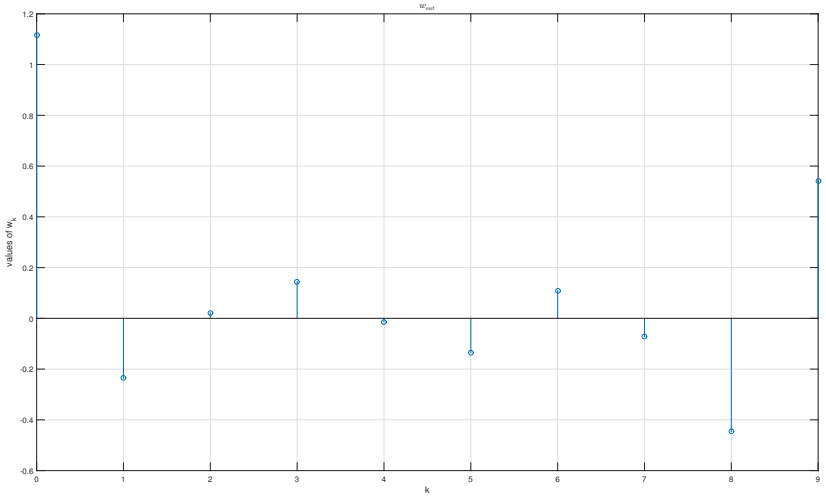

Fig. 3.10 Values of w_{out} at $C/N_0 = 42$ dBHz, referred to the figure example 3.9.

3.3.3 Cross-correlation moving average

The LAF-based detector described in this document requires the measurements of a correlation sequence with of a significant number of points. In order to distinguish the effects of the noise from the effects of the MP, the noise in the correlation sequence should be attenuated as much as possible. To reduce the noise effect, the first step, after the multicorrelator, is a cross-correlation moving average. Two possible implementation of this filter are *continous moving average* or *block moving average*. The first one is a moving average filter with overlap between slices of the signal, the second one instead operates independently the average on slices, without overlapping. For this implementation and to reduce computational load, the block moving average is chosen. During the processing, on every integration time of the incoming signal a correlation sequence with N_{tot} points is computed, and stored. Then we supposed that, if a strong MP is present, it has the same nature (same delay) in a time interval including many measurement epochs. In this case we can store and average the correlation sequences, to reduce the noise effect. For example a MP which lasts about 50 ms is present in 50 non-overlapping correlation sequences. In the examples shown in this section the following parameters have been used:

- $C/N_0 = 45$ dBHz
- A simulation duration of 22 s.
- No MP in the first 15 s and last 2 s.
- MP from 15 s to 20 s.
- The MP is one ray with amplitude halved respect to the direct path, and delay $0.30548 \mu s$.

Concerning the moving average filter, we set $M = 10$ for all the cases (this choice will be discussed in depth later). Fig. 3.11 is divided in four subplots. The upper-left graph shows the measured and ideal correlation in a particular instant. In the upper-right graph the measured correlation and the estimated correlation by the LAF are shown. The bottom-left shows the estimation error between the input of the LAF (measured correlation) and the output (estimated correlation). In the last graph, in bottom-right plot is shown the $\hat{\mathbf{w}}$ vector.

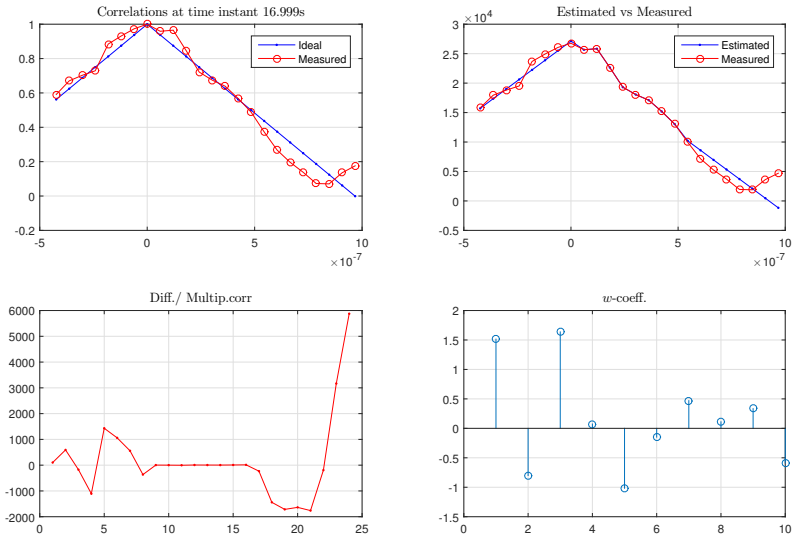

Fig. 3.11 Correlations and coefficients and 1 ray of MP presence.

These plots are taken during the MP part and the presence of the MP could be detected since the moving average window has short duration of 20 ms. Therefore it is important to attenuate the effects of the noise, visible in the resulting $\hat{\mathbf{w}}$ vector of the LAF.

To underline this, let's consider a time window of 1 ms, equal to the integration time, so it means there is no average on data. It is possible to see the distribution of the amplitude of the coefficients in Fig. 3.12 and to observe that the 1-st coefficients have approximately the same normal distribution with different averages (see Section 3.6).

In Fig. 3.13 are shown correlations, in different time instants, which can be affected by the noise. Instead, in Fig. 3.14, the correlations are also affected by MP in the instants from 15 s to 20 s. Both of the figures use a moving average window of 1 ms. With respect to the previous figures, in Fig. 3.15 is visible the denoising effect, due to the average over a time window of 50 ms.

Other example of average time window is in Fig. 3.16, where the moving average is calculated over 200 ms. This value together with 500 ms, is typically used for the simulations, especially when C/N_0 is lower than 45 dBHz.

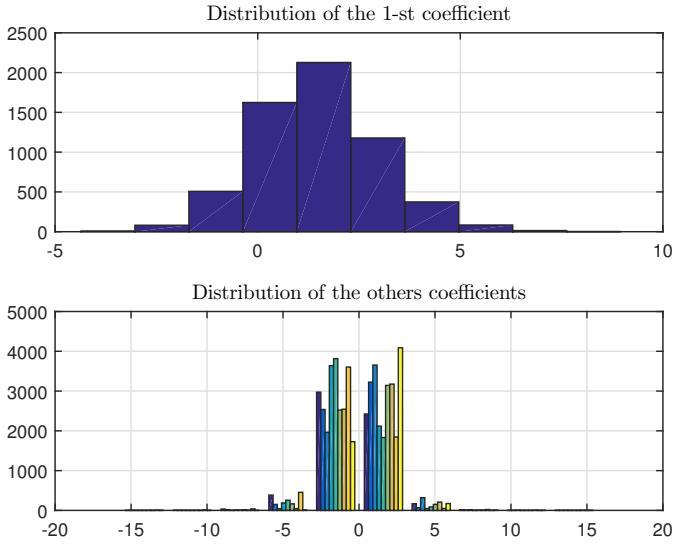

Fig. 3.12 Distribution of coefficients on a duration of 6 s without MP.

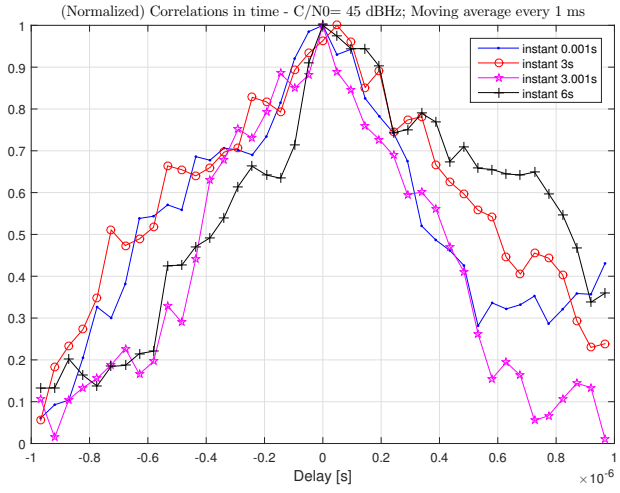

Fig. 3.13 Correlations at different time instant, without MP and where it is difficult to identify the peak for all correlations. Moving average window of 1 ms

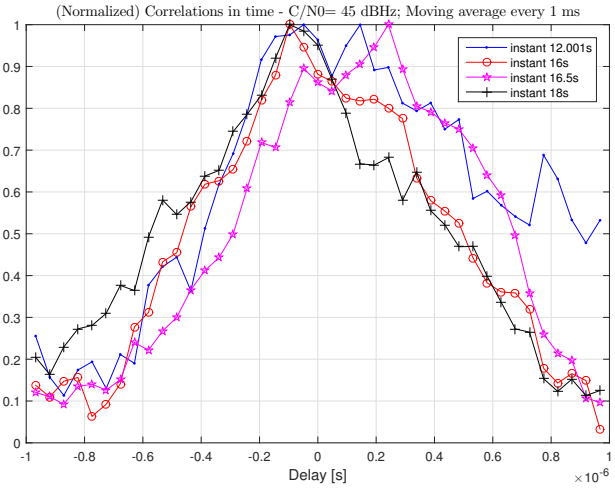

Fig. 3.14 Correlations at different time instant, with MP and where it is difficult to identify the peak for all correlations. Moving average window of 1 ms

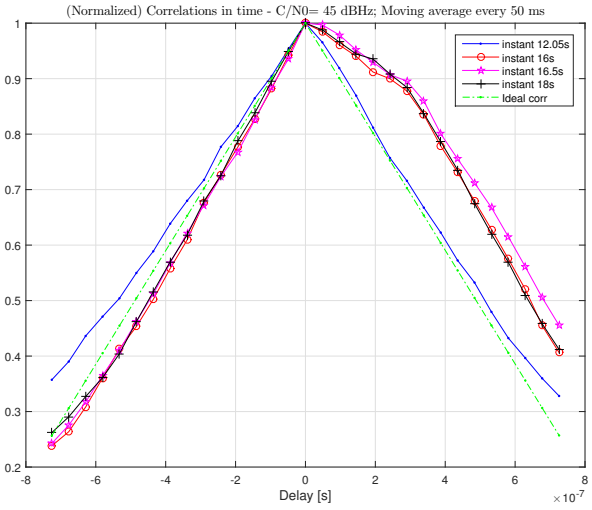

Fig. 3.15 Correlations at different time instant, with/without MP and moving average window of 50 ms.

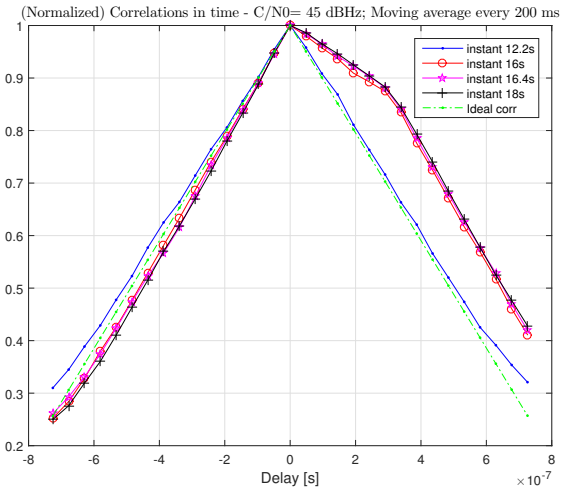

Fig. 3.16 Correlations at different time instant, with/without MP. Moving average window of 200 ms

Another reason to use moving average is to reduce the computational load, because for instance the case with 1 ms of window implies that the LAF's weights have to be evaluated at each millisecond instead of 50, 200, 500 ms. Moreover the analysis to have information at level of 1 ms is not so useful and very noisy.

3.3.4 Peak Alignment problem

This section will address the problem of the alignment of the peak of the correlation function. In fact the points of the correlation have to be correctly aligned before performing the moving average operation. Peak alignment is important to avoid to give false information to the detector block and to better compute the w vectors. The situation of the following simulations is this:

- $C/N_0 = 45$ dBHz.
- 200 ms of time window.
- 6 seconds of the signal, with last 3 s with MP.

Obviously, the peak of correlation is the maximum of the function, so the problem is to fix the maximum value of the correlation. In ideal case, there

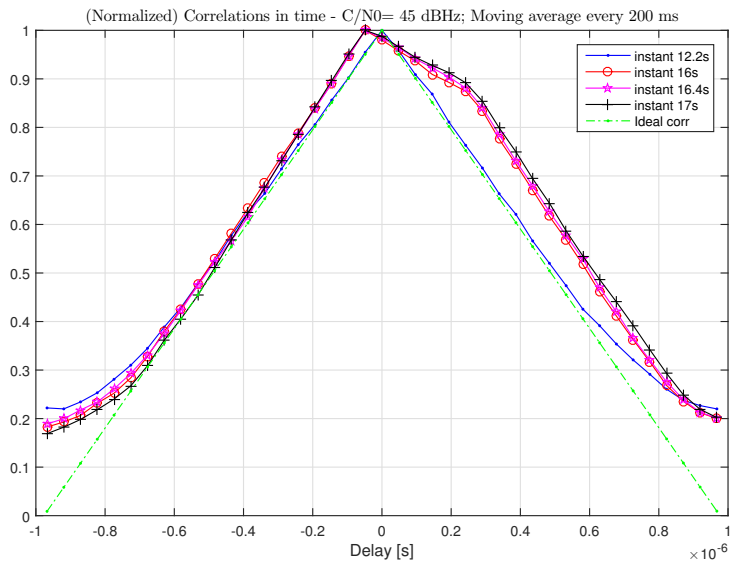

Fig. 3.17 Correlations not aligned but averaged (istants after 15 s have MP together with the signal).

is no problem, and the identification of the maximum is a simple operation. On the contrary, in the presence of noise, as in the example of Fig. 3.13, the correlation is not a perfect triangle and especially the points around the true peak could be higher than the peak itself. In conclusion, due to noise, it is possible to find a wrong maximum peak. The moving average reduces the quantity of noise giving regular correlation points as shown in Fig. 3.17, but if we observe the case of MP presence, the peak is not aligned as in the case of only noise presence. The problem is how to do the alignment, because the average after the alignment risks to smooth not only the noise, but also the MP as shown in Fig. 3.18, so degrading the detection capability.

The adopted solution is to compute the average before the alignment. If a strong MP persists during the time with the same characteristics, the average allows us to highlight the distortion and the true peak, as shown in Fig. 3.19 where the alignment is done after the average.

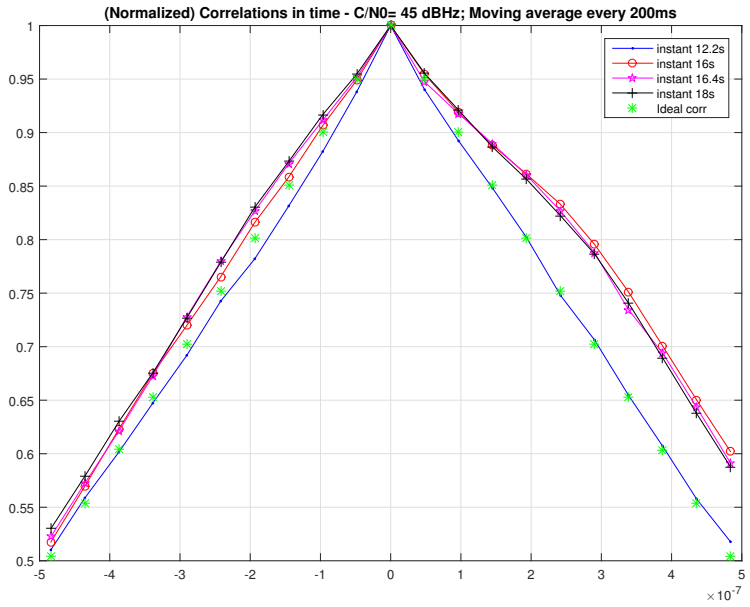

Fig. 3.18 Smoothing effect on correlations by using alignment before the average (istants after 15 s have MP together with the signal).

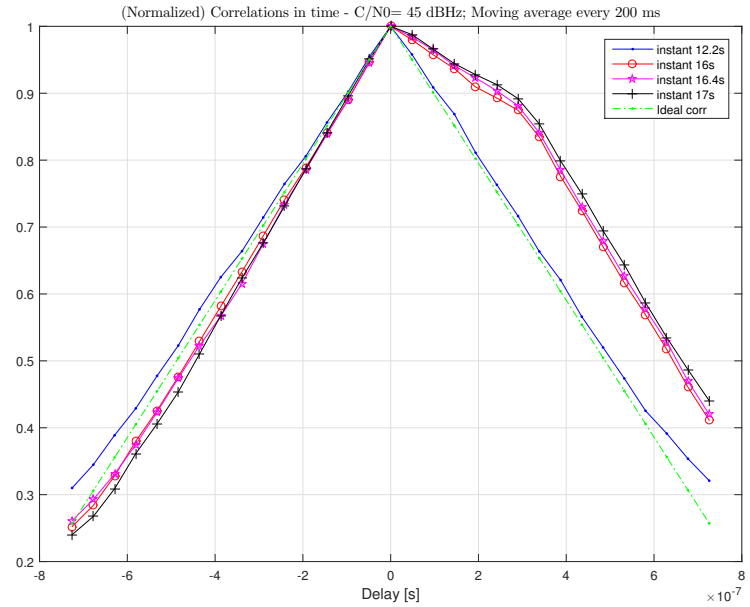

Fig. 3.19 Correlations by using alignment after the average (istants after 15 s have MP together with the signal).

3.3.5 Simulation results

To validate the results obtained by simulation, we used data generated with N-Fuels, that is a GNSS signal simulator [52]. This part of the work considers four main types of environment depending on the characteristics: Open, Rural, Suburban, Urban. The first problem was to establish a correct tuning of parameters of the signal simulator, to work in a realistic scenario. To do that, in section 3.3.6 are presented values which were useful to set up, taken from the research in [53]. It was possible to determine, for different environments, some MP characteristics, i.e. average number of reflected rays etc. In section 3.3.7 it will be shown the profiles of the MP and the results obtained with the complete detection algorithm.

3.3.6 Multipath characteristics

This brief section will introduce some typical values useful to validate the analysis. From the the receiver point of view, the most dangerous MP or distortion problem is when it has a high *MSR* and this situation continues over time. In table 3.1 are reported some typical values of *Signal-to-Multipath ratio* (*SMR*) that is defined with opposite sign respect to *MSR*, in the case to have elevation angle of $E = 25°$. We are interested, in particular to the last case of the table, urban environment, where there is the lowest *SMR* (highest *MSR*).

	Multipath Characteristics ($E = 25°$)	
Environment	**Mean SMR (dB)**	**Typ. Path Delay (m)**
Open	27.5	26
Rural	13.5	57
Suburban	20.5	56
Urban	6.0	51

Table 3.1 MP characteristics for different environment with elevation angle of 25° [53].

Another important parameter to consider is the average number of rays present in the incoming signal. Instead to have a single reflected ray with a certain power, it may be possible to have many rays with less power. In [53], it is shown a mean number of reflected rays for each type of environment. For

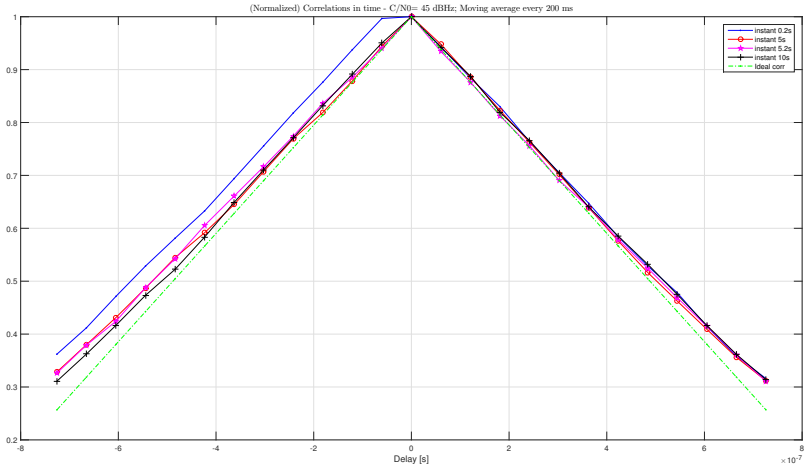

Fig. 3.20 Correlations at different epochs without MP.

the urban case, the worst one, the maximum number of reflected rays in the case of an elevation angle $E = 25°$, is set equal to 5.

3.3.7 Multipath profiles

As already mentioned in the introduction of the chapter, here we consider many different scenarios with and without MP, the effects of different moving average windows, etc. We start with the first case, that we consider as a reference good case. In Fig. 3.20 some correlation functions are shown in several time instants on a dataset with duration 22 s and $C/N_0 = 45$ dBHz. These correlations are not referred to a single epoch of 1 ms but they are an average on a window duration of 200 ms. Here the istants before 10 s are shown. For all the cases, α can be 0.3 or 0.5, so the peak of MP will be 0.3 or 0.5 than the peak of the LOS.

Figs. 3.21 and 3.22 show the results of the detector, in terms of computed distances (upper graph) and detector output (lower graph). The detection output is the index in the dictionary that indicates which vector is closer to $\mathbf{w_0}$. If the index is different from 1 (the index of the $\mathbf{w_{LOS}}$), the distortion is present. The results are shown in the time interval from 10 s to 22 s.

Now in Figs. 3.23 and 3.24, the conditions are the same as before, but C/N_0 decreases to 42 dBHz. The performance is still good, but during MP

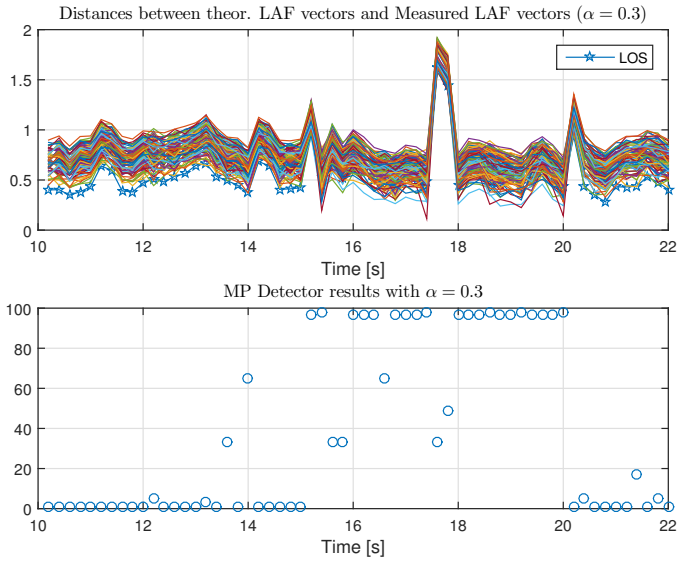

Fig. 3.21 Distances and detector results in case with $\alpha = 0.3$ and $C/N_0 = 45$ dBHz.

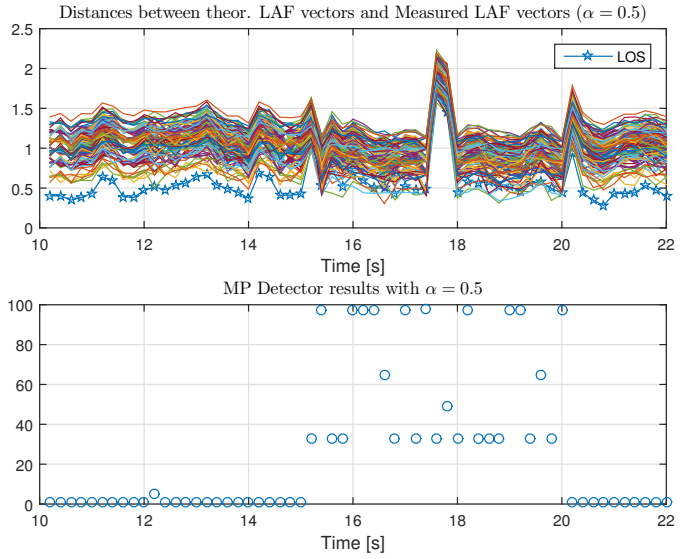

Fig. 3.22 Distances and detector results in case with $\alpha = 0.5$ and $C/N_0 = 45$ dBHz.

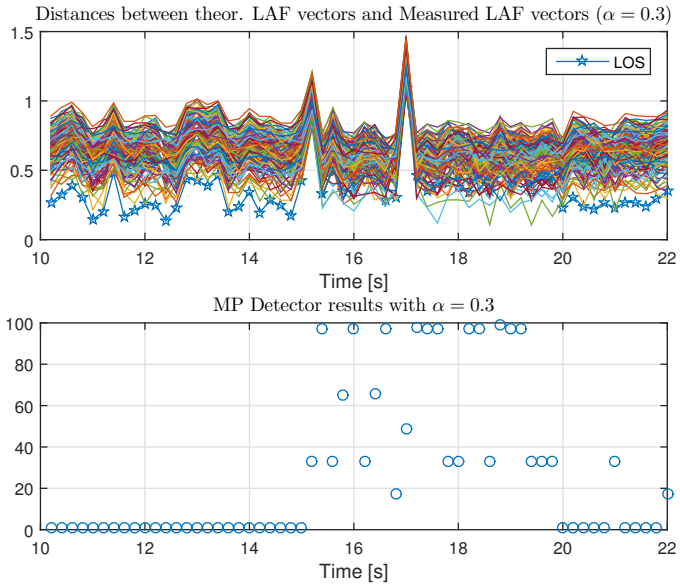

Fig. 3.23 Distances and detector results in case with $\alpha = 0.3$ and $C/N_0 = 42$ dBHz.

stage, there is some missed detection in case of $\alpha = 0.5$. The last case is in Figs. 3.25 and 3.26, where $C/N_0 = 40$ dBHz. The performance is very similar for both values of α.

Multiple rays

Until now, all the examples and figures have only one reflected ray. In Figs. 3.27 and 3.28, there are two replicas with $MSR_1 = -6$ dBHz and $MSR_2 = -8$ dBHz and different delays $\tau_1 = 0.29\mu$s $\tau_2 = 0.3548\mu$s.

In the last case shown in 3.29 and 3.30, with $C/N_0 = 42$ dB, there are five MP rays with $MSR_1 = -9$ dB, $MSR_2 = -7$ dB, $MSR_3 = -6$ dB, $MSR_4 = -7$ dB and $MSR_5 = -8$ dB. The delays are $\tau_1 = 0.15\mu$s, $\tau_2 = 0.19\mu$s, $\tau_3 = 0.25\mu$,s $\tau_4 = 0.32\mu$s and $\tau_5 = 0.39\mu$s. As we expect, the detection method works both in the simplest cases with two rays and with multiple rays. This because the resulting distortion is more important than the effective number of rays.

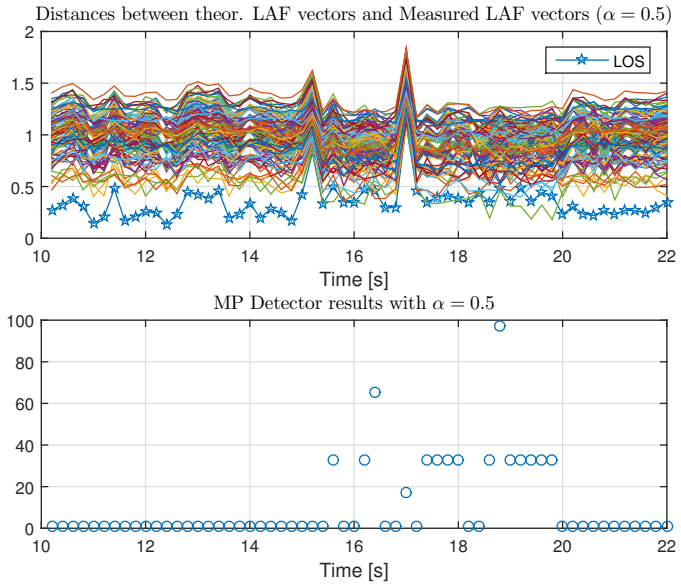

Fig. 3.24 Distances and detector results in case with $\alpha = 0.5$ and $C/N_0 = 42$ dBHz.

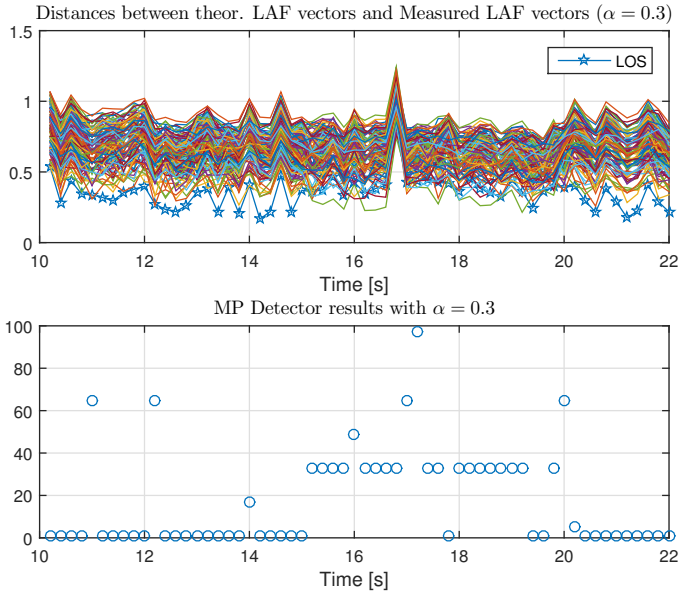

Fig. 3.25 Distances and detector results in case with $\alpha = 0.3$ and $C/N_0 = 40$ dBHz.

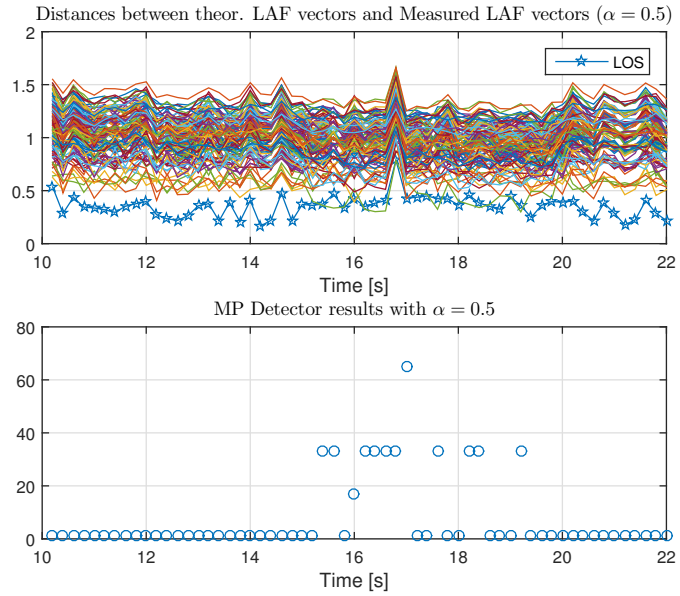

Fig. 3.26 Distances and detector results in case with $\alpha = 0.5$ and $C/N_0 = 40$ dBHz.

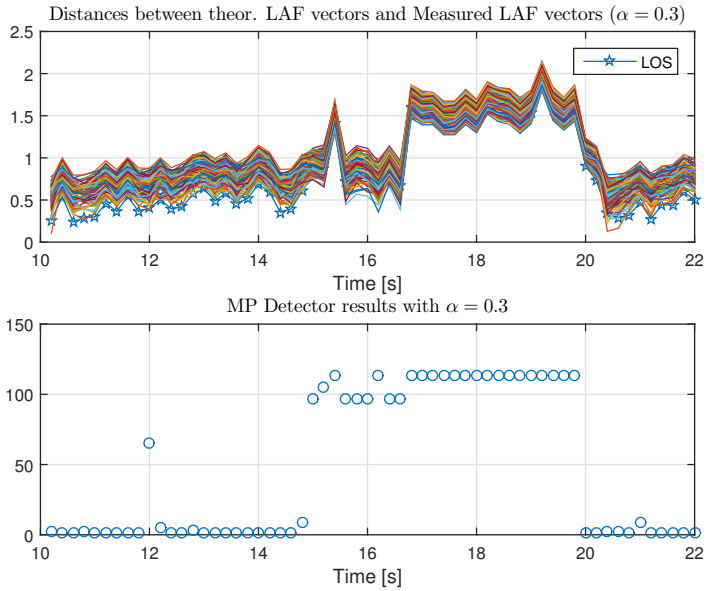

Fig. 3.27 Distances and detector results in case with $\alpha = 0.3$ and $C/N_0 = 45$ dBHz. MP has two replicas with $MSR_1 = -6$ dB and $MSR_2 = -8$ dB and different delays $\tau_1 = 0.29\mu$s $\tau_2 = 0.3548\mu$s

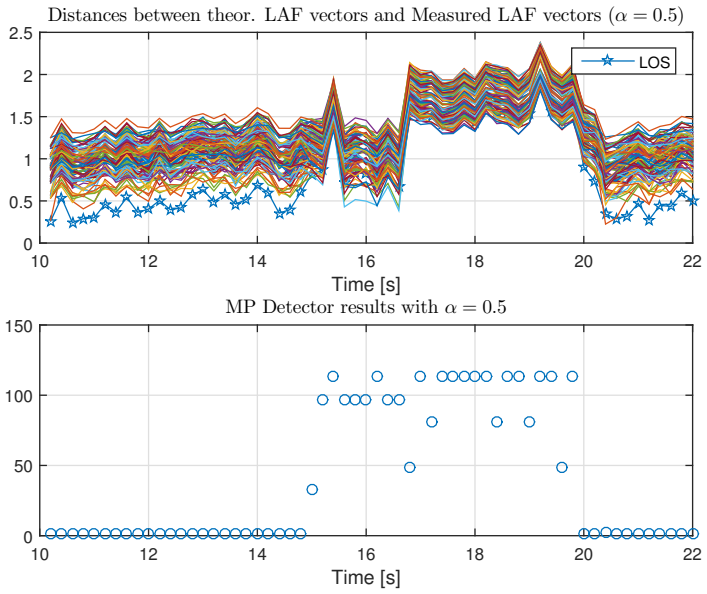

Fig. 3.28 Distances and detector results in case with $\alpha = 0.5$ and $C/N_0 = 45$ dBHz. MP has two replicas with $MSR_1 = -6$ dB and $MSR_2 = -8$ dB and different delays $\tau_1 = 0.29\mu$s $\tau_2 = 0.3548\mu$s

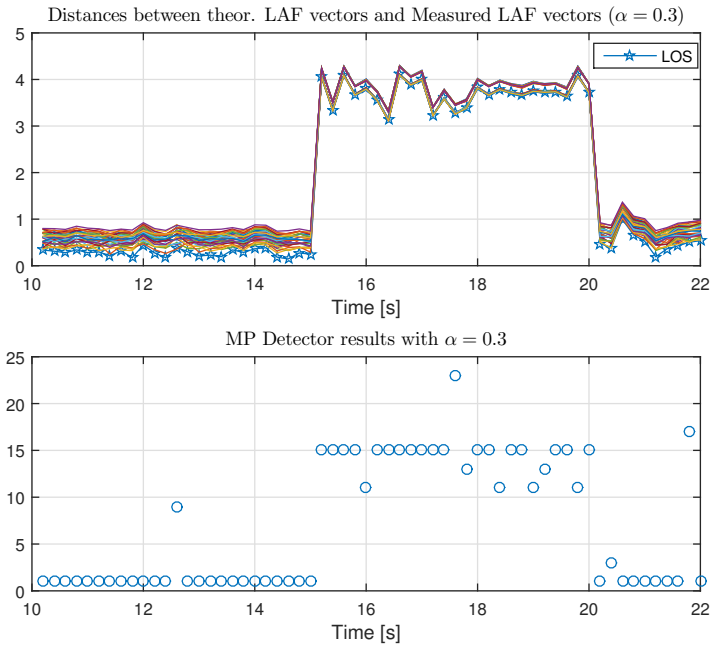

Fig. 3.29 Distances and detector results in case with $\alpha = 0.3$ and $C/N_0 = 42$ dBHz. MP has five rays with $MSR_1 = -9$ dB, $MSR_2 = -7$ dB, $MSR_3 = -6$ dB, $MSR_4 = -7$ dB and $MSR_5 = -8$ dB. The delays are $\tau_1 = 0.15\mu$s, $\tau_2 = 0.19\mu$s, $\tau_3 = 0.25\mu$,s $\tau_4 = 0.32\mu$s and $\tau_5 = 0.39\mu$s

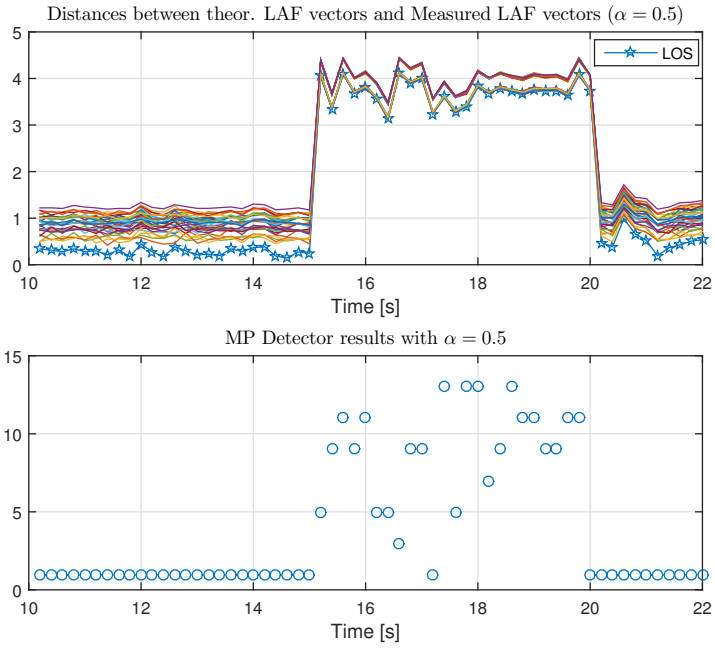

Fig. 3.30 Distances and detector results in case with $\alpha = 0.5$ and $C/N_0 = 42$ dBHz. MP has five rays with $MSR_1 = -9$ dB, $MSR_2 = -7$ dB, $MSR_3 = -6$ dB, $MSR_4 = -7$ dB and $MSR_5 = -8$ dB. The delays are $\tau_1 = 0.15\mu$s, $\tau_2 = 0.19\mu$s, $\tau_3 = 0.25\mu$,s $\tau_4 = 0.32\mu$s and $\tau_5 = 0.39\mu$s

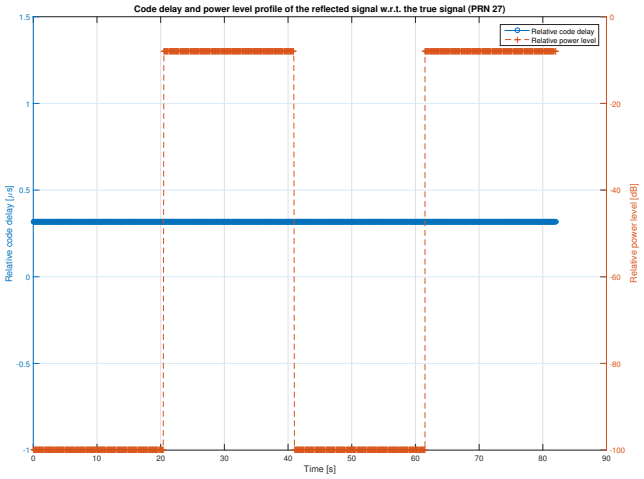

Fig. 3.31 MP profile, delay and power during the time.

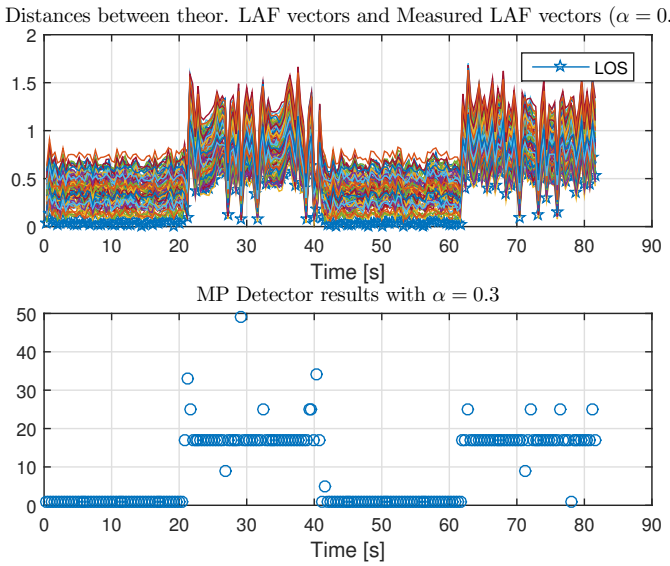

Fig. 3.32 Calculated distances and detector results for long dataset with $C/N_0 = 43$ dBHz, $\alpha = 0.3$ and $M = 8$.

3.3.8 Detection and error probability

In this subsection, we try to estimate the detection and error probability (P_d and P_e). For this type of simulation, we use longer dataset in order to plot the *probability of detection* and *probability of false alarm* for several value of C/N_0. The MP profile is shown in Fig. 3.31, where the duration of the dataset is 82 s and where every 20.5 s, the *MSR* rises from -100 dB to -8 dB and viceversa, with a fixed delay of 0.31748μs. The results for the detector are shown in Figs. 3.32, 3.33 and 3.34 respectively for $\alpha = 0.3$, $\alpha = 0.4$ and $\alpha = 0.5$ with $M = 8$. It is possible to see that the performance of the detector are influenced by α values.

Figs. 3.35, 3.36, 3.37 and 3.38 show the results referred to the previous dataset, in terms of probability to detection and probability to commit error, with a growing value of C/N_0 for several fixed values of α and for $M = 8$ and $M = 10$. The graphs show that it is possible to identify an optimal α to define the presence of the MP, in case of the example with $MSR = -8$ dB, the optimum is between $\alpha = 0.3$ and $\alpha = 0.4$. From the case with $M = 8$ to $M = 10$ the situation doesn't change very much so it may be possible to reduce the

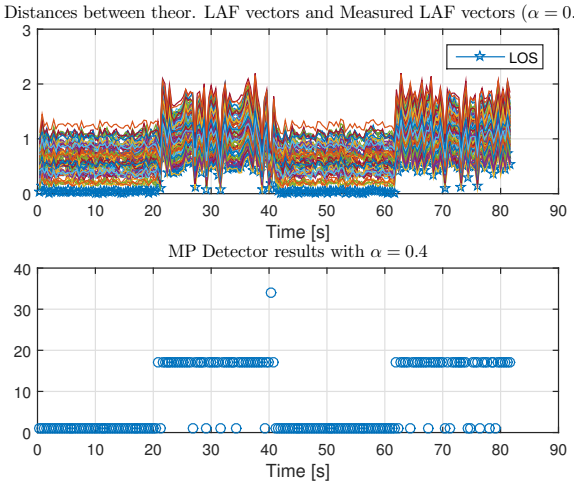

Fig. 3.33 Calculated distances and detector results for long dataset with $C/N_0 = 43$ dBHz, $\alpha = 0.4$ and $M = 8$.

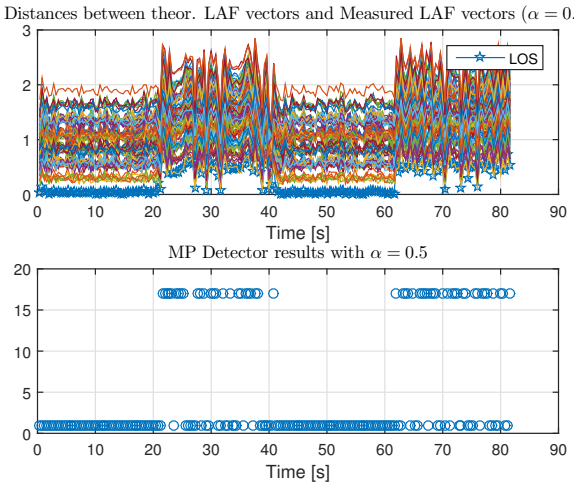

Fig. 3.34 Calculated distances and detector results for long dataset with $C/N_0 = 43$ dBHz, $\alpha = 0.5$ and $M = 8$.

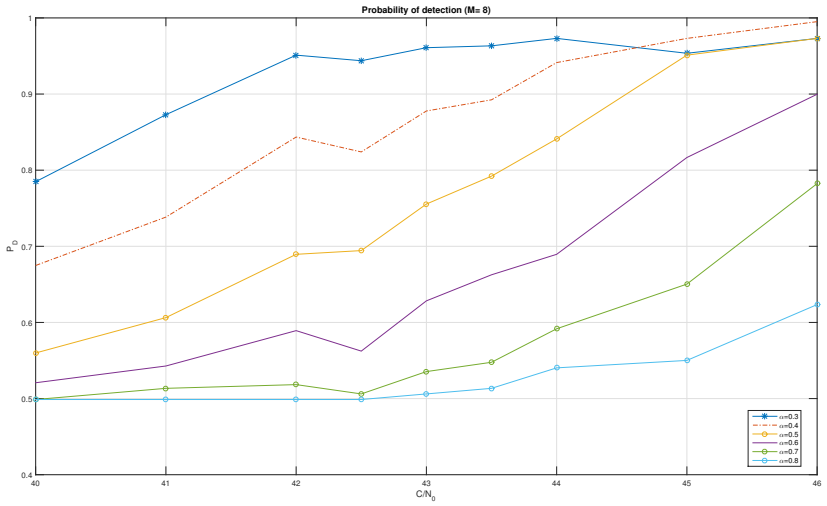

Fig. 3.35 Results for P_d with $M = 8$.

complexity by decreasing M. Obviously, α depends from distortion and could give additional information about it.

3.4 Constrained Least Squares

This section presents an enhanced method of the algorithm proposed in Section 3.3.2, where a novel approach of the MPDD algorithm to detect MP or other distortions at the correlation stage level is presented. The method is based on the decomposition of the signal by means of LAFs [43, 51]. The enhancement presented in this section includes some constraints on the solution, in order to limit the effects of the noise and improving the performance in terms of detection and false alarm probability even in low Signal-to-Noise Ratio (SNR) conditions. It is also presented the adaptation of the algorithm to Galileo correlation signal, so extending the possibility to use not only with the GPS but also with other satellite constellations.

The idea is to estimate the received signal as a weighted sum of delayed replicas of the LOS signal by solving, instead of LS, a CLS, a different minimization problem. Then, getting the new vector $\hat{\mathbf{w}} \in \mathbb{R}^{M\times 1}$ of filter coefficients, the MPDD algorithm is performed.

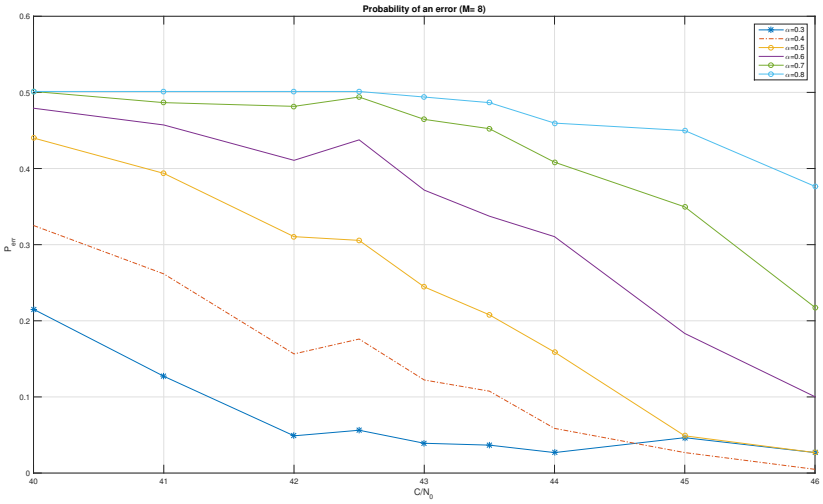

Fig. 3.36 Results for P_e with $M = 10$.

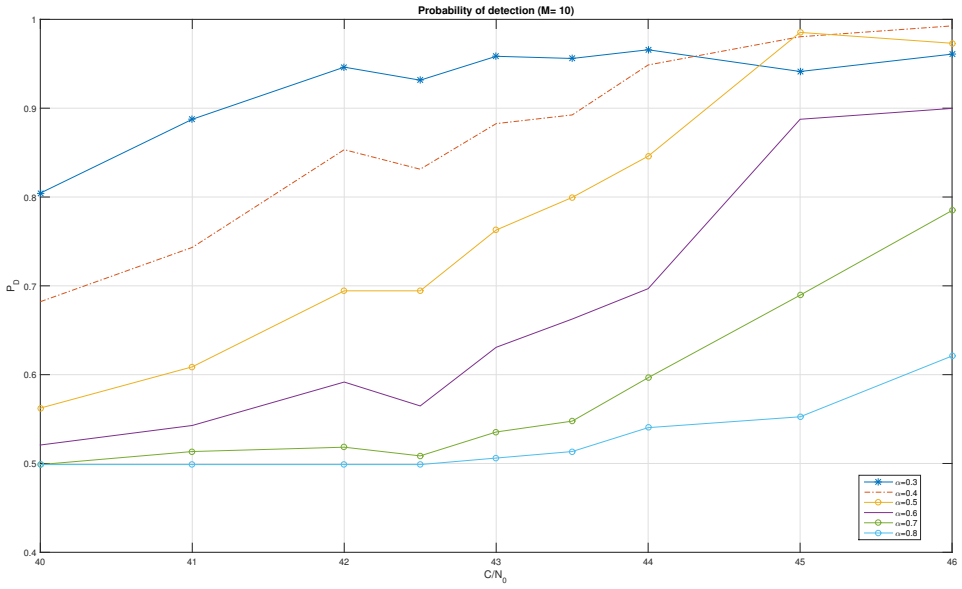

Fig. 3.37 Results for P_d with $M = 10$.

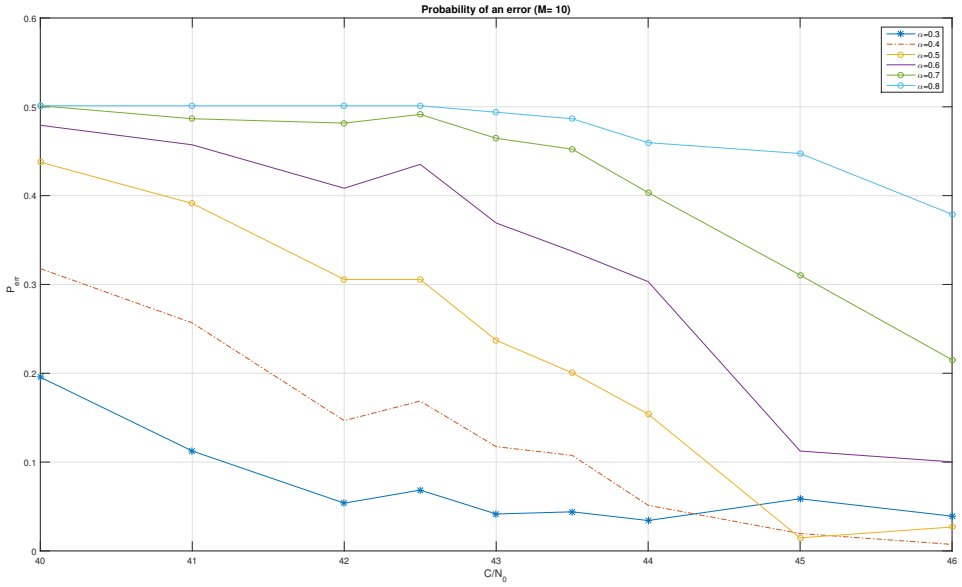

Fig. 3.38 Results for P_e with $M = 10$.

In the MPDD, the estimated vector $\hat{\mathbf{w}} \in \mathbb{R}^{M\times 1}$ is used in a M-dimensional geometrical space to compute its geometrical distance from sample vectors, representing possible MP scenarios.

In Section 3.1, the LS goal is the minimization of the error ϵ defined by (3.3). The method could not be very robust in the presence of noise. Then, in order to improve the method, in particular reducing the false alarm probability mainly due to the noise, an updated version has been developed and is presented here. The w_i coefficient vector is estimated by solving a CLS problem, which in formulas is defined as:

$$\begin{aligned} &\min && ||\mathbf{U}\mathbf{w} - \mathbf{d}||^2 \\ &\text{subject to} && w_i > 0,\ i = 1, \ldots, M. \end{aligned}$$

where $\mathbf{U}, \mathbf{w}$ and $\mathbf{d}$ are the previous matrix and vectors as described in Section 3.1. The Non-Negative Least Squares, as in [54], is applied here. As discussed in 3.1, in the presence of noise the traditional LS estimates the input including the input noise. The input signal is estimated as a weighted sum of delayed replicas of the target signal, which is a suitable model for the MP channel but does not fit well for the WGN channel. As a consequence, the system adds a

high number of positive and negative w_i coefficients in order to try and estimate the WGN component as well as it can. The result is a highly noisy solution.

A constraint is then put here on the possible values of the w_i coefficients. The method presented here, applying the CLS, includes a bound on the solution in order to have all the M coefficients w_i of the $\mathbf{w}$ vector such that $w_i > 0$, $\forall i$.

However, it is clear that this constraint appears not to be suitable to estimate a MP channel where LOS and MP components have different phase signs. In such a case, in order to properly estimate the signal components some negative w_i coefficients would be needed. Nevertheless, it has to be noted that the goal of the algorithm is not to properly estimate the signal as weighted sum of components, but just to detect if anomalies are present in the signal, discriminating between the only-LOS case and all the other unwanted cases. If a counter-phase component is present, then the CLS (applied with the *autocorrelation method* windowing as explained in Section 3.1.1), estimates non-null w_i coefficients with shorter delay with respect to the LOS. Such an anomalous behaviour detects the presence of counter-phase MP, and a warning flag is raised. Furthermore, CLS has also an impact on the decision metric because thanks to the constraint, we can avoid to compute distances with vectors with $\alpha < 0$. In the ideal case of only-LOS signal present without noise, the LS and the CLS solutions are coincident. However, in general the CLS algorithm gives a smaller number of non-null w_i coefficients than the LS, and the global noise effect decreases.

3.5 Results

The new version of the MPDD algorithm has been tested and validated by means of a simulation campaign with simulated GNSS data generated by N-Fuels [52], which can generate signals affected by multiple different MP rays. The main problem is the presence of the noise, so in Section 3.3.3, to reduce the noise and also the computational load, the correlations computed are collected in a time window and averaged. In all the considered simulations, the time window chosen is $T_a = 200$ ms. In this case, with a $T_{int} = 1$ ms, we have 200 correlations which are averaged within a single time window. Moreover, we assume that if a strong MP is present (strong enough to affect the position

solution) its delay is supposed to be constant over several measurement epochs. For both LS and CLS solutions the length of the filter is $M = 9$. Another parameter to take into account for the detection is the set of vectors used in the decision metric. In the simulations both the LS and the CLS method have the same set of vectors with $\alpha = 0.3$ and $\alpha = 0.5$. In the following simulations, we test the detector on different scenarios with some common parameters. We generate only 1 reflected ray of MP and its power is $P_{MP}(t) = \frac{P_{LOS}(t)}{2}$ where $P_{LOS}(t)$ is the power of the LOS signal and it is present in the interval $[15-20]$ s. We perform the test with different values of C/N_0 and DLL spacing d_s. In the scenario in Fig. 3.39, the MP is in counter-phase. The MPDD output with CLS solution shows that some MP is present and a distortion is correctly detected. It is possible to observe the effects of the MP even in the estimated C/N_0. In general, the correlators of the DLL influence the algorithms devoted to the estimation of C/N_0.

Furthermore, the detection method was adapted to Galileo E1 OS signal by changing the ideal correlations in matrix $\mathbf{U}$. An example in Fig. 3.41 where the correlation in the presence and absence of MP is displayed. In Fig. 3.39 some MPDD results related to Galileo are shown.

Then, in Fig. 3.40 a comparison between the LS and the CLS coefficients is shown: the $\mathbf{w}$ vector estimated in the two cases is plotted, in the only-LOS case with $C/N_0 = 40$ dBHz. It can be noted that the CLS solution provides a lower number of non-null w_i coefficients, and the absolute value of those coefficients is in general lower, with respect to the LS solution. This is an aspect of the CLS method, able to reduce the noise impact on the coefficients.

The results of the simulation scenario with $C/N_0 = 39$ dBHz with in-phase MP and different values of d_s are shown in Fig. 3.42 and Fig. 3.43. Figure 3.42 is obtained with a spacing of $d_s = 0.5$ and it means that the tracking loops are more affected by MP and noise distortions than tracking loops with a narrower spacing as in Fig. 3.43 where $d_s = 0.2$. In fact, the effect of d_s is also visible in the performance of both implementations of the MPDD with LS and CLS. Again, it is possible to see the effects of the MP even in the estimated C/N_0: in the considered cases, the effect of the MP on the C/N_0 is not, as it could be imagined, to decrease the signal power; on the contrary, the MP presence increases the C/N_0. However, this kind of situation does not

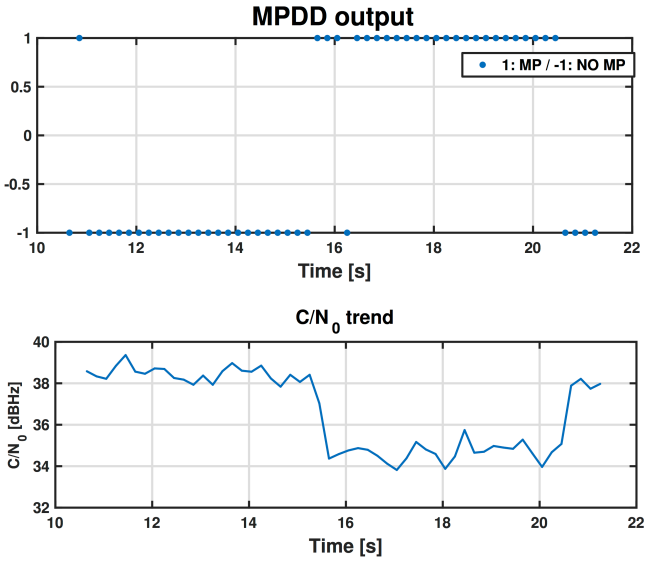

Fig. 3.39 MPDD results with Galileo signals with an output every $T_a = 200$ ms.

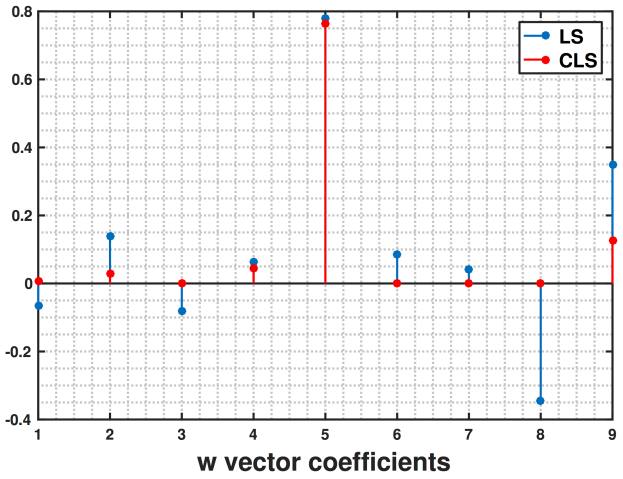

Fig. 3.40 Example of vector coefficients in case of LS and CLS solution without MP and $C/N_0 = 40$ dBHz.

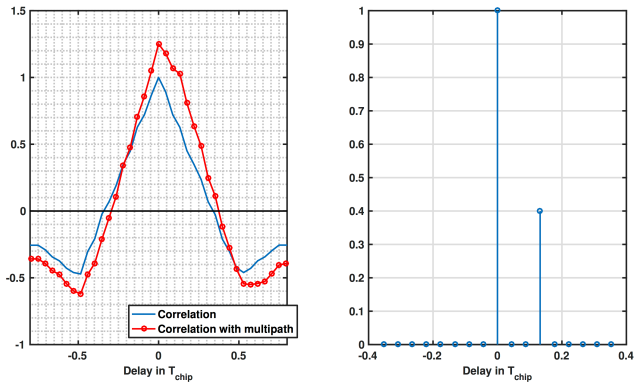

Fig. 3.41 Galileo correlations (left plot) and values of the taps of the linear filter (right plot).

mean that the quality of the signal is improved overall, simply it is the effect of the small difference between MP and LOS phase. The LOS signal is distorted and affected by a MP error. The delay estimate provided by the DLL is not properly correct.

In Fig. 3.44 the evolution in time of the energy of the residual error ϵ is shown (the cost function in (3.3) of the minimization problem), in both the LS (ϵ_{LS}) and in the CLS case (ϵ_{CLS}). The graph is normalized by the maximum value of ϵ_{CLS}. As we expect, the LS solution has a lower value of residual error, which means that the LS problem has better performance in terms of approximation of the input signal, since the LS solution has not constraints. On the contrary, the CLS approach provides a worse solution in terms of approximation of the input signal, with respect to the LS method. Therefore in general $\epsilon_{LS} < \epsilon_{CLS}$. On the other side, when only the noise is present, it is possible to observe that the difference $\epsilon_{CLS} - \epsilon_{LS}$ is not so remarkable as in case of MP presence, so the performance is quite similar and the difference is given by the presence of the constraint and the noise. As mentioned in Section 3.4, for our detection purpose, a huge difference between the only-noise condition and MP condition is desirable, since it allows to have less ambiguous results to discriminate between the presence/absence of signal distortions (MP) even in the presence of low SNR.

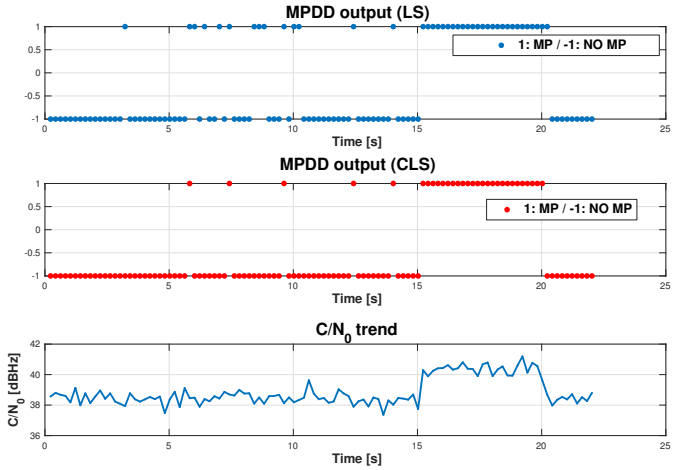

Fig. 3.42 MPDD comparisons between LS (upper graph) and CLS (middle graph) method, spacing of the DLL $d_s = 0.5$ with GPS L1 C/A signals with an output every $T_a = 200$ ms and C/N_0 trend (bottom graph).

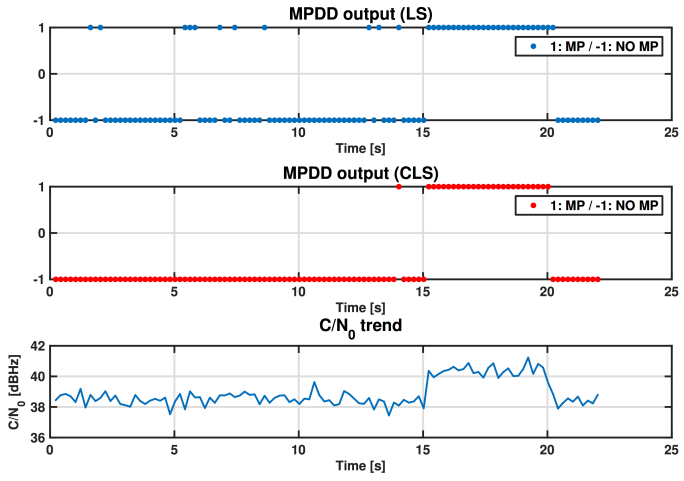

Fig. 3.43 MPDD comparisons between LS (upper graph) and CLS (middle graph) method, spacing of the DLL $d_s = 0.2$ with GPS L1 C/A signals with an output every $T_a = 200$ ms and C/N_0 trend (bottom graph).

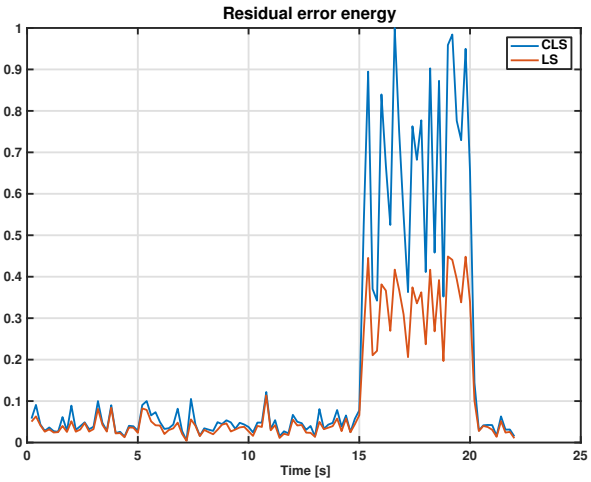

Fig. 3.44 Energy of the residual error ϵ. Results for both LS and CLS method. Spacing of the DLL $d_s = 0.2$ with an output every $T_a = 200$ ms.

3.5.1 LS and CLS comparison

To compare the performance in terms of P_d and P_{fa} of the detectors, we used the same dataset used in **??**. The results are illustrated in Fig. 3.45 and Fig. 3.46 for different value of α. In Fig. 3.45 the results are related to LAF-LS, while Fig. 3.46 to LAF-CLS solution. It is possible to observe that the two detectors, in terms of P_d, have similar performance, instead, the situation is different in terms of P_{fa}. As we already mentioned, the reason why we choose a constraint is because the noise at the input of the LAF-LS generates possible false alarm, especially in case of low C/N_0.

By using these plots, it is even possible to select values for α to tune the entries of the dictionary for the detector.

3.6 Statistical plots for the coefficients: Q-Q plot and mountain plot

Here, we present two graphical tools used in the work. The first, the mountain plot, also called folded empirical Cumulative Density Function (CDF) plot, presented in [55], is a graphical tool alternative to the CDF. The CDF is a strictly increasing function, the mountain plot, instead, folds the second half

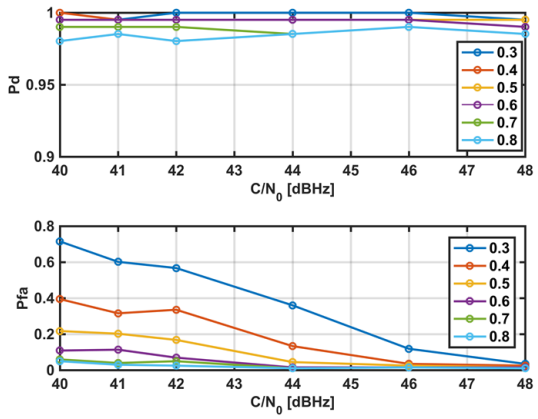

Fig. 3.45 P_d (upper graph) and P_{fa} (bottom graph) for different value of α in case of LS decomposition.

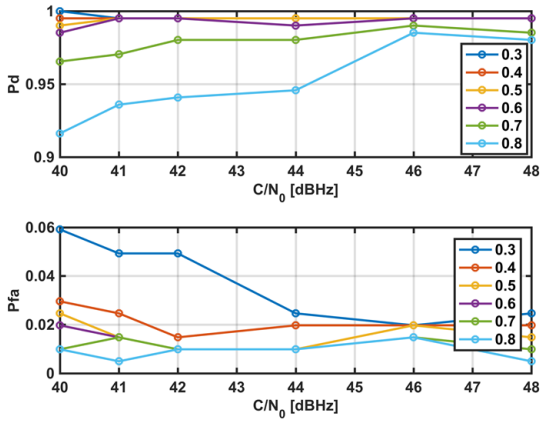

Fig. 3.46 P_d (upper graph) and P_{fa} (bottom graph) for different value of α in case of CLS decomposition.

of CDF. Therefore the resulting plot is identical to the CDF for the elements X with probability $P(X < x) \leq 0.5$ while, it is plotted $1 - P(X \leq x)$ for the elements X with probability $P(X > x) > 0.5$. This instrument is quite useful to highlight some properties, such as symmetry, and to emphasize the median of the distribution [56]. It is also useful and easier to find the central amount of percentage (i.e 95%) of the data. Finally, different distributions can be compared more easily.

Another graphical tool used is the Q-Q plot (stands for Quantile-Quantile plot) to compare two probability distributions by using quantiles against each other. If the two distributions are similar, the Q-Q plot will be a line $y = x$. In our case Q-Q plot is used to compare an empirical distribution against a Normal distribution.

To populate the dictionary used for the detection, we can start by evaluating the distribution of the coefficients in case of LAF with LS and CLS solution. First of all, we started with a simulation scenario with only noise with a duration of 30 minutes and a moving average window of 500 ms. The case of LAF-LS is in Fig. 3.47, where it is possible to see a good symmetry for all the $M = 9$ distributions. It is plotted also a Gaussian distribution (the circle marker) that overbound the 5-th coefficient, the center one. As already explained in the chapter, it is the coefficient representing the LOS in the ideal case. Its distribution is centered around a value different from zero. The other distributions, in case of only noise, are centered around zero. Instead, others distributions of the coefficients are centered around zero and have different variances. It is still possible to overbound with a zero mean Gaussian distribution and a standard deviation larger ($\sigma = 0.5$) than the center coefficient distribution ($\sigma = 0.2$). Another observation regards the distribution of the 4-th and 6-th coefficient. As in the case of the 5-th coefficient, they have a bias, since they are not centered around zero. This depends on the decomposition mechanism of filter together with the position of the peak leading to a not perfect symmetry of the measured correlation. This is more visible in case of LAF-CLS solution as in Fig. 3.48. The Q-Q plot in Fig. 3.49 is an example, for the distributions centered around zero, of the similarity with a Normal distribution in a limited range.

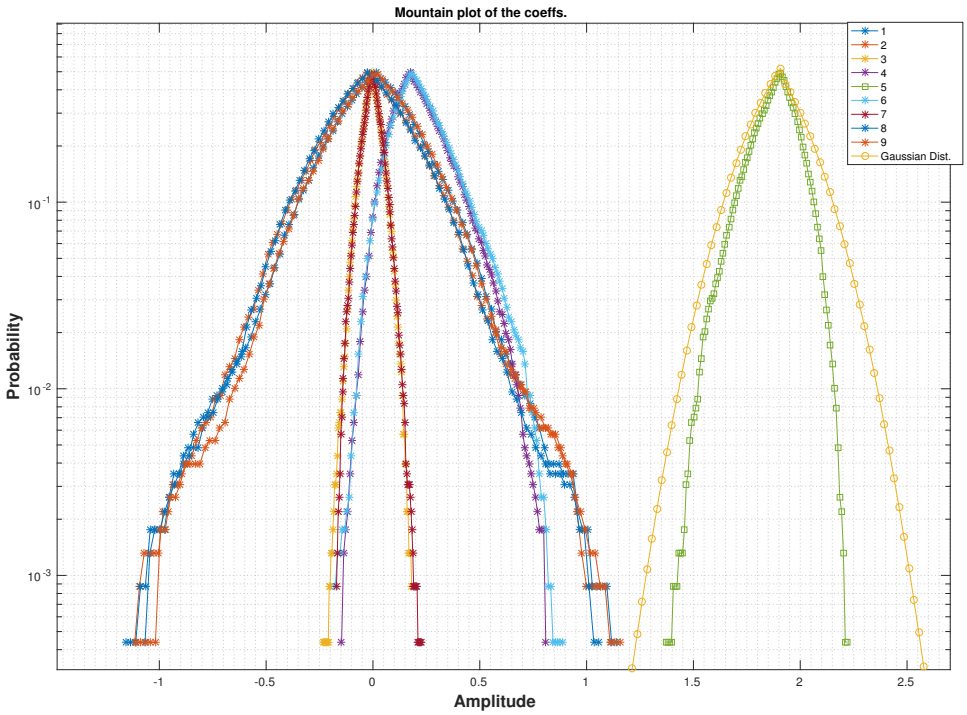

Fig. 3.47 Distribution of all M coefficients of the filter in case of LAF-LS solution with $C/N_0 = 45$ dBHz.

In Fig. 3.48 a mountain plots in the case of LAF-CLS is shown. Here it is possible to observe the huge separation between the zero-centered distributions and the LOS distribution. This depends on the fact that in the same noise condition, the variances of the non-LOS components is smaller than in the LAF-LS case.

3.6.1 Analogy with Transmission Theory

As already said, the analysis over the incoming signals were performed at the tracking stage of the GNSS receiver. The correlation signal obtained was decomposed by solving a LS or CLS minimization problem. The decomposition works not directly on the signal, but on the shape of the correlation. All the considerations about the detector are based on the vector of the filter coefficients in a vector space domain. The decision metric chosen is the minimum euclidean distance between vectors in a geometrical space. By using a multicorrelator and

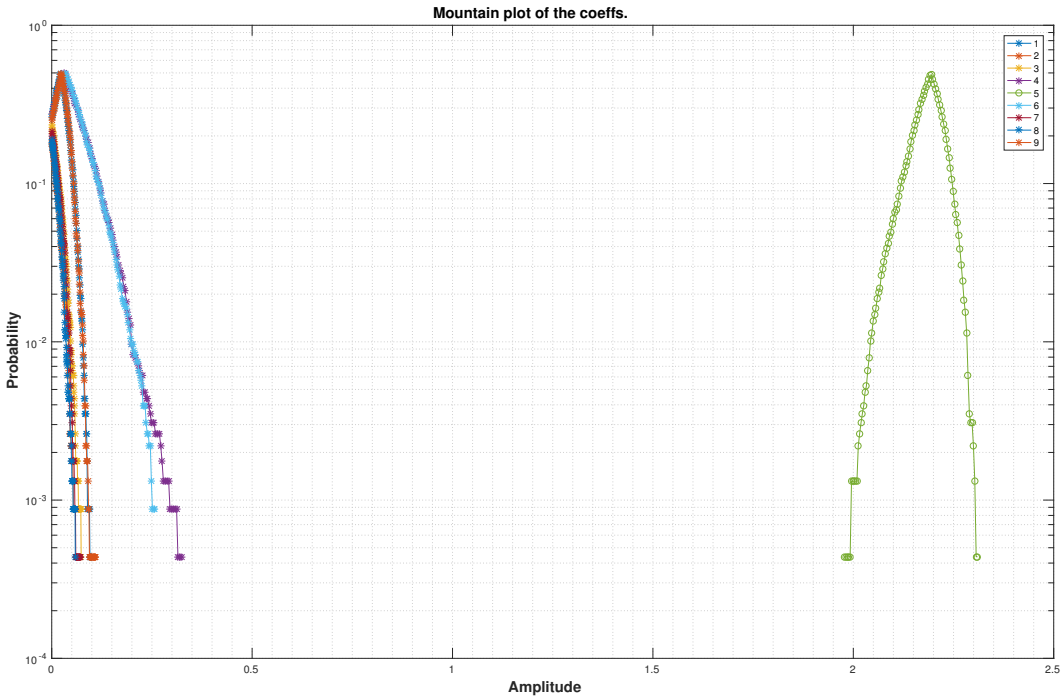

Fig. 3.48 Distribution of all M coefficients of the filter in case of LAF-CLS solution with $C/N_0 = 45$ dBHz.

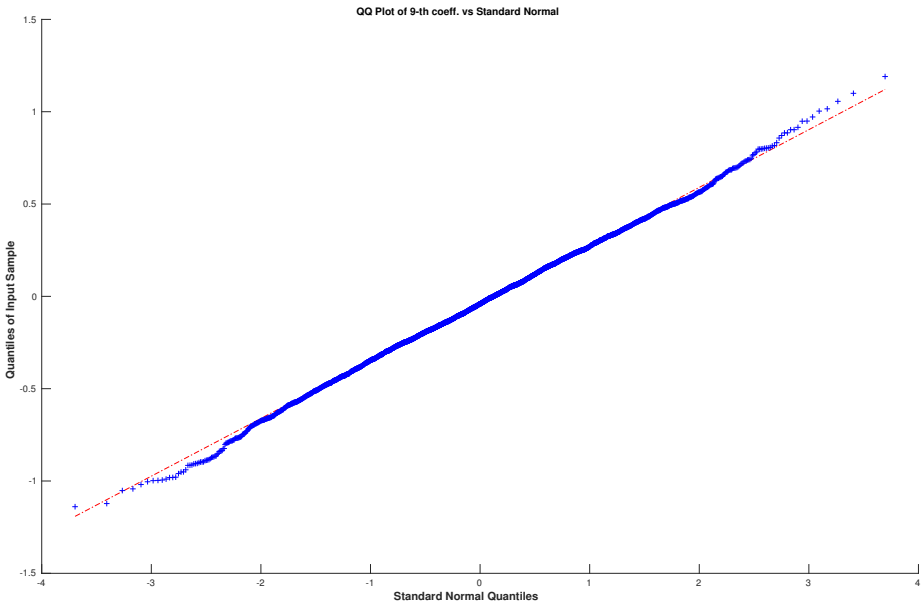

Fig. 3.49 Q-Q plot of the 9-th coefficient in case of LAF-LS solution with $C/N_0 = 45$ dBHz.

the decomposition, we could have more information about the MP, so the reason why we chose to use a dictionary of vectors for comparisons. This approach leads to an analogy with another communications topic: the transmission theory [57]. By transforming the problem from signal to geometrical domain, we have similar conditions as in case of reception of a symbol, on an AWGN channel, and try to guess which symbol of the constellation we received.

In transmission theory, in case of the classical modulation scheme like BPSK, Pulse Amplitude Modulation (PAM), Quadrature Amplitude Modulation (QAM) etc., we have a set $(s_1, s_2, \ldots, s_i, \ldots, s_n)$, called constellation, of the possible symbol that can be received. The constellation can be represented, for example, in a plane and the symbols are points distributed in that space. The received symbol s_r, due to the noise or other impairments, is a point in the space that probably has coordinates not coincident with the coordinates of the constellation symbols. To decide which symbol was transmitted, the space is divided in regions, called Voronoi regions, around the symbols of the constellation. The decision taken is that the incoming symbol s_r is a symbol of the constellation $(s_1, s_2, \ldots, s_i, \ldots, s_n)$ if it is within one of these regions.

The Voronoi region associated to a symbol s_i is the set of all vectors which are nearest to a s_i than to all the others. To assess in which region the symbol belongs, the distance between the symbols'coordinates is calculated. The decision is taken choosing the symbol at the minimum distance.

In our problem, we have a similar situation where the "transmitted symbol" is the vector of filter coefficients and the "constellation" is the dictionary. Then, our decision metric is the minimum distance as in the transmission theory case. In our constellation, the number of symbols is proportional to the number of its dimensions and it is higher than the contellations used for the modulation purpose.

3.7 Conclusion

In this chapter, we presented the LAF theory and how this theory can be used to detect correlation distortions.The strategy is based on the representation of the measured correlation as the output of a FIR filter, then the coefficients of the filter are observed and compared with a dictionary of vectors.

From this initial approach, the method is evolved, the **U** matrix has been extended in order to have a better representation of the signal in input by using components both on the left and on the right side of the correlation peak. Then, the method has been enhanced by modifying the minimization method, changing from a LS to a CLS problem. Thanks to the CLS algorithm the noise impact is highly reduced (especially with low C/N_0), resulting in a reduction of the false alarms.

Moreover the MPDD algorithm, which was initially developed and tested on the GPS L1 C/A signals, has been modified in order to be applied to the Galileo signals.

Simulation results showed that the new enhanced algorithm, based on the CLS solution, has better performance in terms of false alarm probability even in the presence of low SNR. The results are proved also with the Galileo signals.

Chapter 4

Signal Quality Index

This chapter is related to the work presented in [58]. A well assessed integrity technique is the so-called RAIM [59], which can be implemented by adopting different algorithms, such as range comparison [35], Pseudorange residual or Residual Based (RB) [36], and parity method [37]. They provide snapshot schemes and yield identical results under the assumption of equal alarm rate, as shown in [38], where a detailed comparison of these methods is given. Another well known RAIM scheme is the Solution Separation that works on the position domain [60]. A basic assumption of all these schemes is that only one fault at a time is possible. However, these schemes can be extended to the case of multiple faults, as described in the recent work [61].

The RAIM algorithms use PR and position data to implement the FDE module, which leads to the exclusion of faulty satellites in the position computation. However the identification of faulty satellites can be done also at the tracking stage of the receiver, by adopting adequate signal processing techniques, as shown, for example, in [62]. Today, these methods cannot be implemented in a current commercial GNSS receiver, but a new generation of receivers can be devised with new blocks working in the correlation domain, and able to assist the FDE module of RAIM.

The work presented in this chapter analyses the feasibility of this concept of assisted-RAIM. In particular it is focused on the effects of environmental impairments, as MP, and how to assist RAIM to protect the receiver from this type of errors. MP occurs in the presence of objects, close to the receiver,

which can reflect the signals coming from the satellites. The working principle of a GNSS receiver is based on the measurements of the delay between the time instant when a signal leaves the satellite and the time instant when the signal is received. Therefore, if reflected signals are received together with the useful signals, an error on the estimation of the delay of the GNSS signals may occur. The DLL is the block devoted to the delay estimation. However a DLL error not always impairs the PR measurements. This fact has to be taken into account in the design of assistance methods based on correlation points estimated by a DLL. More details on this aspect are given in Section 4.2.

In the literature, many MP mitigation techniques are proposed (e.g., [46, 47], just to cite a couple of examples). However, when the goal is to satisfy some integrity requirements, the general approach is to identify the presence of errors in the delay estimation without mitigating its effect, but rather excluding the satellite affected by impairments from the solution. We propose here to adopt a technique of MP detection, which derives from the MPDD described in Chapter 3, and based on the identification of a LAF able to model the MP effects, as shown in [48, 49]. This chapter introduces the concept of SQI, which is both a metric able to evaluate the goodness of the signal, and a parameter used to improve the performance of the FDE module of RAIM. Note that methods of Signal Quality Monitoring (SQM) are already proposed in literature in the framework of integrity systems. For example in [63, 64] SQM algorithms are proposed to detect anomalous signal distortions by using extra correlators, which are not used to maintain the receiver locked to the incoming signal. The difference here is that the information from the tracking stage is used to create an index (SQI), which becomes an integral part of the assisted RAIM.

The chapter gives a brief introduction of the DLL and how it works in Section 4.1. In Section 4.2 the methods of pseudorange calculation are reviewed and the MP impact on DLL outputs and PR measurements is analysed. The Section 4.3 introduces the concept of the heuristic metric SQI. In Section 4.4 some RAIM and FDE concepts are given and the RB RAIM algorithm is briefly explained. In Section 4.5 a possible interaction between SQI and RAIM is described and simulation results are given.

4.1 DLL

The main purposes of the DLL is to maintain a local code $C_{loc,m}[n]$ of the receiver locked to the incoming PRN code $C_m[n]$ where m is the SV index. To do this, DLL estimates the relative delay between two codes by using a correlation operation. However, the typical implementation of the DLL is not based on the estimation of a delay, rather, on the estimation of a code frequency f_c. To maintain locked $C_{loc,m}[n]$ and $C_m[n]$, every integration time T_{int} (i.e., 1 ms), the output of the DLL's discriminator is used to correct f_c and this mechanism yields to have a variable number of samples every T_{int}. The presence of filters in the loop introduces a delay in the receiver chain or better, a transient with a duration dependent on the filter bandwidth: narrow band means less noise but long transient and vice versa. To align the incoming PRN code with a locally generated code, a DLL must include integrators, a code loop discriminator, and code loop filters. In our scheme the signal Equation (1.8) is first demodulated by multiplying it by two local carrier waves at frequency f_{IF}, one for each branch of the receiver (I and Q). The resulting signal is multiplied by three local codes (called early, prompt, late), generally shifted by $-1/2$, 0 and $+1/2$ chip time, and the outputs are integrated and dumped to implement the correlator.

The model chosen in this work for the discrimination function is a *non-coherent* scheme, independent of the phase of the local carrier, and with the expression

$$\frac{(I_e^2+Q_e^2)-(I_l^2+Q_l^2)}{(I_e^2+Q_e^2)+(I_l^2+Q_l^2)}$$

called Normalised Early minus Late power, where $I_e = AR_x(\tau - d/2)\cos(\phi_e)$, $Q_e = -AR_x(\tau - d/2)\sin(\phi_e)$, $I_l = AR_x(\tau + d/2)\cos(\phi_e)$, $Q_l = -AR_x(\tau + d/2)\sin(\phi_e)$, and $R_x(\cdot)$ is the correlation function between the local and incoming code, A is an amplitude factor, τ is the code delay of the signal, ϕ_e is the estimated carrier phase error and d is the correlator spacing between early and late.

We are interested in investigating what happens to the DLL parameters, when a disturbance, e.g., an MP, affects the received signal. The tracking loops settings used for the results are the following:

- the DLL noise bandwidth is $B_n = 2$ Hz

- the correlator spacing $d = 0.5$ chips
- the PLL noise bandwidth is $L_n = 10$ Hz

4.2 Pseudorange Calculation in a GNSS Receiver

From the theory, we know that a typical GNSS receiver computes the user's position from the estimated pseudorange ρ_i (distance between the i-th satellite and the receiver). Considering that both satellites and receiver's clocks are affected by independent errors, we call *system time* the reference time frame where satellites and the receiver's clocks are referred. Before introducing the equation, we define some notations [3]:

- T_t is the system time at which the signal left the satellite
- T_{RX} is the system time at which the signal reached the user receiver
- δt is the offset of the satellite clock from system time (written in the navigation message)
- t_{RX} is the offset of the receiver clock from system time
- $T_t + \delta t$ is the satellite clock reading at the time that the signal left the satellite
- $T_{RX} + t_{RX}$ is the user receiver clock reading at the time the signal reached the user receiver
- c is the speed of light

A generic ρ for a single satellite is given by taking into account all the clock errors

$$\begin{aligned} \rho &= c\,(T_{RX} + t_{RX}) - c\,(T_t + \delta t) \\ &= c\,(T_{RX} - T_t) + c\,(t_{RX} - \delta t) \\ &= r + c\,(t_{RX} - \delta t) \end{aligned} \tag{4.1}$$

where r is the geometric range and the second term $c(t_{RX} - \delta t)$ is the residual distance due to the not perfect synchronisation between satellite and receiver clocks. To calculate this, the time of flight of the signals is measured and the clock corrections will be made after data demodulation and PVT computation.

4.2.1 How the GNSS Receiver Implements the pseudo-range Computation

In order to process tracked signals independently, GNSS receivers assign each one a dedicated channel. As said, to obtain ρ it is necessary to know the transmitted time T_t for each satellite and to correct all the misalignments of the receiver and the satellite clock with respect to the system time. Two possible implementations of this measurement are Common transmission time and Common reception time [65, 66]. The former one is based on the satellites' transmission time. Obviously the channels are not synchronised each other at the receiver side, so on each channel the same bit of a subframe (and relative TOA) have to be identified. The receiver selects a reference channel by using the first arriving bit, and calculates the relative delay Δ_i with respect to the bit of i-th satellite, $\Delta_i = T_{RX,i} - T_{RX,1}$. This allows to write the range r_i of the i-th satellite as $r_i = \rho_1 + c\delta t_i + c\Delta b + c\Delta_i$, where ρ_1 is the pseudorange of the reference channel or in other words, the satellite closest to the user, Δb is the unknown bias for the not perfect synchronisation between clock on board the i-th satellite and the clock of the receiver. Finally, δt_i is the correction of the offset of the i-th satellite clock from system time.

In the second implementation (Common reception time) the receiver calculates $\Delta_i = T_u - T_{RX,i}$, where, in this case, Δ_i is the time interval between the instant of reception of the subframe for the i-th channel $T_{RX,i}$ and T_u, that is the common receiving time when the receiver decides to measure the PR over all channels. All the pseudoranges are derived with respect to the reference channel, which is the one with the minimum travel time. Once Δ_i are computed for all the channels, $r_i = \rho_1 + c\Delta b + c(\Delta_1 - \Delta_i) + \delta t_i$.

To measure the time interval Δ_i, the receiver continuously counts the samples processed per each channel and maintains a monotone counter in 20 ms increments derived from receiver's reference oscillator [3]. The mechanism

of counting partially protects the pseudorange measurements from correlation distortions. In next section this is proved by simulation since a theoretical explanation would require a deep analysis of both DLL and counting operations.

The Common reception time is the method usually employed in commercial GNSS receivers.

4.2.2 Simulation Experiments

In this section we investigate which is the effect of the correlation distortions on the pseudorange measurements. In fact it is known that the PRs are measured in scheduled time epochs with a typical rate of 1 Hz (or few Hz), while a DLL computes correlations with a much greater rate (e.g., 50 Hz). Therefore, we expect that a distortion in the correlation may have a different impact if it occurs during the local code update performed by the DLL, or at the epochs of pseudorange measurements. To analyse these different effects we have performed some simulation tests. The simulation scenarios were created by using the signal generator described in [67]. The analyzed datasets represent a static position with four satellites in view all affected by one-reflected ray of MP. The received signal is GPS L1 C/A, it lasts 60 s with different values of Carrier-to-Noise ratio (C/N_0), but constant for the whole duration.

The dimension of the time windows of the MP events are different, so as to test the impact of the duration on the accuracy reached by the receiver on the PVT stage. The MP model used in the simulation is

$$\begin{aligned} s(t) = {} & A_0 D(t-\tau_0) C(t-\tau_0) \cos(\omega_0 t + \phi_0) \\ & + \sum_{i=1}^{N} A_i D(t\tau_0 - \tau_i) C(t-\tau_0-\tau_i) \cos(\omega_0 t + \phi_0 + \Delta\Phi_i + (\Delta\omega_i - \Delta\omega_0)t) \end{aligned}$$

where A_0 is the signal amplitude of the LOS and A_i is the amplitude of the reflected rays. τ_0 and τ_i are respectevely the delay of the LOS and the delay of the i-th ray. $\omega_0 t + \phi_0$ is the phase of LOS and the phase of the i-th ray is $\omega_0 t + \phi_0 + \Delta\Phi_i + (\Delta\omega_i - \Delta\omega_0)t$. The values of the initial phase and delay of the reflected ray are randomly chosen. All the satellites in view are affected by a simulated single ray MP during the time windows indicated in Table 4.1. The MSR is the parameter used to assign the MP amplitude. It is defined as the

Table 4.1 Time windows when MP is present.

Multipath Instants	Duration (s)
10.900–11.300	0.400
27.900–28.100	0.200
42.350–42.650	0.300
50.750–50.900	0.150
53.475–53.525	0.050

ratio between the power of the MP signal and the power of signal itself. MSR is constant and equal to -6 dB (about half amplitude of the signal) for all the time windows.

4.2.3 Preliminary Results

Since the purpose of the simulation experiments is to compare the effect of MP on the measured pseudorange, two versions of the simulated signal are created:

(a) the signal $s_c(t)$, which represents the clean scenario, containing only noise;

(b) the signal $s_m(t)$ obtained by adding MP to $s_c(t)$ in the time windows given in Table 4.1.

Fig. 4.1 shows the time evolution of the code frequency corrections $\Delta f_c[n] = f_c[n+1] - f_n$ where f_n is the nominal value of the code frequency (1.023 MHz in GPS L1 C/A), and the relative value in time calculated as $\Delta T_{chip}[n] = T_{chip} - 1/f_c[n+1]$ in the DLL. The red line is the average value for the corrections. Let's start by analysing this figure in the time windows specified in Table 4.1. What we want to observe is the behaviour of the pseudorange computation just before and during a MP occurrence. The MP effect is clearly observed in the first time window shown in Fig. 4.2, where a change of the code frequency appears during the disturbed time window. Then after a transient, the estimate of the code frequency returns to be stable. Fig. 4.3 shows similar results in time windows affected by MPs with different durations.

To make some comparisons with simulated data, we calculated pseudorange ρ_{clean} in a scenario with only noise and pseudorange ρ_{MP} in a scenario with noise and MP in the time windows given in Table 4.1. Then, we computed

the difference $\rho_{clean} - \rho_{MP}$ in order to see the impact of tracking errors at pseudorange level. These operations are repeated for different values of the output rate T_ρ of the pseudorange measurements. The persistent distortions could introduce errors on the estimate of f_c and consequently in pseudorange computation based on samples counting (as we explained in Section 4.2.1).

We observe that, if we use short T_ρ, affected by MPs limited in time, the probability that next pseudorange calculated is wrong is higher than if we use longer T_ρ. It is possible to observe this effect in Figs. 4.4–4.6, where on the top left graph there is the difference $\rho_{clean} - \rho_{MP}$, on the top right the evolution of the ρ_{MP} in time, at bottom left the graph shows if the PR is measured in the presence of MP and at bottom right the MP profile. For example there are respectively 3, 2 and 1 pseudoranges measured during MP event in Figs. 4.4–4.6. Errors in code frequency f_c estimation may alternate the pseudorange computation. These errors can be recovered by the DLL if the duration of the distortion is limited in time and, once the disturbance is finished, there is enough time before next pseudorange measurement for the DLL to recover the error.

In Fig. 4.7 a zoom of the Fig. 4.4 is depicted, where the circle points indicate that a MP is present in a time instant of pseudorange computation. As expected the quantity $\rho_{clean} - \rho_{MP}$ is different from zero where circle points are present.

4.3 SQI

The output provided by the detector is a hard detection (Yes/No) about the presence of correlation anomalies. However it could be interesting to introduce a sort of soft decision to better assist the RAIM.

The idea has been to continuously monitor the quality of the received signal during the computation of navigation solution. To achieve this goal we introduced an index SQI(t_n) that describes the quality of the navigation solution, where t_n are the time instants of the PVT computation.

This quality index takes into consideration the MPDD output and other information data such as the C/N_0 and the distance between the weight vector

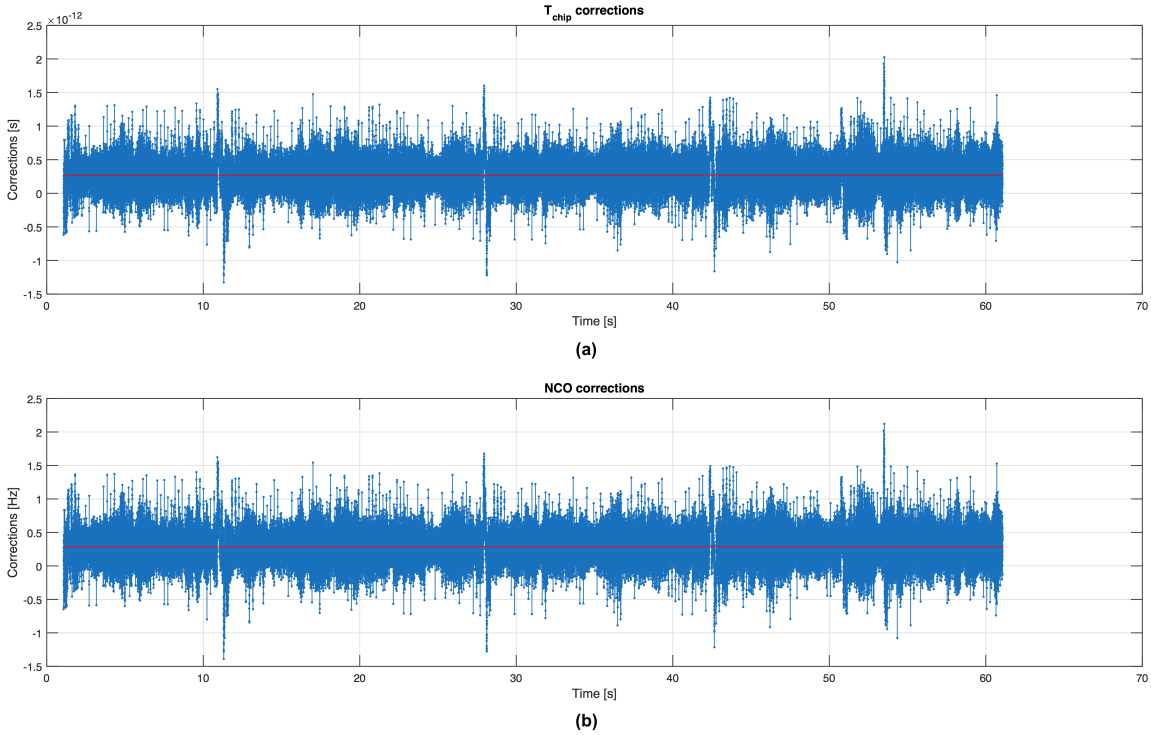

Fig. 4.1 $\Delta T_{chip}[n]$ in time (**a**) and corrections of code frequency $\Delta f_c[n]$ for PRN 31 (**b**).

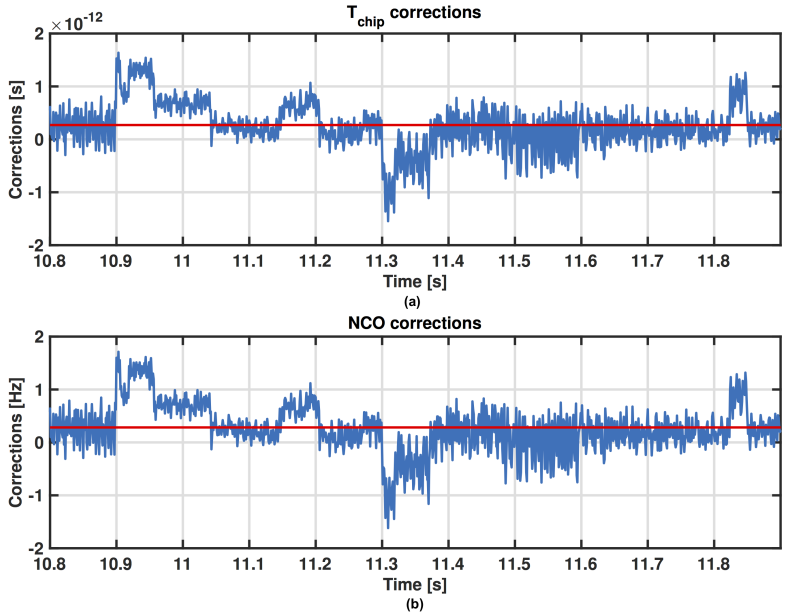

Fig. 4.2 Zoom of the $\Delta T_{chip}[n]$ (**a**) and $\Delta f_c[n]$ (**b**) for PRN 31 in the first time window of Table 4.1.

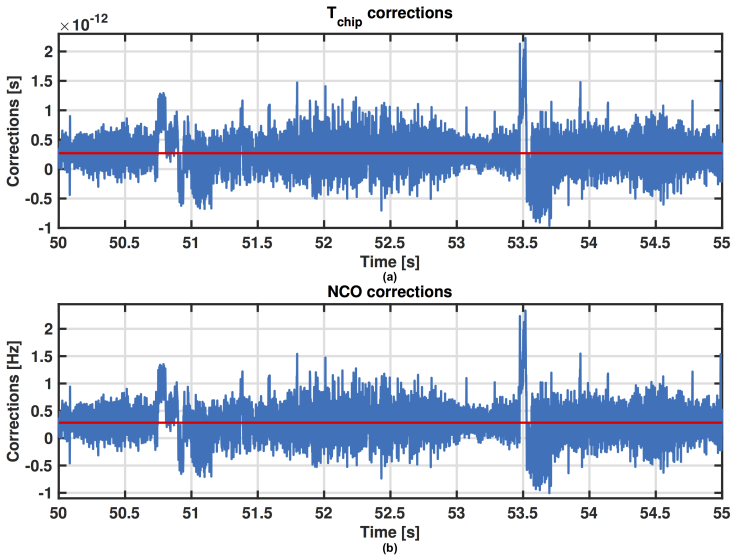

Fig. 4.3 Zoom of the $\Delta T_{chip}[n]$ (**a**) and $\Delta f_c[n]$ (**b**) for PRN 31 in the last time window of Table 4.1.

$\hat{\mathbf{w}}$ and the theoretical LOS vector w_{LOS}. It is defined as

$$\text{SQI}(t_n) = \frac{1}{\lambda}\sum_{k=1}^{N} m(t_{n-1}+kT_a)s(t_{n-1}+kT_a)d(t_{n-1}+kT_a)f\left[\frac{C}{N_0}(t_{n-1}+kT_a)\right]$$

where:

- T_a is the duration of the moving average time window.
- N is the number of the moving average time windows between two time instants (t_n and t_{n-1}). For example, between two PVT computations with a rate of 1 Hz and a moving average of $T_a = 100$ ms, $N = 10$.
- $m(\cdot)$ represents the MPDD output,

$$m(kT_a) = \begin{cases} -1, & \text{if } E_{min} = \min E_p = E_{LOS},\ p = 1,2,...N_V \\ 1, & \text{if } E_{min} = \min E_p \neq E_{LOS},\ p = 1,2,...N_V \end{cases}$$

  meaning that -1 indicates a correlation function with at most noise presence, instead 1 the presence of distortions.
- The function $s(\cdot)$ takes into account the temporal distance between the occurrence of the distorting event and the epoch when the PVT

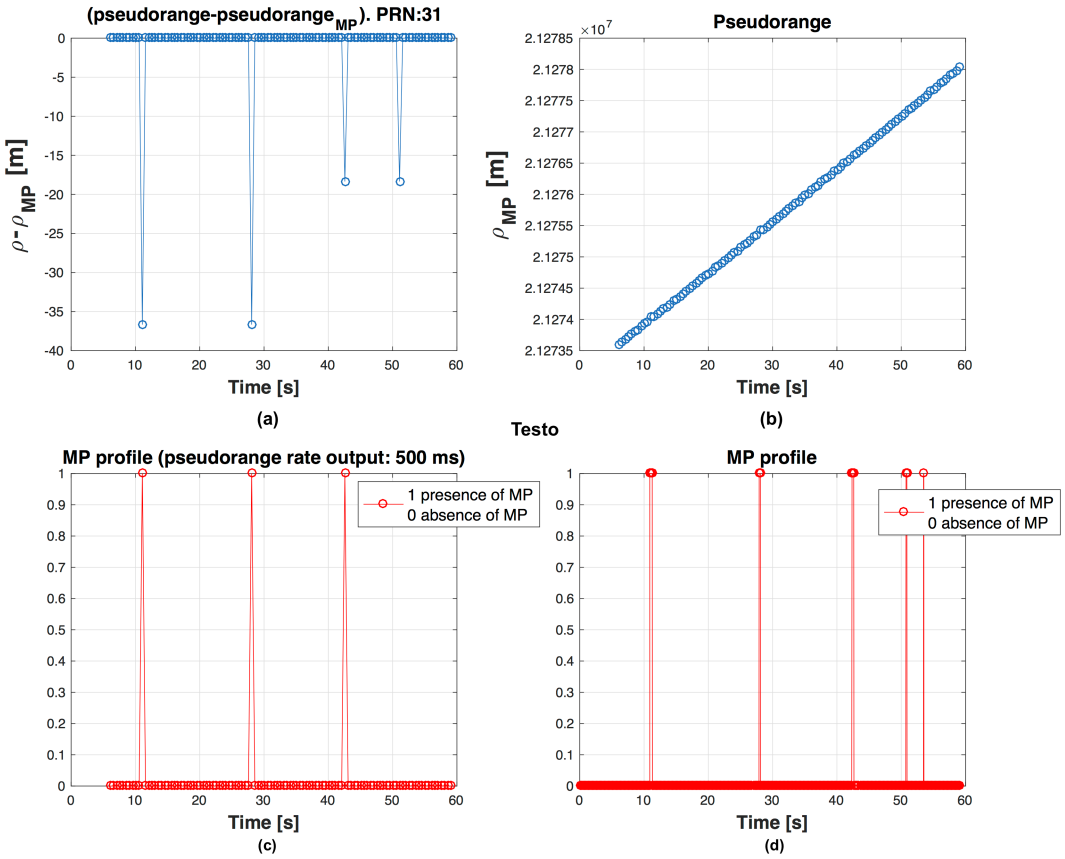

Fig. 4.4 Behaviour of pseudorange for PRN 31, with output every $\Delta T_\rho = 500$ ms. Pseudorange error ($\rho_{clean} - \rho_{MP}$) (**a**); ρ_{MP} trend in time (**b**); MP presence during a pseudorange computation (**c**) and MP profile (**d**) are shown.

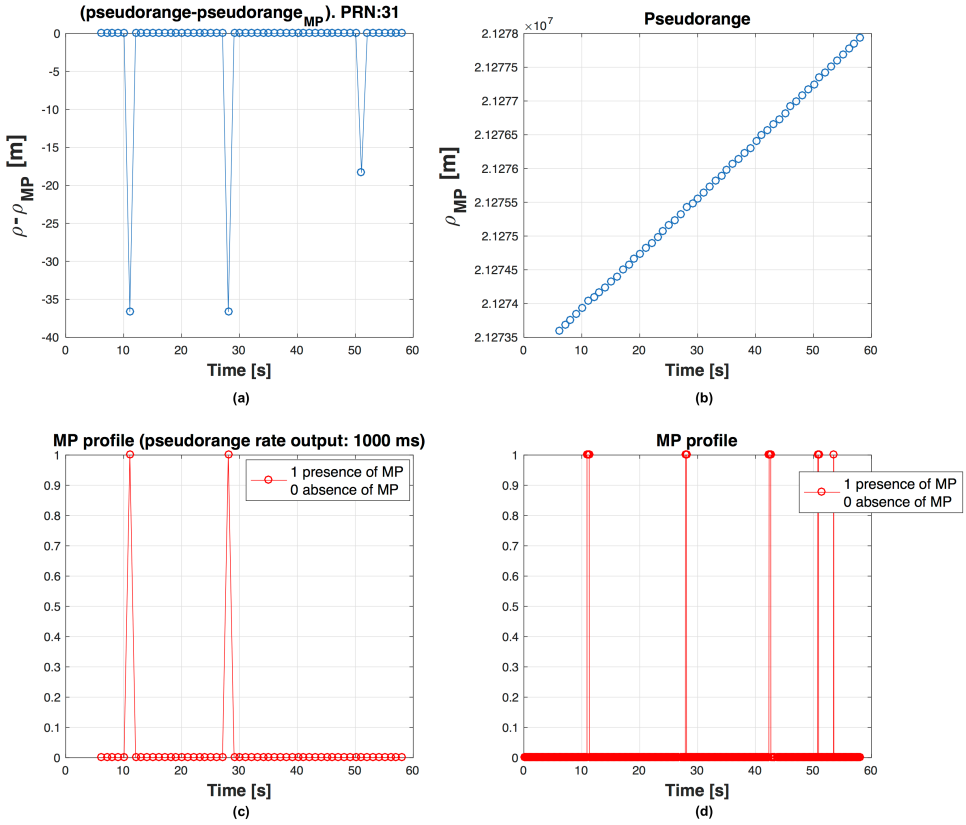

Fig. 4.5 Behaviour of pseudorange for PRN 31, with output every $\Delta T_\rho = 1000$ ms. Pseudorange error ($\rho_{clean} - \rho_{MP}$) (**a**); ρ_{MP} trend in time (**b**); MP presence during a pseudorange computation (**c**) and MP profile (**d**) are shown.

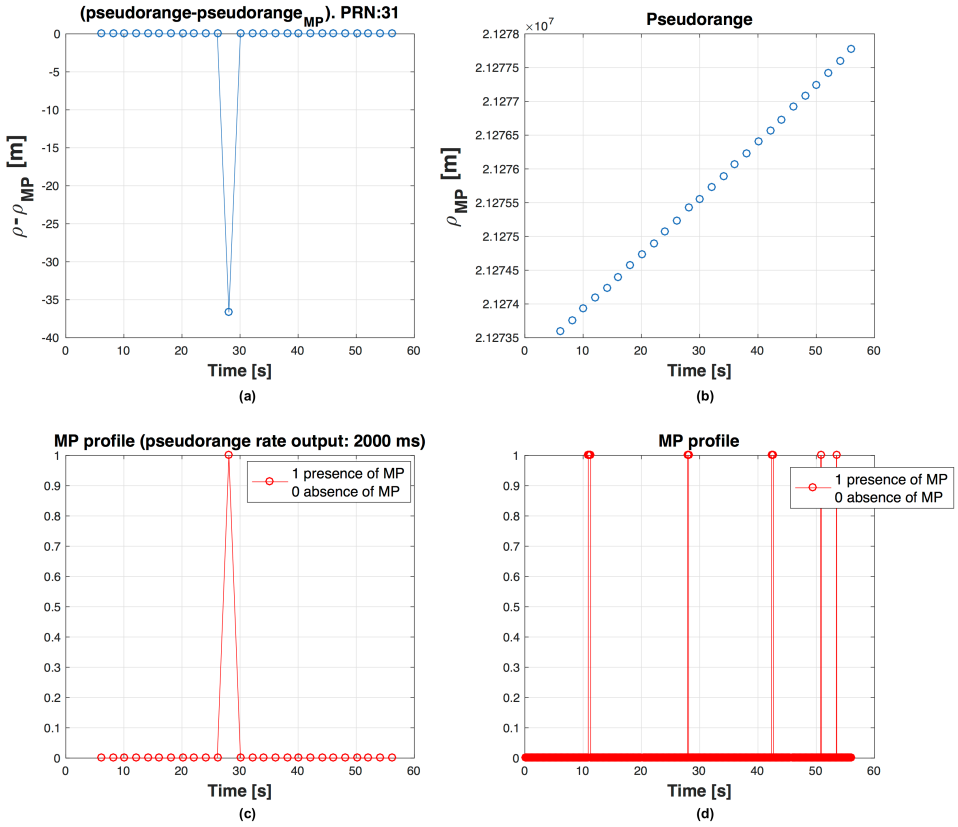

Fig. 4.6 Behaviour of PR for PRN 31, with output every $\Delta T_\rho = 2000$ ms. Pseudorange error $(\rho_{clean} - \rho_{MP})$ (**a**); ρ_{MP} trend in time (**b**); MP presence during a pseudorange computation (**c**) and MP profile (**d**) are shown.

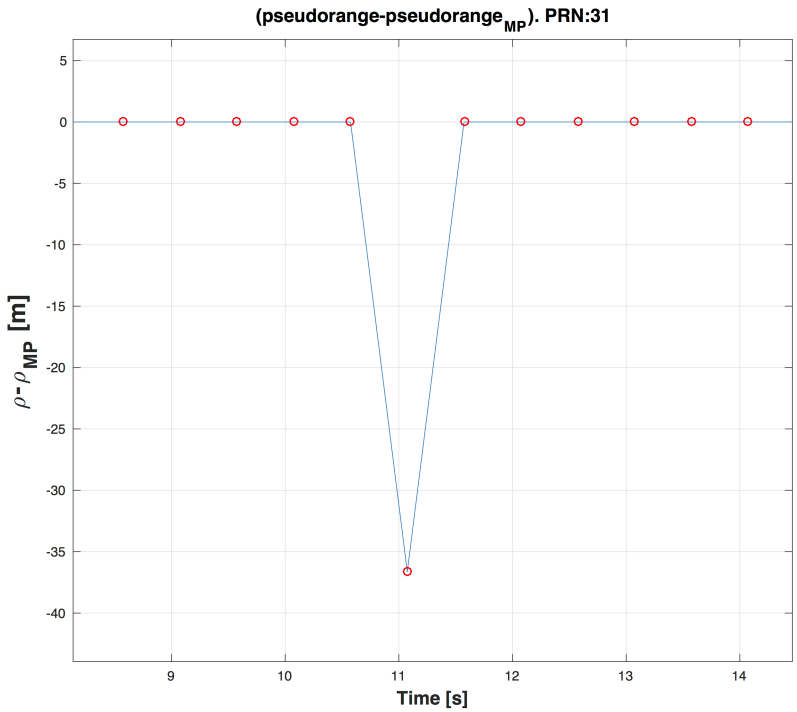

Fig. 4.7 Zoom around 10 s of $\rho_{clean} - \rho_{MP}$ in the case $\Delta T_\rho = 500$ ms in blue and MP profile in red.

is computed. In fact the PVT module of any GNSS receiver uses the estimated pseudoranges at some given epochs, and, as explained in Section 4.2.3, correlation distortions between two epochs could have an impact on the pseudorange estimation. The meaning of the function $s(\cdot)$ is to give a different importance to the MPDD output measurements depending on how far they are from the next pseudorange computation. The focus of this work is not to find an optimum $s(\cdot)$ so, by experimental assessment, for our receiver, we chose $s(\cdot)$ as a Gaussian function shown in Fig. 4.8.

- The function $d(\cdot)$ measures the ratio E_{min}/E_{LOS}, and it is defined as

$$d(kT_a) = \begin{cases} E_{min}/E_{LOS}, & \text{if } E_{min} \neq E_{LOS} \\ 1, & \text{if } E_{min} = E_{LOS} \end{cases}$$

$d(\cdot)$ is a ratio between distances, so it gives a relative measure of how far is $\hat{\mathbf{w}}$ with respect to the LOS.

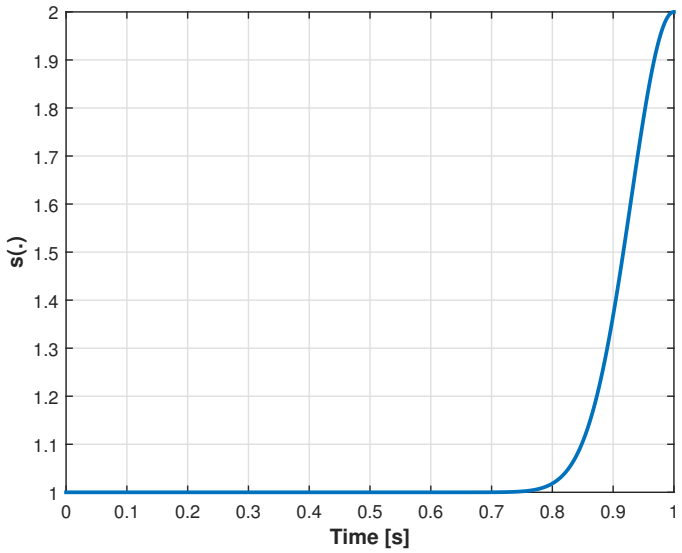

Fig. 4.8 Trend of $s(t)$ within two instants of the PVT computation.

- $f(\cdot)$ takes into account the C/N_0 value. The C/N_0 gives a measure of the reliability of the output of the MPDD. As a matter of fact, if C/N_0 is high, it means that the decision about the presence of distortions is more reliable than with low value of C/N_0. By using experimental data, we choose a valid function based on C/N_0. Therefore, an experimental assessment of the $f(\cdot)$ has been obtained by using NAVX-NCS ESSENTIAL GNSS SIMULATOR and simulating 1 hour of SIS signals without multipath and with different C/N_0. The data are then collected and processed by a fully-software GNSS receiver. In Fig. 4.9, the setup of the data collection is shown. The GNSS simulator is connected to the USRP that is the front-end able to downconvert the radiofrequency signal into baseband signal. The USRP has an external rubidium clock that provides a precise time reference for synchronization purpose. Then, the data are collected by the computer connected to the USRP. The signals transmitted by the simulator contain 8 SV in view each of them with a different value of C/N_0 as in Fig. 4.10. Starting from this situation where we know that no multipath rays are in the signals, by running the MPDD and counting the false alarm results of the detector per each channel, we try to estimate the false alarm probability P_{fa}. The $f(\cdot)$ function chosen is $1-P_{fa}$ and is plotted in Fig. 4.11 in function of C/N_0.

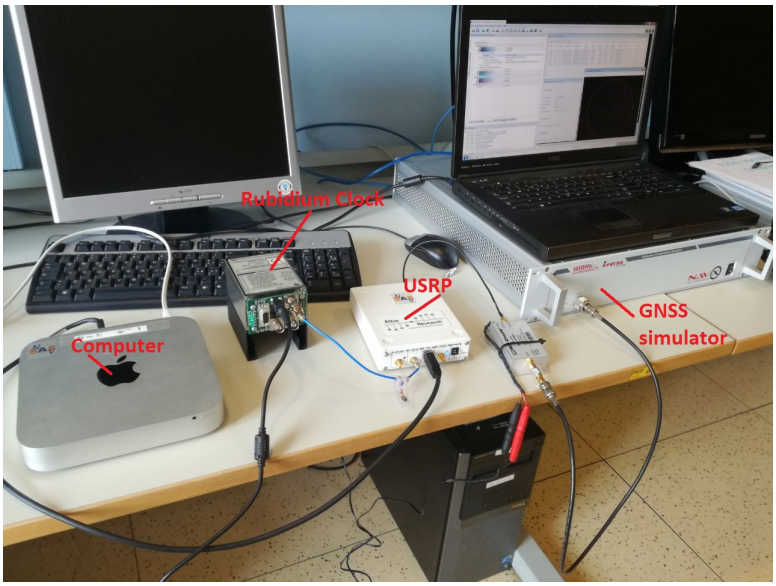

Fig. 4.9 Data collection setup.

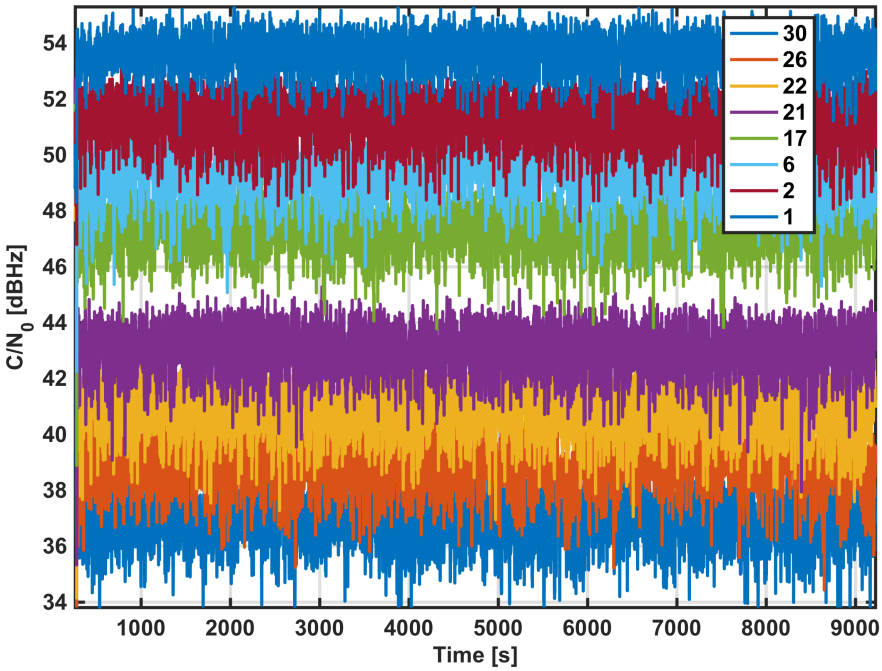

Fig. 4.10 C/N_0 trend over the time for all the 8 SV in view.

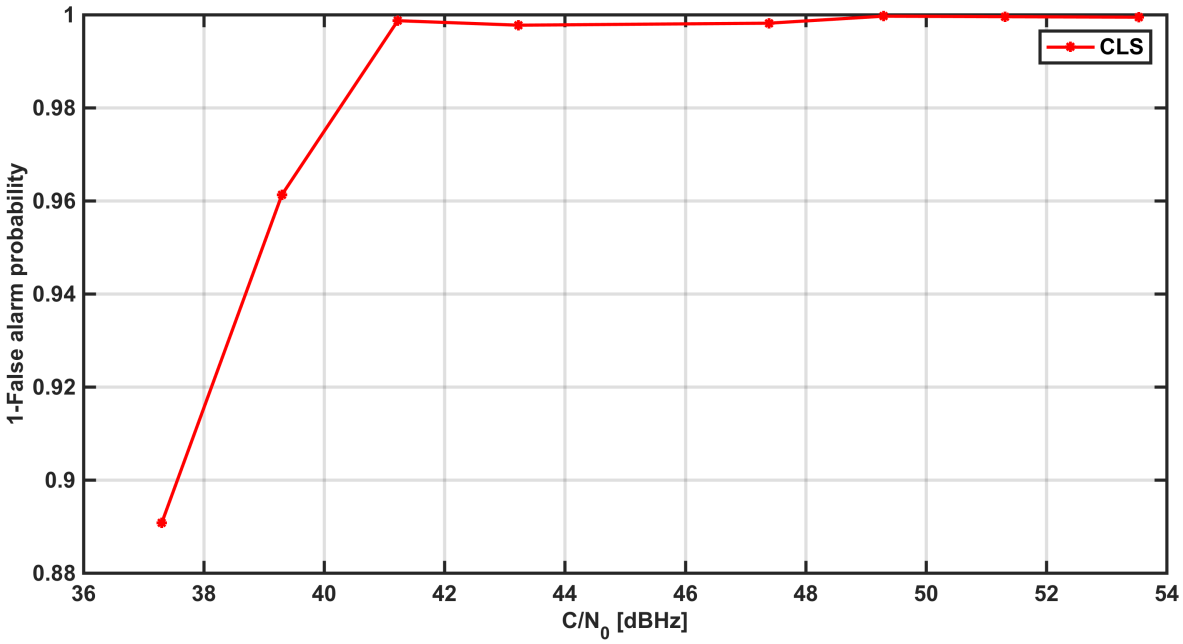

Fig. 4.11 $1 - P_{fa}$ curve in function of C/N_0.

It is important to choose a C/N_0 estimator that suits our problem. In [68] a comparison between five well-known methods to estimate the C/N_0 is made. We chose to use an estimator with low computational complexity, the *Signal-to-Noise Variance* (SNV), that is based on the first absolute moment and the second moment of the signal samples [68].

- λ is a normalization factor to obtain $\text{SQI}(t_n) \in (0, 1]$. The parameter λ is set as the sum of the maximum values that can be obtained at each discrete time k for the functions $m(\cdot)$, $s(\cdot)$, $d(\cdot)$ and $f(\cdot)$.

4.4 RAIM

Traditional RAIM techniques provide integrity information, by making use of the available measurements [59]. The basic assumption for RAIM for aviation applications is the presence of only one fault at the same time. This is a strong assumption, but the process may be iterated so including *de facto* the case of multiple faults. In literature three main RAIM algorithms are proposed and already presented in 2.2: range comparison, least-squares residuals and parity method. All the methods are able to determine the presence of a satellite

failure by using the redundancy of the measurements of the over-determined system of linearised equations

$$\boldsymbol{\Delta\rho} = \mathbf{H}\boldsymbol{\Delta x} + \boldsymbol{\epsilon}$$

where $\boldsymbol{\Delta x}$ is a vector containing the incremental deviations of the user position from the linearization point, $\mathbf{H}$ is the geometry matrix, where the generic row j is the unit vector pointing from the linearization point to the considered j-th satellite, and $\boldsymbol{\epsilon}$ is the vector of pseudorange errors. To detect position errors, RAIM requires at least five satellites in view, while the exclusion of the faulty measurements requires at least six satellites. The snapshot approach means that the system takes decision about the presence of failure by using only current considered observations.

In this chapter, we propose a method of assisted RAIM, based on the idea to detect satellite failures at tracking stage level, since errors like MP are much more visible in the correlation rather than at the pseudorange level.

4.4.1 Global and Local Test

The structure of a RAIM algorithm comes from the statistical detection theory [59]. Two hypothesis tests are posed: Global and Local Test. The first one tests if a failure exists and the second one identifies which is the failed satellite, under the assumption to have at most one failure at a time. In the residual method, the first step is to compute the residual between predicted and measured pseudoranges [69], $\hat{\mathbf{r}} = \mathbf{H}\boldsymbol{\Delta}\hat{\mathbf{x}} - \boldsymbol{\Delta\rho}$, given by

$$\hat{\mathbf{r}} = \mathbf{H}(\mathbf{H^T}\boldsymbol{\Sigma}^{-1}\mathbf{H})^{-1}\mathbf{H^T}\boldsymbol{\Sigma}^{-1}\boldsymbol{\Delta\rho} - \boldsymbol{\Delta\rho} = -\boldsymbol{R}\boldsymbol{\Delta\rho}$$

For the Weighted Least Squares (WLS) solution, if the pseudorange errors are normally distributed with covariance matrix $\boldsymbol{\Sigma}$, then the residuals are distributed as $\hat{\mathbf{r}} \sim N(0, \mathbf{R}\boldsymbol{\Sigma}\mathbf{R^T})$ [70]. The first test performed is the global test, which checks if a failure exists by calculating the value for the test statistic $T = \hat{\mathbf{r}}^{\mathbf{T}}\boldsymbol{\Sigma}^{-1}\hat{\mathbf{r}}$. If the error is a Gaussian variable with zero-mean, T follows a Chi-square distribution with $n-p$ DOF, where n is the number of measurements and p the number of parameters to be estimated. In other words, $n-p$ is the

number of redundant measurements. Therefore, once we get T, we need to compare it against a threshold value. To do this, we have to set a certain level of false alarm probability (α) and missed detection (β). If the current calculated T fails the test, the local test is performed to identify which is the faulty satellite. The elements of the residual vector $\hat{\mathbf{r}}$ are normalised by the diagonal elements of the covariance matrix of the residual and finally, we get $\hat{\mathbf{w}} \sim N(0,1)$. The fault exclusion is performed with the null and alternative hypotheses test with H_0: $|w_k| \leq n_{1-(\alpha_0/2)}$, where α_0 is the false alarm probability of the local test. The values of the parameters α, β and α_0 are linked together and, once two of them are fixed the third is obtained. The complete parameters computation is explained in [70]. The β parameter is involved for both global and local test (through the non-centrality parameter [71]). The complete sequence of the tests is shown in Fig. 4.12.

4.4.2 Covariance Matrix Uncertainty

In the simulations, the model for the pseudorange error variance is $\sigma_k^2 = a + b \cdot 10^{-0.1(C/N_0)}$, where k is the satellite index. The model is discussed in [72] and used in many other works [70], where the values a and b are constant and take into account the degradation caused by the environment. In [71] the authors suggest $a = 10$ m^2 and $b = 22500$ m^2 Hz for lightly degraded signal conditions. The implicit assumption is that the covariance matrix Σ is diagonal with entries $\sigma_1^2 \ldots \sigma_k^2$, but this in general is not true and the measurements are correlated, then the matrix entries out of the diagonal are different from zero [73]. In a non-aviation context, like road or railway, the covariance matrix is not generally diagonal [74, 75]. In [76] there is an example on how to deal with the uncertain covariance. For the experimental results we used a diagonal matrix, since the correct definition of a non diagonal matrix is out of the scope of this work.

4.5 SQI and RAIM interaction

The SQI introduced in the previous section has to be integrated within the algorithms of PVT and RAIM in order to improve the accuracy of the estimated

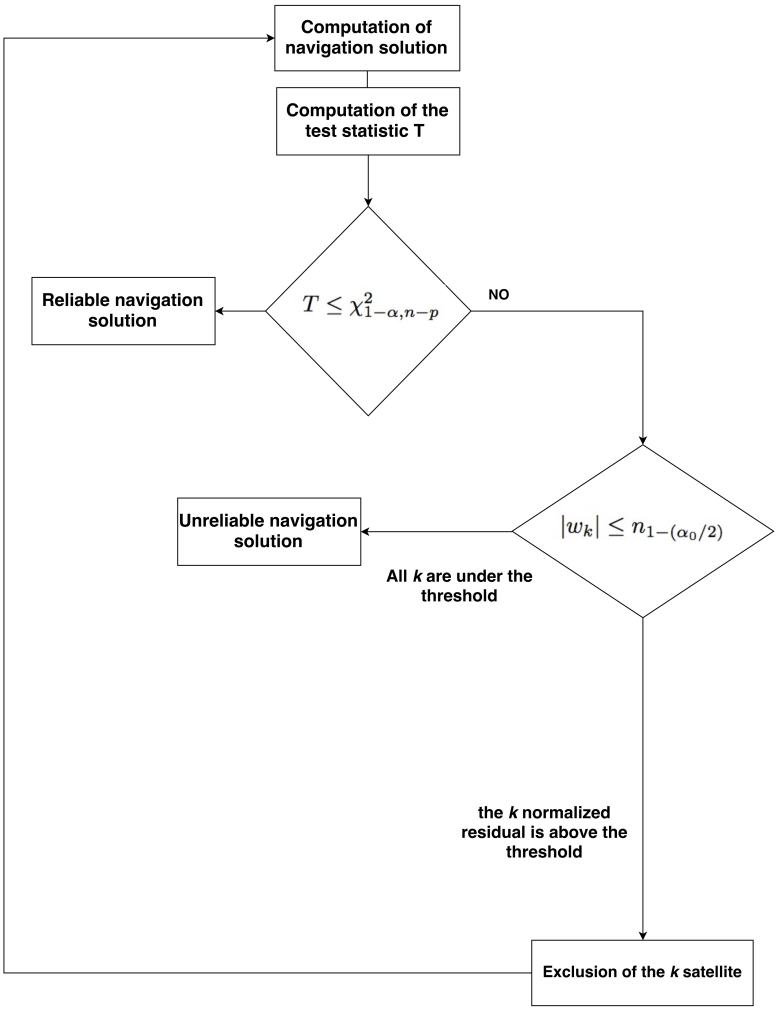

Fig. 4.12 Block diagram of the FDE algorithm.

position. The simplest integration method could be to set a threshold $\mathrm{SQI}_{\mathrm{thres}}$, and to exclude the satellites with $\mathrm{SQI} < \mathrm{SQI}_{\mathrm{thres}}$ from the PVT computation. However, in the case of a low number of satellites in view, the problem of the satellite-user geometry has an impact on the accuracy, and this should be considered in the mechanism of SQI/RAIM/PVT integration. This means that a trade-off has to be found, considering also the effect of the Geometric Dilution of Precision (GDOP) (or simply DOP) [3] , on the estimated position. In fact in some cases the error introduced by the worst DOP (due to a satellite exclusion) could be bigger than the error due to the effect of MPs in some of the satellites in view included in the PVT computation.

In the case of a bad geometry and of strong distortions, instead of removing degraded satellite signals from the PVT, another possible approach is to penalise satellites with a poor signal quality in the WLS solution of the navigation equations, by changing the diagonal noise covariance matrix Σ, as

$$\Sigma_{k,k}(t) = \sigma_k^2(t) + \sigma_k^2(t)\gamma(1 - SQI(t))$$

where γ is a penalty weight. The diagonal entry k can assume values from $\sigma_k^2(t)$, when SQI $= 1$ (corresponding to a signal in good conditions), to $(\gamma+1)\sigma_k^2(t)$ when SQI $= 0$ (corresponding to a strong distortion). In this way, we can reduce the effects of the errors in the pseudoranges projected in the position domain. This method is denoted as P-WLS in the following (where P stands for penalty).

4.5.1 Simulation Results without Using GDOP information

The purpose of the simulations in Section 4.2 is to show the effects of some MP distortions in the GNSS receiver. In order to validate this method we chose scenarios in which the MP phenomenon had longer durations than those of Section 4.2. We show simulation results obtained by processing these new scenarios, with different numbers of satellites in view, and with MP events that affect specific satellites in the time windows indicated in Table 4.2. The purpose is to analyze the effects of satellite exclusion and P-WLS, without

Scenario	MP Windows (s)	PRN
1	8–16	27
	21–25	11, 22
	30–35	16
	40–45	1, 4, 21, 27
2	20–80	1, 4, 21, 27

Table 4.2 Time windows when MP is present for the scenario 1 and 2.

considering GDOP data. For the PVT computation, the WLS solution is used. The RAIM algorithm used in simulation has a false alarm probability $\alpha = 5 \times 10^{-5}$ and missed detection probability $\beta = 5 \times 10^{-5}$. The two simulation scenarios represent the same static position and they have different durations and are presented in Table 4.2:

- Scenario 1 of duration of 50 s
- Scenario 2 of duration of 90 s

Both scenarios globally have 10 satellites in view.

When in the scenarios we consider only 5 chosen satellites in view, obviously FDE cannot be used for exclusion, but the anomalies on pseudoranges can be detected. An example of the position errors in East-North-Up (ENU) coordinates in scenario 1 with 5 satellites, without using RAIM and signal processing assistance, is shown in Fig. 4.13. In Fig. 4.14 the output of the detector, the SQI and the C/N_0 trend related to PRN 11 in scenario 1 is shown. The Tables 4.3 and 4.4 show the position errors in ENU coordinates in scenario 1 and 2 with several values of the penalty weight in the P-WLS method. The performance is also evaluated in terms of MSE over the whole duration of the scenarios. It is possible to observe that especially in scenario 2, where the environment is more degraded than in the scenario 1, the penalty on pseudorange variances can have a strong impact in terms of accuracy expressed in MSE. In scenario 1 the MP affects several PRN in different time windows but with shorter duration, so the penalty weight is between 0 and 1 except for the case with 5 satellites. In fact, in both scenarios another parameter that influences the choice of the penalty weight is the satellites geometry. If most of the satellite signals that we have are not affected by any impairment and also

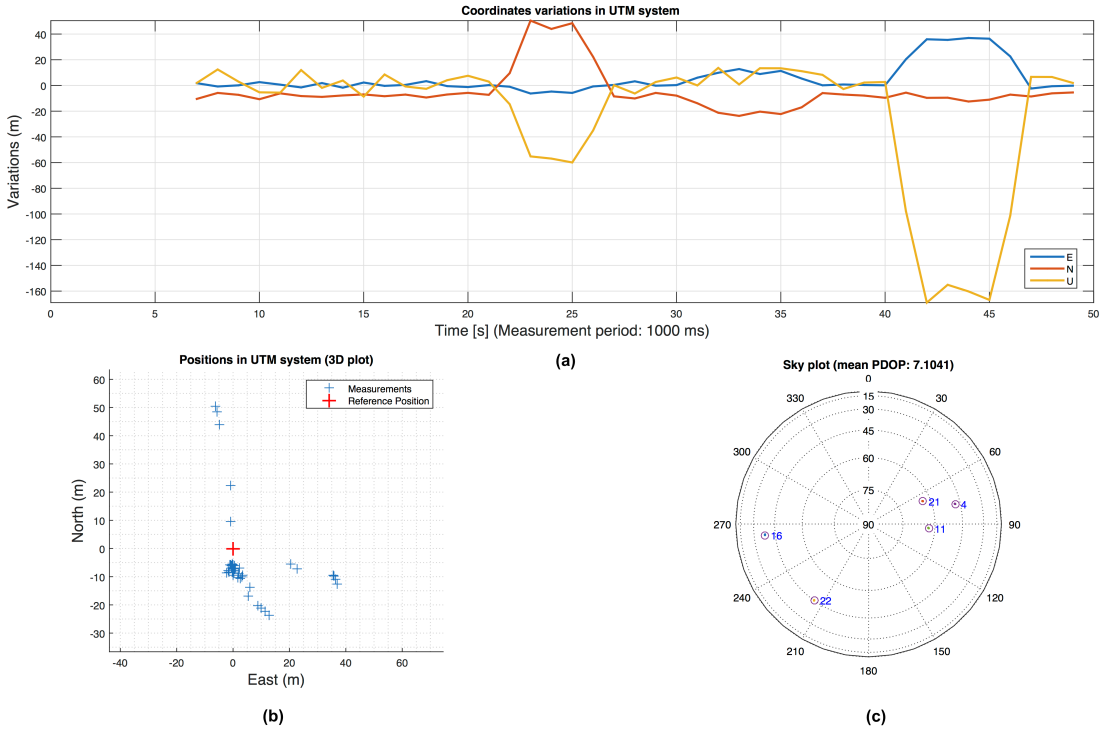

Fig. 4.13 WLS solution of the scenario 1. In (**a**) the position error is shown. The East-North coordinates (**b**) and the skyplot (**c**).

we have a good geometry, penalising the variances may be useless. Finally, the accuracy takes benefit from the penalty weight in a harsh environments.

The results summarised in Tables 4.5 and 4.6 show the effects of the exclusion performed by applying a threshold on SQI. The results have been obtained with $\mathrm{SQI}_{\mathrm{thres}} = 0.7$. As it can be seen in the first row of Table 4.5 relative to the case of 5 satellites, if we exclude one satellite with low SQI, we could get a worse solution due to the bad geometry. This is true with a low number of satellites, but the exclusion leads to an improved solution with a high number of satellites. In summary these results prove that the effect of GDOP has to be considered in the set up of the exclusion algorithms, when the number of satellites in view is very low.

Note that the focus of this chapter is to show that fault detection via signal processing techniques is possible and useful especially for land applications where the environment has important effects on the degradation of the signals.

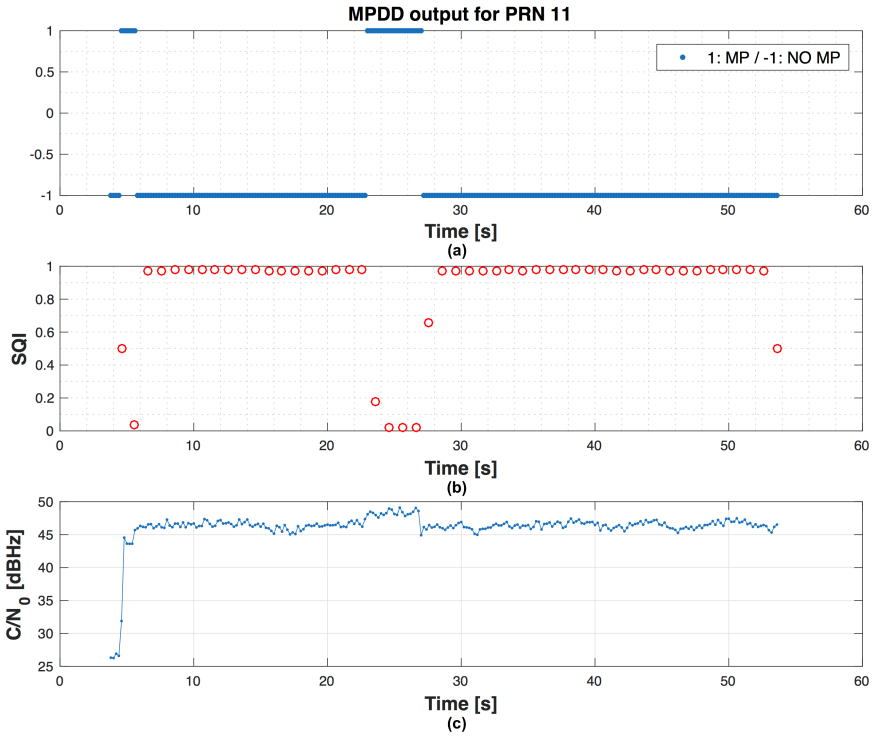

Fig. 4.14 Example related to PRN 11 in scenario 1: the MPDD output (**a**), the SQI (**b**) and the C/N_0 trend (**c**).

Num. of SV	γ	E (m)	N (m)	U (m)	MSE (m)
5	0	17.5	8.4	37.6	24
	1	17.5	8.4	37.5	24
	5	17.5	8.4	37.2	23.9
	10	17.5	8.4	37.1	23.9
8	0	11.7	9.1	31.6	22.8
	1	11.8	9.1	32.3	22.9
	5	12.2	9.1	34.2	23.3
	10	12.4	9.6	35.3	23.6
10	0	5.8	8.9	12.4	12.7
	1	5.8	8.9	12.2	12.5
	5	5.9	9.2	12.4	12.5
	10	5.9	9.4	12.8	12.7

Table 4.3 Results for the scenario 1 with increasing penalty weight and different number of satellites.

Num. of SV	γ	E (m)	N (m)	U (m)	MSE (m)
5	0	3	9.3	57.8	51.6
	1	1.8	6.4	45.9	41.3
	5	1.9	11.7	31.3	30.1
	10	2.5	14.4	26.4	27.2
8	0	8.3	10.9	41.9	38.8
	1	4.5	14.1	36.5	34.5
	5	2.3	16.1	31.1	30.1
	10	3.1	15.8	29.9	28.8
10	0	7	13.9	37.1	35.6
	1	3.6	16.1	29.9	30.3
	5	1.8	15.8	20.8	23.4
	10	2.2	14.3	17.4	20.2

Table 4.4 Results for the scenario 2 with increasing penalty weight and different number of satellites.

Num. of SV	E (m)	N (m)	U (m)	MSE (m)	PRN Tracked	RAIM	SQI Exclusion
5	12.6	16.7	56.8	36.1	16, 21, 22, 4, 11	NO	NO
	15.1	16.3	67.2	43.4		NO	YES
6	6.3	15.6	20.9	20.8	6, 16, 21, 22, 4, 11	NO	NO
	6	32.2	17.2	21.8		YES	NO
	6	32.2	16.2	21.5		YES	YES
7	6.5	14.8	13.8	17.4	6, 16, 21, 22, 4, 18, 11	NO	NO
	4.5	14.7	14	15.9		YES	NO
	4.6	14.7	13.6	15.9		YES	YES
10	5.8	8.9	12.4	12.7	6, 16, 21, 22, 4, 18, 11, 1, 19, 27	NO	NO
	3	8.5	8.7	10.5		YES	NO
	3.1	8.1	8.4	10.4		YES	YES

Table 4.5 Results for the scenario 1 with $SQI_{thres} = 0.7$ and no penalty weight.

Num. of SV	E (m)	N (m)	U (m)	MSE (m)	PRN Tracked	RAIM	SQI Exclusion
5	44.6	99.3	170.3	170.2	1 , 4 , 21, 27, 19	NO	NO
	159.4	136	395.7	323.5		NO	YES
6	44.7	90.4	147	150.4	1 , 4 , 21, 27, 19, 6	NO	NO
	30.9	65.6	109	110.9		YES	NO
	213.7	444.4	242.9	379.9		YES	YES
7	1.5	14.8	8.4	15.8	6, 19, 27, 16, 18, 4, 11	NO	NO
	1.5	14.8	8.4	15.8		YES	NO
	4	24.3	12.6	21.8		YES	YES
10	7	13.8	36.7	34.92	6, 19, 27, 16, 18, 4, 11, 22, 21, 1	NO	NO
	2.4	6.3	26.6	24.5		YES	NO
	2.7	10	8.5	11.9		YES	YES

Table 4.6 Results for the scenario 2 with $SQI_{thres} = 0.7$ and no penalty weight.

For this reason methods for a proper selection of the threshold are not considered in this chapter.

4.5.2 GDOP Control

The simulation results just presented motivate the adoption of an exclusion method able to implement a trade-off between the weights of errors removed by signal quality index and weights of the potential errors introduced by the geometry.

A possible approach is to calibrate the dictionary on specific error cases, in order to detect and remove satellites affected by these specific problems. A second approach is to consider that, in a future with a high number of satellites, the risk to degrade the DOP will be lower, but in any case, an additional block of DOP control is convenient for these kinds of algorithms.

We propose here a control, based on a GDOP budget, which tries to remove satellites starting from the ones with lowest SQI and $\mathrm{SQI} < \mathrm{SQI}_{\mathrm{thres}}$ in order to eliminate the distorted signals which could not be detected by the RAIM. Then a GDOP test can be performed, for example by observing if the GDOP after removal exceeds k times the GDOP with all the tracked channels. The idea is to combine several effects: calibration of the dictionary depending on the considered environment, and choice of the parameter k. In this heuristic way, we can have a kind of control even on the geometry effects, avoiding to introduce wide errors due to the weak geometry. For example, we set $k = 0.1$,

Number of Satellites	E (m)	N (m)	U (m)	MSE (m)	PRN Tracked	RAIM	SQI
	44.7	90.4	146.9	150.4	1 , 4 , 21, 27, 19, 6	NO	
6	30.9	65.6	109	110.9		YES	
	30.9	65.6	109	110.9		YES	
	1.51801	14.7719	8.40841	15.7991	6, 19, 27, 16, 18, 4, 11	NO	
7	1.5	14.8	8.4	15.8		YES	
	1.5	14.8	8.4	15.8		YES	

Table 4.7 Results for the scenario 2 with $SQI_{thres} = 0.7$, no penalty weight and GDOP control enabled with $k = 0.1$ in case of 6 and 7 satellites in view.

so it means that the new GDOP after a possible exclusion cannot exceed 10% of the previous GDOP. By taking in consideration the situation in Table 4.6 with 6 or 7 satellites, with GDOP control we do not perform an erroneous exclusion and we will get in this way the same results as in not assisted RAIM case (as reported in Table 4.7). Conversely, with 10 satellites, GDOP control simply permits the additional exclusion performed by SQI.

Another possible approach to avoid problems in case of a poor geometry is to leave the decision on the exclusion to RAIM algorithms but using SQI to identify unreliable navigation solutions. It is possible to declare a navigation solution unreliable when the global test fails but the local test is passed for all the normalised pseudorange residuals (see Figure 4.12). It means that a faulty situation is detected, but it is impossible to identify which is the faulty satellite and consequently RAIM cannot perform the exclusion. In this situation the RAIM algorithm is not able to provide information related to VPL and HPL.

Fig. 4.15 shows test results regarding scenario 1 with 9 satellites in view, without using SQI, with a false alarm probability $\alpha = 3.33 \cdot 10^{-5}$ and missed detection probability $\beta = 1 \cdot 10^{-2}$. The graph on top is the evolution in time of the global test statistic compared to the global threshold. Then, the local test is performed on the points above the global threshold. In the graph on bottom, the evolution in time of the local test statistic shows that there are only two points under the local threshold (circle points). These values under the local threshold are the navigation solutions which fail the global test, but pass the local one. By using SQI, we want to identify the possible biased pseudorange and exclude it to make reliable the navigation solution. To do this, after the global test failure and when local test is valid, instead of declaring an unreliable solution, we can check the SQI values for each satellite and decide to exclude

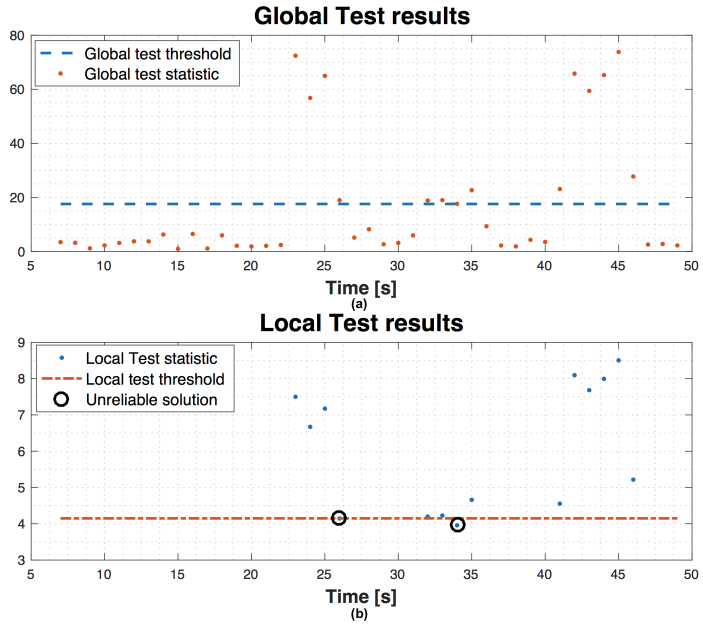

Fig. 4.15 Example of global (**a**) and local (**b**) test on scenario 1 with two unreliable solutions.

the satellite with the lowest SQI and repeat again the global and local test (if needed). In Fig. 4.16 the results of the assistance are shown. We observe that there are not points under the threshold in the local test graph, since after the exclusion, the global test is repeated and no more biases are detected and so the local test is not repeated.

4.6 Conclusions

This chapter presents a technique to detect the presence of distortions at the tracking stage level of a GNSS receiver. In particular the method has been tailored to MP detection, but can be applied also to other impairments. The specific goal is to assist the modules of integrity monitoring of RAIM. In the near future, the presence of a multi-constellation of satellites like GPS, Galileo, GLONASS, Beidou and of receivers able to demodulate all these signals, will provide an increasing number of satellites in view. This will foster the development of signal processing techniques of FDE, since they perform better with a high number of satellites. In general, this kind of exclusion approach is sensitive to the DOP variation, and the effects of the satellite geometry could

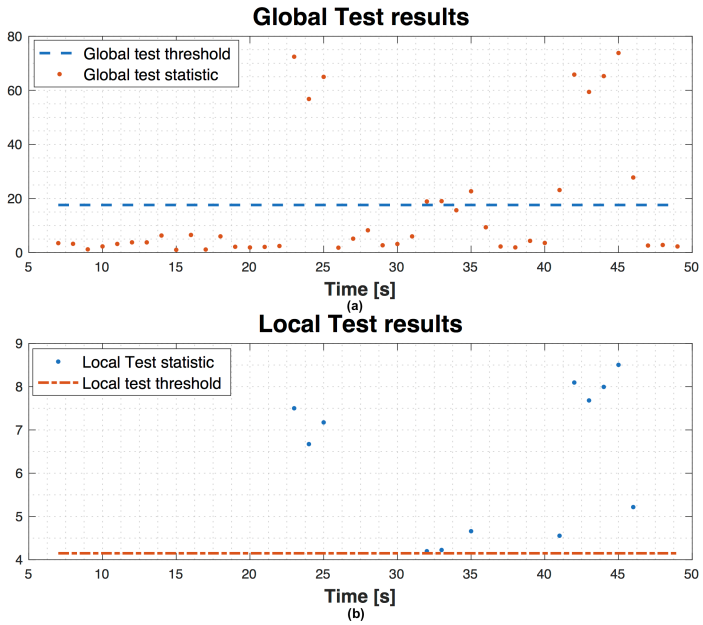

Fig. 4.16 Example of global (**a**) and local (**b**) test assisted by SQI information on scenario 1 without unreliable solutions.

be greater than a simple MP phenomenon in terms of accuracy. For this reason a method to combine GDOP control and FDE is also proposed in this work.

Another way to integrate SQI into RAIM suggested in this work is the exclusion of satellites with lowest SQI in case when RAIM declares a navigation solution as unreliable.

In this work, we have not taken into consideration a possible use of a carrier-smoothing techniques, that might be useful to protect against sporadic MP distortions, because usually they are used in the case of good visibility of the satellites in view.

The proposed technique could be also employed for other kinds of distortion, like spoofing attacks that can bypass RAIM tests. An application of the SQI to the spoofing is in Chapter 5.

Chapter 5

The use of the SQI in a different scenario: the Anti-spoofing case

This chapter is the result of a work in collaboration with fellow PhD student Esteban Garbin Manfredini. He works on developing spoofing detectors and mitigators. My contribution to this work was related to the signal processing part and how to use of SQI to monitor the quality of a signal affected by spoofing interference. Then we developed the tracking jumping procedure to try to mitigate the effects of a spoofer. GNSS navigation and positioning is the core of many applications, such as geofencing [77], that requires a granted level of trustworthiness.

In recent years, one of the major security threats concerning the GNSS users is the so-called spoofing menace. These spoofing attacks consist on the transmission of a counterfeit satellite-like radio frequency signal, in order to gain control of the GNSS receiver and cause it to compute erroneous PVT solutions [78–80]. Spoofing attacks have been proved to be possible [81, 82] and the new software defined ratio technologies are making the spoofing attacks easier to be implemented.

In the framework of this research we focused on the so-called intermediate spoofing attack [83]. An intermediate spoofer consists of a device capable of receiving GNSS signals and generating counterfeit signals. The spoofers extracts time, position, and satellite information from the received signals, and then leverages the synchronization of the local codes and carriers to generate

plausible counterfeit signals [78]. Different kinds of configuration of intermediate attacks have been proposed such as over-powered or matched power attacks [84, 85].

On the other hand, several anti-spoofing techniques have been proposed over the past years [79, 80]. Some of these methods use antenna arrays to obtain information on the direction of arrival with respect to the satellite elevation and discriminate between the satellite and the spoofing signal [86–88]. Other techniques cross-check GNSS measurements with other externals systems, such as, inertial or communications systems [89–91]. Different solutions are based on the authentication of the satellite signal, in order to avoid the reception of unauthorized signals [92–94]. Finally, there are other methods, based on signal processing, designed to detect the spoofing signal exploiting by observables taken at different stages of the receiver, such as, the Carrier-to-Noise ratio (C/N_0) or the correlation function shape [95, 85, 89, 96–98].

Even though many of the existing signal processing techniques are designed for detecting spoofing attacks, only a few of them are able to mitigate its effects, e.g. [96, 99]. In this chapter we propose a novel anti-spoofing signal processing algorithm, called TJ. It is based on the idea used in Chapter 3, where multiple correlators are used to observe the correlation function between the incoming signal and the local replica for MP detection purposes. In this work, a similar concept is developed using a different linear regression algorithm [100]. The TJ algorithm aims at detecting the spoofing signal and mitigating its effects by unlocking the receiver from the spoofing control and track the satellite signal instead.

In this chapter we focus on the matched-power intermediate spoofing attack with the goal of introducing the novel TJ algorithm and demonstrating its feasibility, in particular, on the vehicular context and its applications. For the test phase we used the TEXBAT as the main source for demonstrating the working abilities of the algorithm. The TEXBAT is a set of recorded scenarios, made available by the Radionavigation Laboratory at the University of Texas at Austin, created to provide a test-bench for the evaluation of anti-spoofing techniques performance, both in static and dynamic scenarios [84]. The TJ algorithm, by itself, is not conceived as a defense against the over-powered

types of spoofing attacks, but these are easily detectable by means of a power measurement control and can be a priori excluded [101].

By means of the TJ algorithm, the receiver is able to maintain availability of the GNSS usage and obtain trusted positions by using the mitigated signal. Due to the presence of vestigial spoofing signals, the accuracy of the mitigated positions is slightly degradated with respect to the position obtained using clean signals.

The chapter is organized as follows: in Section 5.1 we outline the overall working procedure of the TJ algorithm. In Section 5.2 we detail the spoofing signal detection algorithm based on the linear regression algorithm. Following, in Section 6.1.1 we describe the two different KFs used inside the TJ algorithm. In Section 5.4 we present the delay estimation algorithm and jumping procedure to unlock the signal from the spoofing control. Finally, in Section 6.5 the working results for the TJ algorithm are discussed and in Section 5.6 the conclusions are drawn.

5.1 The Time Jumper principle

The flow chart of algorithm describing the TJ working principle is depicted in Fig. 5.1, where three main sections of the algorithm can be identified, the detection part, the PVT part, and the jumping part.

The detection part is in charge of revealing the spoofing presence and of its exclusion from the navigation solution. The detection is based on a SQI able to measure the difference between the received signal and the ideal one. The SQI is defined by using the correlation function between the received signal and the local code replica, and other signal information, such as C/N_0. The SQI value is the metric used for the detection and exclusion of the faulty satellites from the PVT computation. A detailed description of the detection part is presented in Section 5.2.

The PVT part, described in Section 6.1.1, regards the use of KFs in the PVT computation. There are two different KFs used in the algorithm, one used when enough unspoofed channels are available to compute a trusted solution

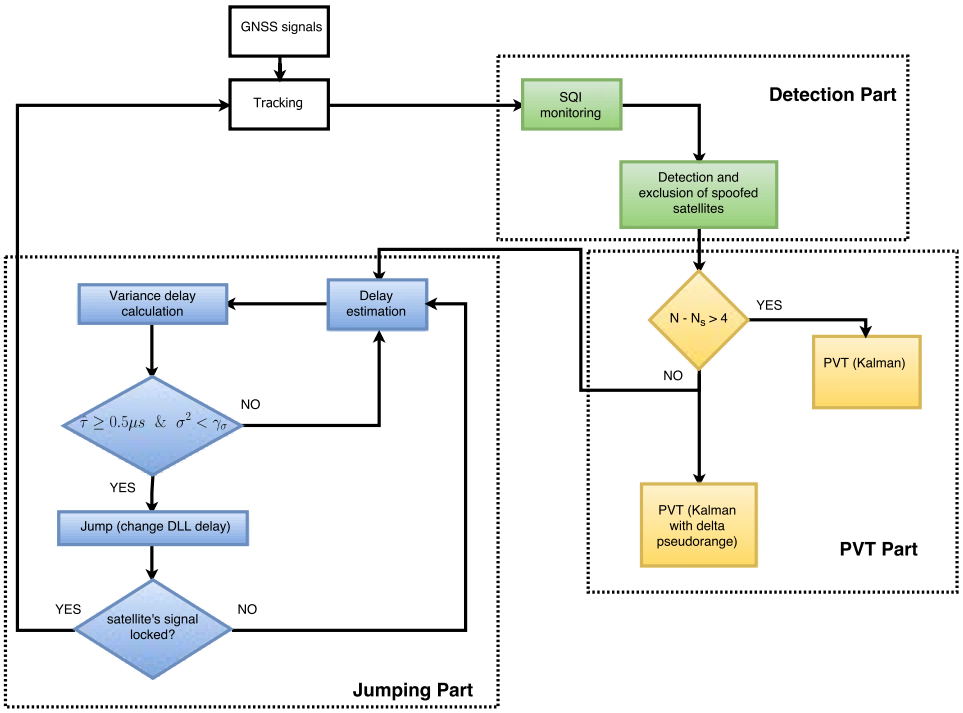

Fig. 5.1 Flow chart of the functioning principle of Time Jumper algorithm

and the second one when a solution cannot be found using only the unspoofed ones.

Finally, In Section 5.4 we discuss the jumping part that is in charge of unlocking the channel's DLL from the control of the spoofer and make it lock to the authentic signal. During this procedure, we first estimate the relative delay between the spoofing and the satellite signal by observing the correlation function shape. Afterwards, a delay jump is performed by modifying the absolute delay of the DLL using the estimated delay difference. After the jump, appropriate checks to control if the jump was performed correctly are done.

The detection strategy and the PVT computation are based on previous research and known results. The jumping procedure is the major novel contributions of this work.

5.2 Detection problem

The detector used in the scheme of Fig 5.1 is a modified version of the MPDD algorithm introduced in Chapter 3. This algorithm works at the correlation level and it is able to detect distortions of the correlation function. Since MP and spoofing signals may create similar distortions in the correlation function, it is possible to use a variant of the MPDD algorithm to detect spoofing signals. In spite of the similarities in the distortion, there are subtle differences that can be considered when detecting one or the other. For example, a spoofing attack is expected to create a single additional ray apart from the LOS signal, while in MP environments many different rays can be mixed with the LOS signals.

The MPDD is based on the use of LAFs. In this work we substitute the LAFs by a Least Absolute Shrinkage and Selection Operator (LASSO) [100], which provides, in the framework of spoofing detection, better detection capabilities. Furthermore, the algorithm is improved by the introduction of a quality index that will be used to exclude low quality signals.

5.2.1 From Linear adaptive filter to LASSO

The idea described in Chapter 3 is to use LAF to decompose the correlation of the incoming signal in a weighted sum of delayed ideal correlations in order to detect MP reflections of the LOS in the correlation domain, without any limitation on the number of reflections. In the LAF theory, a generic signal is modeled as $d[n] = y[n] + n_0[n]$, where $n_0[n]$ is a noise sequence and $y[n]$ is a signal defined as the output of a FIR filter:

$$y[n] = \sum_{k=0}^{M-1} w_k^* u[n-k] \tag{5.1}$$

according to (5.1) $y[n]$ is written as a summation of M delayed and weighted replicas of a basis input signal $u[n]$. The filter length M depends on how many delayed replica signals are used to approximate $d[n]$. In Chapter 3, $u[n]$ is the ideal correlation of a GPS L1 C/A signal and $d[n]$ is the measured correlation between the local code and the incoming one averaged in a time window. In order to limit the effect of the noise in the receiver, the measured correlations

are collected in time and then averaged before applying the LAF decomposition. The taps of the filter w_k are considered as the unknowns of the system and they are computed by minimizing the residual error $e[n] = y[n] - d[n]$. This minimization problem can be written in matrix form as:

$$\min_{w} \quad ||\mathbf{Uw} - \mathbf{d}||_2^2 \tag{5.2}$$

where $\mathbf{U} \in \mathbb{R}^{N \times M}$ contains M delayed ideal correlations and $\mathbf{d} \in \mathbb{R}^{N \times 1}$ is a vector of measured correlation points. Equation (5.2) is a typical least square minimization problem, solved as $\hat{\mathbf{w}} = (\mathbf{U^H U})^{-1}\mathbf{U^H d}$. The vector $\hat{\mathbf{w}} \in \mathbb{R}^{M \times 1}$, containing the taps of the linear filter, is used to characterize the presence of external signals. The value of the central tap weights the ideal correlation with zero delay and is related to the LOS signal, while the values of other taps are linked to the presence of possible MP signals and noise.

The rule chosen here to detect the presence of distortions is the same used in Chapter 3, so the anomalies are present if the distance between the estimated coefficient vector $\hat{\mathbf{w}}$ and the vector representing LOS in the dictionary case is not minimum.

In the spoofing attack scenarios the problem is similar. Although there are distortions in the correlation domain, only one additional signal is present when a receiver is under a spoofing attack. The minimization problem expressed by (5.2) can be modified, taking into account the fact that we are looking for a single additional signal. The new formulation of the problem has to guarantee a limited number of non-zero components of the vector $\mathbf{w}$. This is possible by adding a constraint so that:

$$\begin{aligned} &\min_{w} && ||\mathbf{Uw} - \mathbf{d}||_2^2 \\ &\text{subject to} && ||\mathbf{w}||_0 < s \end{aligned} \tag{5.3}$$

where $||\mathbf{w}||_0$ is the pseudo ℓ_0 norm defined as

$$||\mathbf{w}||_0 = |\text{supp}(\mathbf{w})|$$

and where $|\cdot|$ is the cardinality of the set $\text{supp}(\mathbf{w}) = \{\mathbf{w} : w_i \neq 0\}$. The integer number s is used in order to do this minimization and limits the ℓ_0 norm of the vector $\mathbf{w}$, so s indicates the maximum number of non-zero components. A

possible choice is to select $s = 2$, in order to represent only the LOS and the spoofed signal. Nevertheless, the replicas in $\mathbf{U}$ have fixed delay values while the LOS and the spoofing signals may fall between two replicas, as shown in Fig. 5.2 and this leads to $s \geq 4$. To limit the complexity of the overall representation we chose $s = 6$.

The problem in (5.3), an ℓ_0 *constrained least square*, is a non-convex and NP-hard problem [54]. In order to solve it, a possible approach could be to use greedy algorithms like *iterative hard thresholding* [102] or, as an alternative, we relax ℓ_0 and solve an approximated version of the problem, using the ℓ_1 norm [103].

In this work, we are more interested in highlighting the presence of components than approximating the input signal in the best way. The convex problem

$$\begin{aligned} \min_{w} \quad & ||\mathbf{U}\mathbf{w} - \mathbf{d}||_2^2 \\ \text{subject to} \quad & ||\mathbf{w}||_1 < s \end{aligned}$$

is referred to as the LASSO problem [100, 104]. Given the nature of the constraints, the LASSO tends to produce several coefficients that are exactly zero [105] and this behavior fits well with the desired representation. In our case, we have $\mathbf{w} \in \mathbb{R}^{M \times 1}$ with $M > s$, so the solution will have at most s components different than zero. In Fig. 5.2 we can observe an example of the LASSO applied to decompose input correlation $\mathbf{d}$ and approximate it as $\mathbf{y} = \mathbf{U}\mathbf{w}$. The vector $\mathbf{w}$, obtained by the LASSO solution, used for detection purposes will also be used in Section 5.4.1 to estimate the relative delay between LOS and spoofing signals.

5.2.2 The use of SQI

Another element of the proposed method is the use of the heuristic metric introduced in Chapter 4 that evaluates the quality of the signal.

In Figs. 5.3 and 5.4, two examples of MPDD binary outputs are depicted, the SQI results and C/N_0 trend respectively. The results presented hereafter were obtained by processing two channels of TEXBAT dataset number 4, where it is easy to observe the time epoch when the distortion appears in the

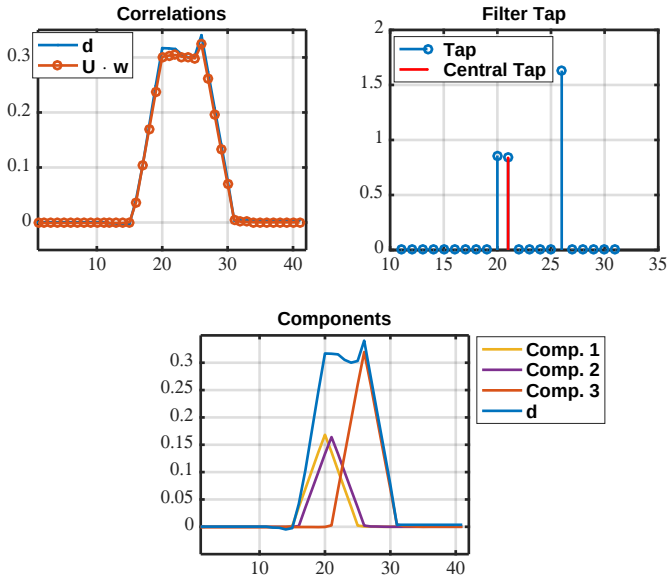

Fig. 5.2 Example of measured correlation **d** and its approximation, tap of the filter (**w**) and weighted decomposition

correlation function, and the effects that it has on the SQI of each channel. Scenario number 4 of TEXBAT is a matched-power static position push that serves the purpose to validate the definition adopted for the SQI.

5.2.3 Exclusion rule

A spoofing attack is able to alter the delay of each satellite signal at different times and with different trends. The mitigation of the dangerous spoofing effects cannot be based only on SQI, since a low SQI does not necessarily indicate that the receiver is under spoofer attack. In our method we declare the spoofing presence by combining the information given by SQI and the duration of the event. We chose that when one of the channel's SQI is below a predefined threshold $\gamma_{\text{SQI}} = 0.6$ for an amount of time $T_{\text{SQI}} = 10$ s, the channel is excluded from the navigation solution. Once a channel is excluded, the remaining healthy ones are used to compute the PVT solution by means of a classical KF. The algorithm will continuously monitor the channels and exclude the impaired ones. If there are less than four channels declared healthy, the algorithm will switch to the KF version used under spoofing attack, and the solution will be

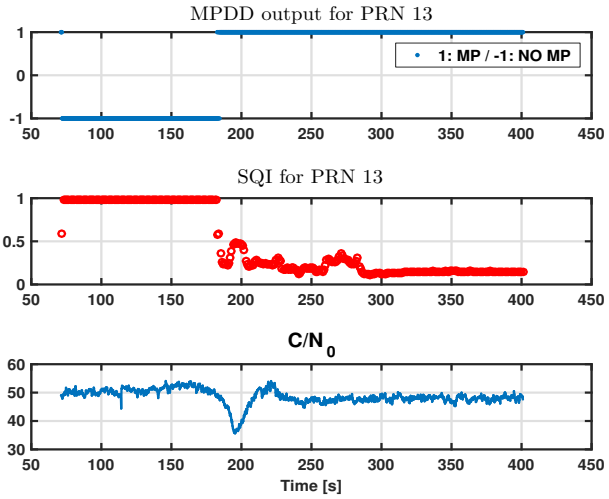

Fig. 5.3 Example of detection results for satellite 13, using TEXBAT scenario ds4. The attack is detected after 180 s, when the spoofer tries to change the true delay computed by the receiver.

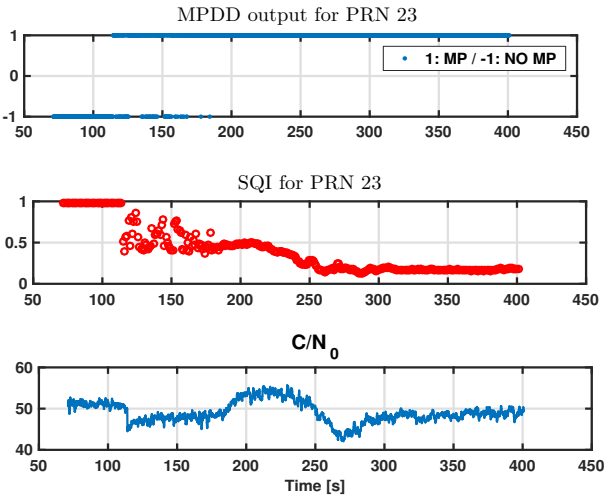

Fig. 5.4 Example of detection results for satellite 23, using TEXBAT scenario ds4. The attack is detected after 110 s, when the spoofer tries to change the true delay computed by the receiver.

computed using only Doppler measurements as it will be explained in Section 6.1.1. At the end of the procedure, a number N_s of satellites will be excluded, where $0 < N_s \leq N_T$ and N_T is the total number of satellites.

5.3 Kalman Filter

When $N_T - N_s \geq 4$, N_s satellites are excluded from the solution based on the KF using only the non-spoofed code and Doppler measurements, otherwise, when $N_T - N_s < 4$, the N_T Doppler measurements are used by the KF. This double choice provides an overall better performance, in terms of continuity and accuracy, as it will be shown in Section 6.5.

Both discrete KFs architectures are based on the description presented in [3, 106] and the notation used, referring to time t_k, is:

- $\mathbf{x_k}$ is the process state vector
- $\mathbf{\Phi_k}$ is the state transition matrix relating $\mathbf{x_k}$ to $\mathbf{x_{k+1}}$ in the absence of a forcing function
- $\mathbf{z_k}$ is the measurement vector
- $\mathbf{H_k}$ is the matrix giving the ideal connection between the measurement and the state vector
- $\mathbf{v_k}$ is the vector containing the measurement error, which is assumed white with known covariance and zero crosscorrelation with $\mathbf{w_k}$
- $\mathbf{Q_k}$ is the noise covariance matrix associated to the Kalman linear model

In a classical KF the state estimate is given by:

$$\hat{\mathbf{x}}_\mathbf{k} = \hat{\mathbf{x}}_\mathbf{k}^- + \mathbf{K_k}(\mathbf{z_k} - \mathbf{H_k}\hat{\mathbf{x}}_\mathbf{k}^-)$$

where $\mathbf{K_k}$ is the Kalman Gain computed as:

$$\mathbf{K_k} = \mathbf{P_k^-}\mathbf{H_k^T}(\mathbf{H_k}\mathbf{P_k^-}\mathbf{H_k^T} + \mathbf{R_k})^{-1}$$

The error covariance update is:

$$\mathbf{P_k} = (\mathbf{I} - \mathbf{K_k H_k})\mathbf{P_k^-}$$

The state estimate prediction is given by:

$$\hat{\mathbf{x}}_{\mathbf{k+1}}^{-} = \mathbf{\Phi_k}\hat{\mathbf{x}}_{\mathbf{k}}$$

and the error covariance extrapolation is computed as:

$$\mathbf{P}_{\mathbf{k+1}}^{-} = \mathbf{\Phi_k P_k \Phi_k^T} + \mathbf{Q_k}$$

5.3.1 Case $N_T - N_s \geq 4$

Thanks to the detection and exclusion stage, the KF used in this case works with only non-spoofed signals. A KF with eight states is used, considering four states for the position and timing and other four states for their respective derivatives. The error state vector is:

$$\mathbf{e}_k = \begin{bmatrix} \delta\mathbf{x} \\ \delta t \\ \delta\dot{\mathbf{x}} \\ \delta\dot{t} \end{bmatrix}$$

where $\delta\mathbf{x}$, is the vector related to the position coordinates x, y and z and $\delta\dot{\mathbf{x}}$ is the vector related to the velocity coordinates. This architecture is used as soon as the receiver is turned ON and it is maintained while $N_T - N_s \geq 4$.

Using the non-spoofing KF, the measurement vector at time t_k is obtained as:

$$\mathbf{z}_k = \begin{bmatrix} \mathbf{r} \\ \dot{\mathbf{r}} \end{bmatrix}$$

where $\mathbf{r}$ contains the code-based pseudoranges measurements minus the predicted measuremtns and $\dot{\mathbf{r}}$ is computed using the Doppler measurements obtained from the PLL. Under non-spoofing conditions, the matrix describing the connection between the measurements and the state vector at time t_k is given by:

$$\mathbf{H}_k = \begin{bmatrix} \tilde{\mathbf{r}}_{x,y,z} & 1 & 0 & 0 \\ 0 & 0 & \tilde{\mathbf{r}}_{x,y,z} & 1 \end{bmatrix}$$

where $\tilde{\mathbf{r}}_{x,y,z}$ is the unit vector from the user to the satellite, computed using the satellite position and the user's previous positions. This is the structure of the KF generally used to obtain the PVT solution.

5.3.2 Case $N_T - N_s < 4$

In this case it is not possible to obtain a solution using only non-spoofed pseudorange measurements, and in this condition, we switch to a KF version which uses all N_T available Doppler measurements. The motivation is that, in the dataset used to validate the method, the Doppler measurements are not spoofed.

This version of KF uses also eight states but provides a PVT solution using only Doppler measurements obtained from the PLL.

To compute the solution, the measurement vector $\mathbf{z}_k$ and its connection matrix $\mathbf{H}_k$, are changed as:

$$\mathbf{z}_k = \begin{bmatrix} \mathbf{0} \\ \dot{\mathbf{r}} \end{bmatrix}$$

and

$$\mathbf{H}_k = \begin{bmatrix} 0 & 0 & 0 & 0 \\ 0 & 0 & \tilde{\mathbf{r}}_{x,y,z} & 1 \end{bmatrix}$$

With these changes, the KF completely ignores the pseudorange measurements and relies only on the phase measurements and previous positions.

5.4 Delay Estimation and Jump

5.4.1 Delay Estimation method

As introduced in Section 5.2, for the delay estimation between LOS and spoofer, we use the correlation decomposition performed by the LASSO algorithm. If, during the detection phase, we identify the presence of additional signals in the

correlation function, then the distance between the non-zero taps of the filter are representative of the relative delay between them. Obviously, this estimated delay has a resolution given by the number of taps of the filter ($\mathbf{w} \in \mathbb{R}^{M\times 1}$) and by the range of the multicorrelator used, i.e $T_{range} = 2T_{chip} - (-2T_{chip}) = 4T_{chip}$. Using a greater number of taps, maintaining a fixed T_{range}, provides higher resolution in time.

The ideal correlations are contained in the matrix $\mathbf{U} \in \mathbb{R}^{N\times M}$ whose columns contain shifted versions of the ideal correlation, with a single point shift between two adjacent columns. The choice of M with respect to T_{range} affects the number of possible delayed replicas, the number of columns of $\mathbf{U}$ and, indirectly, the computational load. Hence, the choice of the resolution needs to meet a trade-off between computational load and the range of the multicorrelator T_{range}. In the experiments presented in this chapter we selected $M = 21$ and $T_{range} = 4T_{chip}$ in order to limit the computational load and to have a range wide enough to observe external signals that are well separated from the LOS one.

Once decided M and T_{range}, we need a technique to estimate $\hat{\tau}$. The first and intuitive approach could be to observe directly the vector $\hat{\mathbf{w}}$ and count the number of taps between the two coefficients different from zero. This approach is possible if we have only 1 (LOS case) or 2 (LOS + spoofer) coefficients different than zero. Unfortunately this is generally not true because of three factors:

- the presence of noise that could create small additional coefficients (Fig. 5.5)
- the constraint s in the LASSO, that allows to have more than 2 taps for the approximation if $s > 2$ (Fig. 5.6)
- the resolution. Since the true delay τ is not generally an integer multiple of the distance between two adjacent taps, LASSO will use the combination of two adjacent taps when LOS or spoofer correlation peaks are between two taps.

The developed technique takes into account these factors in order to have a better delay estimation and it is called Barycenter Delay Estimation (BDE). The idea is to first remove possible taps with low values, caused by noise,

through hard-thresholding, and then, if there are two remaining non-zero coefficients, count the number of taps between them and multiply it by the resolution T_{res}. If the remaining coefficients are more than two, we observe $\mathbf{w}$ and compute all barycenters between adjacent taps. Finally, the delay will be the distance between the two highest barycenters. An example is shown in Fig. 5.6.

Using GPS L1 C/A signal, the correlation functions are all triangles with the same base b and the heights are related to the amplitudes of the coefficients of $\mathbf{w}$. The barycenter will be computed as:

$$t_{bar} = \frac{iA_i + (i+1)A_{i+1}}{A_i + A_{i+1}} \cdot T_{res}$$

where $A_i = bw_i$ is the area of the triangle associated to the w_i coefficient. In Fig. 5.7, we show an example of delay estimation vs. time for three satellite signals using the dataset number 6 of the TEXBAT.

In Fig. 5.7, we observe that around 120 s the spoofer starts the push-off phase, the estimated delay starts growing and after some time the estimation stabilizes around a final value for each channel. At the beginning of the attack, from 50 to 120 s, when the spoofing signal is aligned with the satellite signal, the estimation is more difficult because of the smaller distance between two peaks. This Figure shows that the technique has difficulties in detecting additional signals that are perfectly aligned to the LOS signal. Fortunately, these scenarios do not present real threats to the PVT solution.

5.4.2 Pre-Jump Checks

In general, during spoofing attacks, the estimated delay $\hat{\tau}$ will be a non constant parameter, that will be under the spoofer control and will be modified accordingly. Nevertheless, given the nature of a spoofing attack, in order to adequately manipulate the target's position and to avoid that the receiver loses the tracking lock, a spoofer will generally alter the delay information slowly, on the order of 20 ns/s. Therefore, for adequately small time windows, $\hat{\tau}$ can be considered constant and its variance can be calculated accordingly. We can use the absolute value of $\hat{\tau}$ and its variance, in order to decide if the estimations

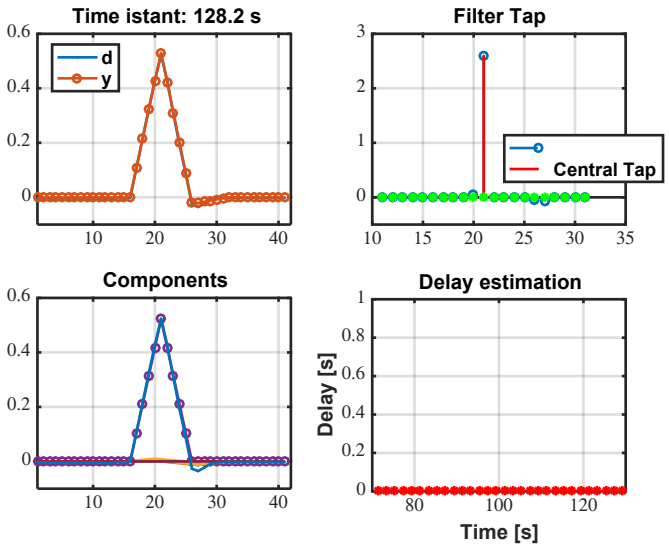

Fig. 5.5 Clean scenario with only the true signal and noise. The measured correlation is clean, with only the central tap (0-delayed replica) different from zero. This means that only one signal component is present in signal correlation.

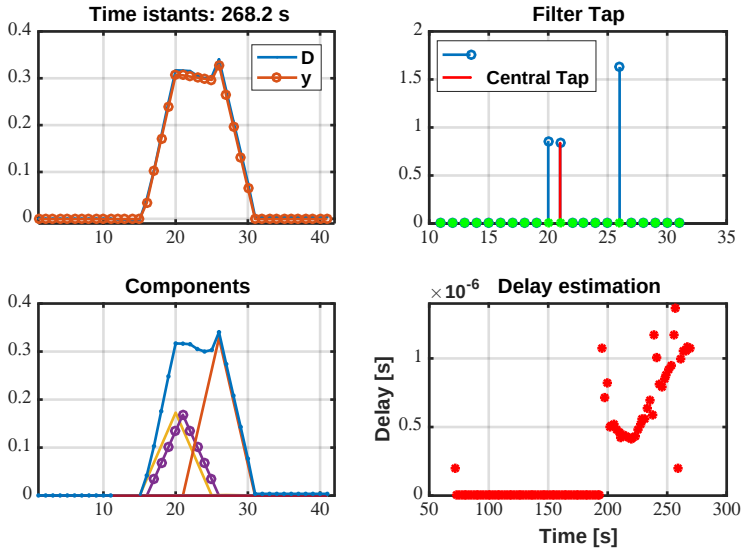

Fig. 5.6 Spoofed scenario in a generic time instant. The distortion in correlation domain is visible also in the number of taps different from zero. Therefore, it is possible to estimate the relative delay between the authentic and the spoofing signal

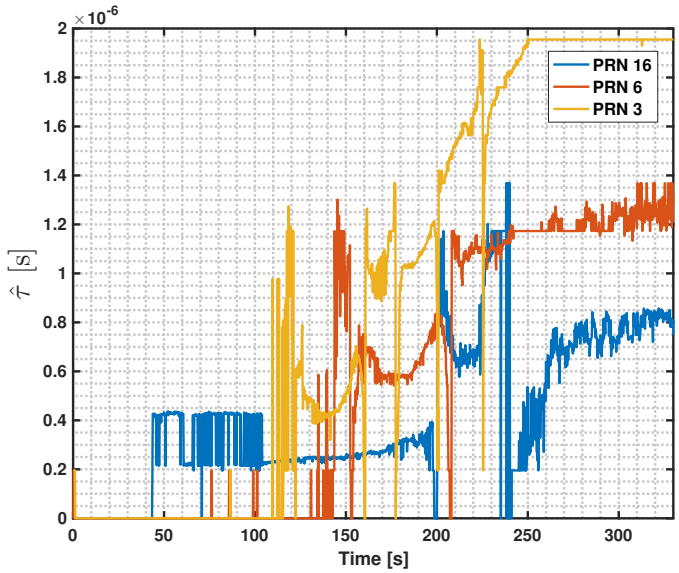

Fig. 5.7 Temporal evolution of delay estimation. Example for 3 different satellites. Not until 120 seconds the spoofer starts the push-off phase of the attack, separating the two peaks from each other

are correct and the authentic peak is being observed. If these conditions are met, the time jump can be performed during that time instant.

Two basic checks are done in order to identify if the current time is suitable for jumping or not. First we check that the estimated delay is at least $0.5\mu s$. This empirical threshold is used to give the possibility for the two signals to be sufficiently apart and for the two peaks to be clearly visible in the correlation function. In case of an unsuccessful jump, an after-jump check is used, as shown in Section 5.4.3.

The second check consists in observing the variance of the delay estimation within a time window. If the variance during one second of the delay estimation is lower than a predefined threshold γ_σ, the estimation is stable and the channel is ready to jump. We can define the checks as:

$$\hat{\tau} \geq 0.5\mu s \text{ and } \sigma^2_{\hat{\tau}} < \gamma_\sigma \tag{5.4}$$

These checks are done on each channel individually. We jump on all the satellites at the same time, because in case of an attack that leaves, at least, four non-spoofed satellites, the receiver is able to continue the operation. In

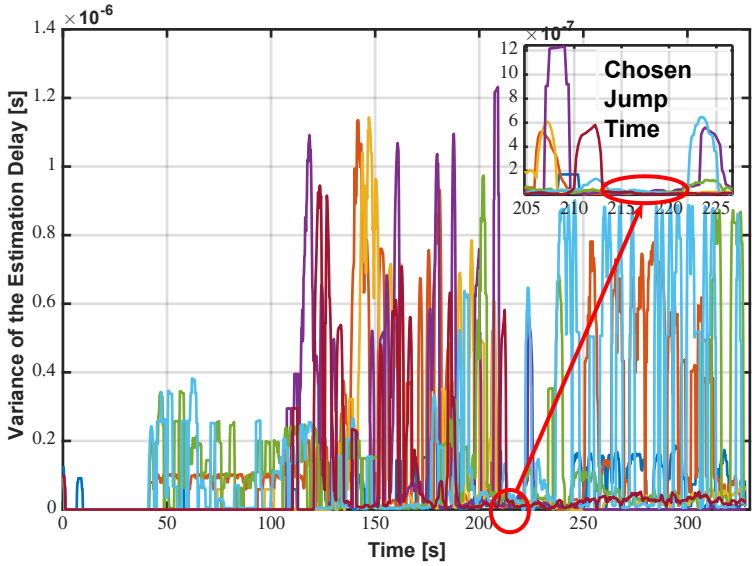

Fig. 5.8 Variance of the estimated delay for all visible channels. In the red circle it is highlighted the time instants chosen to jump because they have the lowest estimated variance

Fig. 5.8 we observe the chosen time instant where the variance of the delay estimation of each channel is below γ_σ. Observing Fig. 5.7 in that time instant, we see that the delay estimations of the satellite signals are greater than 0.5 μs.

Once the checks (5.4) are positive, the absolute delay of the DLL is modified by $\hat{\tau}$, in order to unlock the signal from the spoofer and lock it into the authentic signal.

5.4.3 Post-Jump Checks

After the jump has been performed, we need to check if the DLL is tracking the satellite signal. We check the value of $\hat{\tau}$ and we check the behaviour of the tracking loop, observing the correlators. We define three possible outcomes for each satellite and they are shown in Fig. 5.9:

- *Successful jump* (red line of Fig. 5.9). In this case, the jump successfully unlocks the signal from the spoofer and ends up locked into the authentic signal. A change in the sign of $\hat{\tau}$ is observed, meaning that the DLL

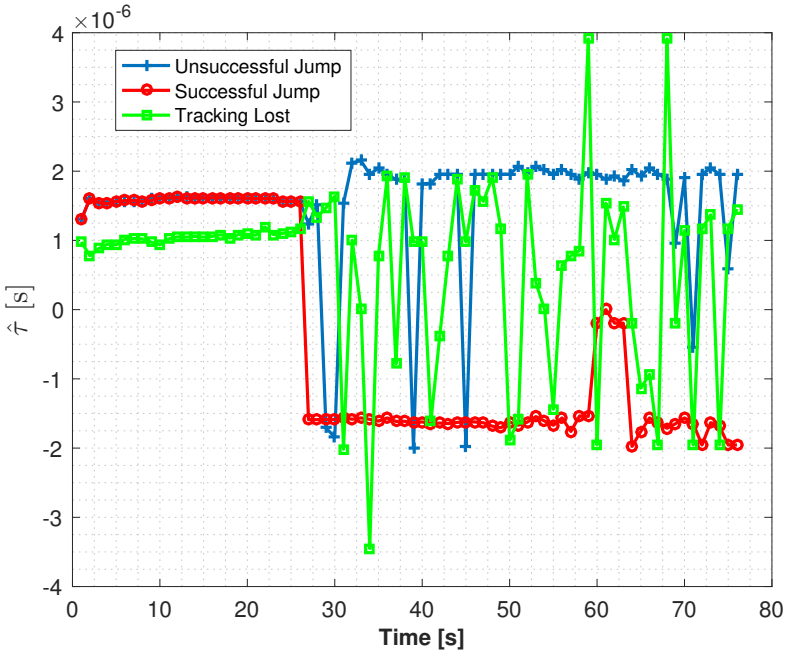

Fig. 5.9 Delay Estimation of three possible outcomes after the Jump (at second 26): loss of lock (green), successful jump (red) and unsuccessful jump (blue)

successfully jumped from one peak to the other. Also, the correlator level will be above zero, indicating that a signal is being tracked.

- *Unsuccessful jump* (blue line of Fig. 5.9). In this case, the jump unlocks the signal of the spoofer for a limited time, but it comes back and lock itself to the spoofer again. In this scenario, $\hat{\tau}$ does not change signs and it maintains a similar value before and after the jump. Also the correlator levels indicate that a signal is being tracked.

- *Loss of lock* (green line of Fig. 5.9). In this case, the jump moves the DLL to a point where there is no signal and it is not able to go back to any peak. In this scenario the correlator levels are very low indicating that no signal is being tracked and $\hat{\tau}$ randomly wanders. When this occur, the channel should go back to acquisition stage and restart the process.

5.5 Results

As previously discussed, the TJ algorithm aims at detecting spoofing attacks and providing continuous use of GNSS signals in the receiver. It also has the scope of mitigating the effects of these attacks by means of a delay jump.

In order to asses the TJ algorithm performance we use the TEXBAT datasets [84]. From the different datasets available in the testbed we focus on the scenario number 6 (ds6), which consists on a Dynamic Matched-Power Position Push. The dynamic scenarios of the TEXBAT are based on a clean road dataset recorded at Austin, TX to which it is added a spoofing signal on top in order to deviate the course taken from the real course of the vehicle. We believe that this is a good example of a typical vehicular application.

We also present results of a static case, the scenario ds4, a similar scenario to ds6 but based on a static clean dataset. These results show the working capabilities of the TJ algorithm, in both dynamic and static cases.

For each scenario, four cases were studied in order to highlight the overall working procedure:

- Case 1 is the clean solution obtained using a generic GNSS software receiver and where no spoofing attack was present.
- Case 2 is the solution obtained with the generic software receiver for the spoofing attack scenario.
- Case 3 is a solution using only the jumping procedure together with a classical PVT computation based on a KF using code and Doppler measurements.
- Case 4 is the solution using the TJ algorithm, i.e. jumping procedure and the double choice KF.

Fig. 5.5 shows a comparison of the error of x, y and z compared to the case 1. For the case 2, we observe that the solution is driven away from the correct road, and large errors are introduced mainly in the z axis. For the case 3 the effects that the jump has in the overall solution are clearly visible, at time 270. We observe that after the jump, the solution comes back to the real path and the maximum errors are reduced with respect to the third case.

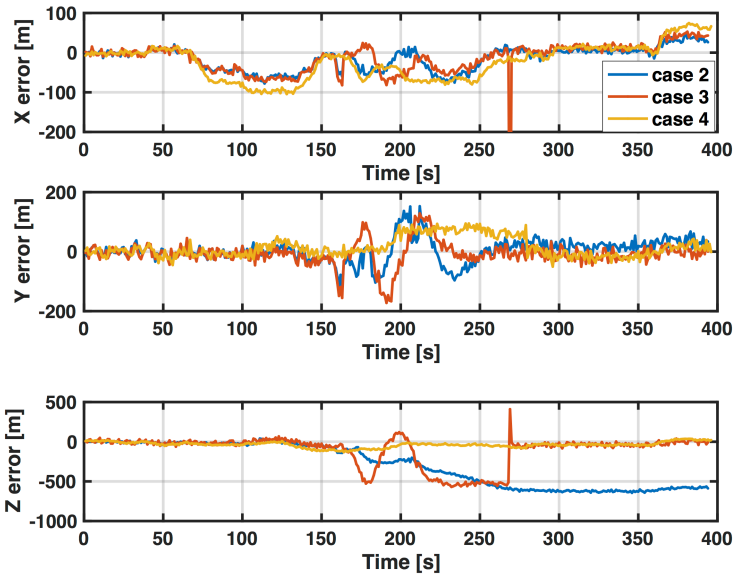

Fig. 5.10 x, y, z results for scenario ds6 with several configurations of the TJ algorithm. The blue line is the position error in case two. In orange the third case with only the Jump and in yellow the error when using the TJ algorithm.

Finally, we can observe how the complete TJ algorithm performs. The solution follows closely the real path and it is not controlled by the spoofer. In Fig. 5.11 the 2D tracks are presented for the four cases. It is possible to observe that using the TJ algorithm provides a continuity of unspoofed solutions, contrary to what it is observed for case 3, where the error increases considerably before the jump is feasible.

In this scenario from the six satellites available before the jump, five satellites performed a successful jump and one loss the lock, so it was excluded from the solution.

For the static case, ds4 scenario, results are presented in Figs. 5.5 and 5.13. We observe how in this scenario the KF is not working as well as in the dynamic scenario. The low dynamics of the scenario make the Doppler measurements less informative for PVT usage.

In the static case, from the six satellites available before the jump, four of them did a successful jump, one did an unsuccessful jump and one lost the lock, so the final PVT solution after the jump is performed with four satellites.

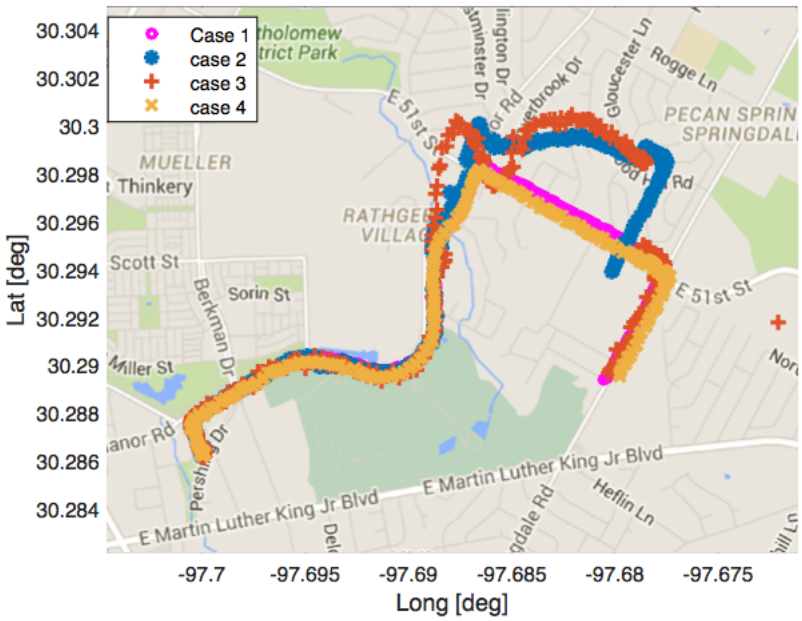

Fig. 5.11 The dynamic track of ds6 with several configurations of the TJ algorithm over map. The blue line is the real path of case 1, the orange line is the spoofed track of case 2. In yellow is depicted the path of case 3 and in purple the case 4 path, using the TJ algorithm

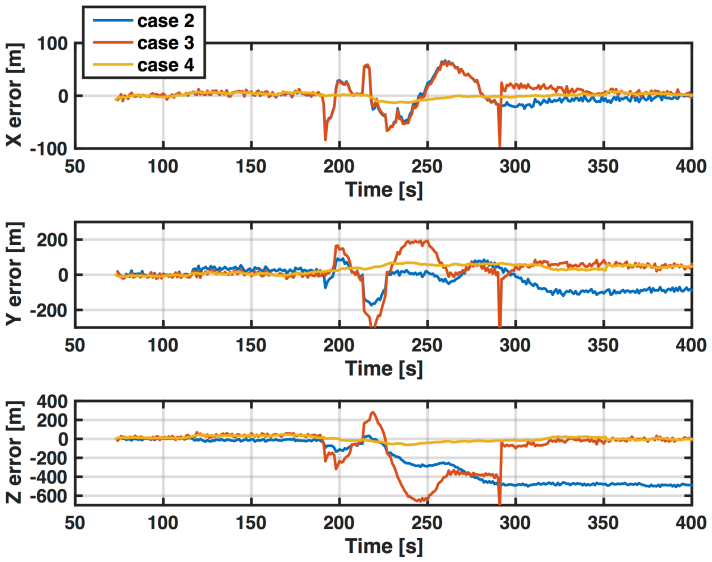

Fig. 5.12 x, y, z results for scenario ds4 with several configurations of the TJ algorithm. The blue line is the position error in case two. In orange is the error for case 3 with only the Jump. In yellow is the error of case 4, using the TJ algorithm

Nevertheless we observe how the errors decrease considerably when using TJ algorithm and the solution is reliable throughout the whole test.

In Table 5.1 we have several error measurements and it is possible to observe how the 3D Root Mean Square (RMS) error is reduced considerably between the different cases in both considered scenarios. If we compare cases 2 and 3, we observe how the jumping procedure alone, reduce the mean error in more than 55 % for the ds6 scenario and 40 % for scenario ds4. Comparing case 2 and 4, the TJ algorithm improves the mean and Standard Deviation (std) of 3D RMS error in more than 80 % for both scenarios. We observe how in case 2 we have the maximum error, but this is generated from the spikes generated by the jump, as can be observed in X, Y and Z directions in Figs. and .

5.6 Conclusions

In this work we presented the TJ algorithm, which is able to detect spoofing attacks and mitigate its effects in a GNSS receiver. Moreover, in parallel to these operations, the algorithm tries to guarantee the continuity and reliability

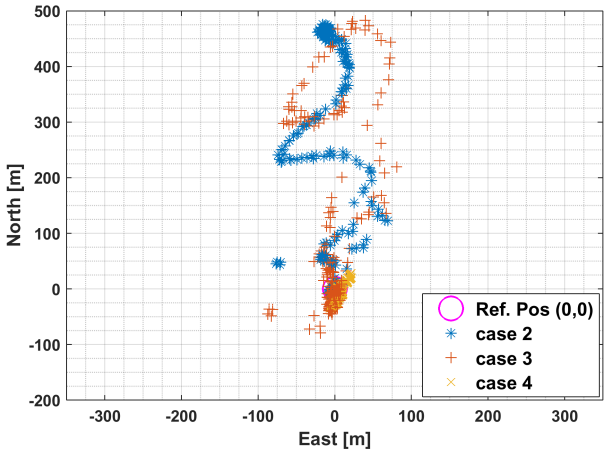

Fig. 5.13 The track of ds4 with several configurations of the TJ algorithm. The blue point is reference static position, the red ones indicates the spoofed track of case 2, in purple is depicted the path for case 3 and in green the path of case 4, using the TJ algorithm

	ds6			ds4		
3D RMS error	mean [m]	std [m]	max [m]	mean [m]	std [m]	max [m]
case 2	413	218	645	290	195	512
case 3	181	193	747	170	186	846
case 4	82	30	134	49	16	94

Table 5.1 Mean, standard deviation and maximum 3D RMS error in meters, for all 3 cases in scenarios ds6 and ds4.

of the system by means of a KF using only Doppler measurements. These Doppler measurements are more difficult to spoof, so more reliable during pseudorange-based attack.

The combination of several techniques like LASSO, KF and time jumping procedure at different levels, increases the complexity of the system, but allows to have a more robust receiver that is able to mitigate the negative effects of a spoofing attack, especially in vehicular applications. The working abilities of the TJ algorithm were demonstrated by means of real tests scenarios, both in static and dynamic, observing how the position error is considerably reduced.

The signal processing part, LASSO, SQI and BDE should be applied to both branches (I and Q) of the receiver, in order to take into account possibles attacks which use relative phase between LOS and spoofer to take control of the receiver while not changing delay or power of the real signal.

Chapter 6

Hybrid method for multipath-resiliant PVT determination using Kalman filter based algorithms

This chapter describes some experiments related to a method of integrity monitoring based on KF.The KF-based positioning, in urban environment, results generally affected by the MP, which is inevitable. The sequential nature of KF also generates in the positioning output a drift from the true trajectory when the navigation data is not clean enough. Therefore, a mechanism called LS fallback is proposed to mitigate the effect of MP on KF-based receiver. The idea of the method is to fallback to LS solution and reinitialize the KF, so reducing the drift and improve the accuracy of the results. This work has been done in collaboration with fellow PhD student, Hieu Trung Tran. His topic is related to environment models for integrity applications. We work together on developing and implementing the algorithms presented in this chapter.

The idea of this work is the analysis of the behaviour of the KF and the LS solution in a urban simulated environment in the presence of MP and a limited number of satellites in view. Here, the RAIM algorithm, in particular the Global test, is used for the detection of the outlier in the set of pseudoranges due to the MP environment. The objective of the comparison is to verify if

the KF-based RAIM can show higher sensitivity against MP than LS-based RAIM, which will be shown later in this chapter. Then an algorithm, called LS fallback, is proposed.

6.1 Introduction

PVT information is an essential element to develop and run services and applications in almost any field of science and technology. Consequently, over the past decades, the use of GNSS has become increasingly ubiquitous in almost any field of technology applications. At the same time the demand for higher accuracy has increased together with an interest in positioning solutions resilient to disturbances and interferences, which often are caused by the harsh environmental conditions in which GNSS receivers are used. Several factors can actually affect PVT accuracy: the miss-functioning of the satellites; different errors sources in the pseudorange determination (ionosphere, geometry, clocks, multipath, etc.) [3]; masking of the sky by the environment; etc. As for the environment, while problems can rise anywhere nonetheless the urban environment deserves special attention since it typically generates unfavorable conditions for a smooth PVT determination. In particular in urban environment the masking of consistent portions of the sky is a common feature that in some urban canyons can become very severe. Meanwhile the flat surfaces of buildings easily reflect GNSS signals generating consistent MP. Yet many applications and services are used in urban environment and improvement in performances in this environment would affect consistent amount of end users.

As for the PVT determination several algorithms and solutions have been developed and proposed, but they mainly refer to two basic schemes [3, 106, 107]: (i) the LS PVT determination which is a memoryless approach deriving the PVT information applying the least square algorithm to the pseudoranges between satellites and receiver; (ii) the KF approach that processes the pseudoranges between satellites and receiver with a KF. While LS based PVT output is relatively noisy, the more sophisticated KF approach provides a smoother output. On top of this it allows to integrate the GNSS PVT information together with other sensors like Inertial Measurement Units (IMU) which are becoming more and more common even in mass-market devices. However KF

is more prone to MP interference that easily causes drifts in the output of the filter that keeps some memory of the past.

In literature, the MP is faced in different ways. MP can be dealt with integrating other sensors, providing extra information as in [108], or detecting it at signal processing level; in this case several metrics based on correlation measurements are proposed in literature [44, 45, 58] or in the previous chapters of this thesis. In [109] some comparisons among different methods are presented. In addition, many mitigation techniques are proposed to limit the disturbance [20, 110] and several other works evaluate the impact of MP on the receiver in different environments [47, 53, 111].

In order to mitigate the possible drifts related to MP when using KF based algorithms, two solutions have been developed. They consist in shifting to LS based PVT determination when the presence of MP is recognized. The two solutions differentiate from each other for the test that is used to identify the presence of MP. One of the two tests is actually structurally equal to a test used in some Fault Detection (FD) algorithms. In fact MP is one of the several causes that can induce GNSS receiver malfunctioning.

Since FD in GNSS technology has been widely addressed and several solutions have been suggested to identify faulty systems [38], considering that MP can be a source of faulty behaviors, a comparison of the behavior of the proposed algorithms for MP occurrence recognition with some indicators used for FD has also been performed.

6.1.1 Kalman Filter

A classical approach, which is commonly adopted in GNSS receivers, consists in implementing a KF to compute the receiver position vector $\boldsymbol{u}_k$. In designing GNSS receivers, different KF solutions have been implemented and are described in the literature. Sometimes the filter has been used to integrate inertial sensors with the GNSS receiver [112], while in other studies it has been integrated directly in the tracking part of the receiver implementing the vector tracking loop architecture [113]. The KF architecture implemented is quite common and foresees the use of a filter state vector $\boldsymbol{x}_k$ with 8 states that are the receiver position coordinates and the clock bias together with their derivatives

(velocities and clock drift) so that $\boldsymbol{x}_k = [\boldsymbol{u}_k, \dot{\boldsymbol{u}}_k]^T$. The interested reader can refer to [3, 106, 112] for more details. The notation used for the filter description at epoch t_k is:

- $\mathbf{x}_k \in \mathbb{R}^8$ is the process state vector
- $\mathbf{\Phi}_k \in \mathbb{R}^{8\times 8}$ is the state transition matrix relating $\mathbf{x}_k$ to $\mathbf{x}_{k+1}$
- $\mathbf{w}_k \in \mathbb{R}^8$ is the process noise vector, assumed to be a white sequence with known covariance matrix $\mathbf{Q}_k$
- $\mathbf{z}_k \in \mathbb{R}^{2N_{sat}}$ is the measurement vector containing the pseudorange and Doppler measurement for each satellite.
- $\mathbf{H}_k \in \mathbb{R}^{2N_{sat}\times 8}$ is the matrix giving the ideal connection between the measurement and the state vector
- $\mathbf{v}_k \in \mathbb{R}^{2N_{sat}}$ is the measurement error vector, which is assumed white with known covariance $\mathbf{R}_k$ and zero crosscorrelation with $\mathbf{w}_k$.
- $\mathbf{R}_k$ is the covariance matrix of $\mathbf{v}_k$, it is assumed to be diagonal and it is derived according to the model in [71].

In the KF the state estimate $\hat{\mathbf{x}}_k$ of $\mathbf{x}_k$ is given by:

$$\hat{\mathbf{x}}_k = \hat{\mathbf{x}}_k^- + \mathbf{K}_k(\mathbf{z}_k - \mathbf{H}_k\hat{\mathbf{x}}_k^-) \tag{6.1}$$

where $\hat{\mathbf{x}}_\mathbf{k}^-$ is the predicted state vector for epoch k, propagated from previous epoch $\hat{\mathbf{x}}_k^- = \mathbf{\Phi}_{k-1}\hat{\mathbf{x}}_{k-1}$,

The connection matrix $\mathbf{H}_k \in \mathbb{R}^{2N_{sat}\times 8}$ relating states to measurements is given by:

$$\mathbf{H}_k = \begin{bmatrix} \mathbf{h}_{x,y,z} & \mathbf{1} & \mathbf{0} & \mathbf{0} \\ \mathbf{0} & \mathbf{0} & \mathbf{h}_{x,y,z} & \mathbf{1} \end{bmatrix} \tag{6.2}$$

where each row of $\mathbf{h}_{x,y,z} \in \mathbb{R}^{N_{sat}\times 3}$ is the unit vector pointing from the linearization point to the location of each satellite [106].

Finally, Kalman Gain $\mathbf{K}_k$ is computed as:

$$\mathbf{K}_k = \mathbf{P}_k^- \mathbf{H}_k^T (\mathbf{H}_k \mathbf{P}_k^- \mathbf{H}_k^T + \mathbf{R}_k)^{-1} \tag{6.3}$$

where $\mathbf{P}_k^-$ is the predicted (a priori) error covariance update at epoch k. $\mathbf{P}_k^-$ is defined as:

$$\mathbf{P}_k^- = \mathbf{\Phi}_{k-1} \mathbf{P}_{k-1} \mathbf{\Phi}_{k-1}^T + \mathbf{Q}_{k-1} \tag{6.4}$$

and $\mathbf{P}_{k-1}$ is the a posteriori error covariance update:

$$\mathbf{P}_{k-1} = (\mathbf{I} - \mathbf{K}_{k-1} \mathbf{H}_{k-1}) \mathbf{P}_{k-1}^- \tag{6.5}$$

To initialize $\mathbf{P}_k$ at $k = 1$ when there is no information on the error covariance, $\mathbf{P}_k$ can be assumed to be diagonal with large values [114].

Since $\boldsymbol{x}_k = [\boldsymbol{u}_k, \dot{\boldsymbol{u}}_k]^T$, the state transition matrix $\mathbf{\Phi}_k$ of the KF is:

$$\mathbf{\Phi}_k = \begin{bmatrix} 1 & 0 & 0 & 0 & \Delta t & 0 & 0 & 0 \\ 0 & 1 & 0 & 0 & 0 & \Delta t & 0 & 0 \\ 0 & 0 & 1 & 0 & 0 & 0 & \Delta t & 0 \\ 0 & 0 & 0 & 1 & 0 & 0 & 0 & \Delta t \\ 0 & 0 & 0 & 0 & 1 & 0 & 0 & 0 \\ 0 & 0 & 0 & 0 & 0 & 1 & 0 & 0 \\ 0 & 0 & 0 & 0 & 0 & 0 & 1 & 0 \\ 0 & 0 & 0 & 0 & 0 & 0 & 0 & 1 \end{bmatrix} \tag{6.6}$$

in which Δt is the time interval between epochs. In this work the position is calculated every second, thus $\Delta t = 1$ s.

The measurement error covariance matrix $\boldsymbol{R}_k \in \mathbb{R}^{2N_{sat} \times 2N_{sat}}$ is usually written as:

$$\boldsymbol{R}_k = \begin{bmatrix} \mathbf{\Sigma}_k & \mathbf{0} \\ \mathbf{0} & \dot{\mathbf{\Sigma}}_k \end{bmatrix} \tag{6.7}$$

where $\mathbf{\Sigma} \in \mathbb{R}^{N_{sat} \times N_{sat}}$ is a diagonal matrix, whose diagonal elements are the pseudorange error variances, while $\dot{\mathbf{\Sigma}}$ is a diagonal matrix containing the variances related to derivatives of pseudoranges.

Different solutions have been suggested in literature to assign numerical values to these variances. The interested reader can refer to [115] for more

Environment	$a(m^2)$	$b(m^2Hz)$	$\dot{a}(m^2/s^2)$	$\dot{b}(m^2Hz/s^2)$
Lightly degraded	10	150^2	0.01	25
Heavily degraded	500	10^6	0.001	40

Table 6.1 Example values for measurement error variance model

insight on some of them. Here the solution adopted is the one described in [116]. With it the diagonal elements of $\mathbf{\Sigma}$ and $\dot{\mathbf{\Sigma}}$ are defined as:

$$\mathbf{\Sigma}_{i,i} = a + b \cdot 10^{\frac{-C/N_{0,i}}{10}} \tag{6.8a}$$

$$\dot{\mathbf{\Sigma}}_{i,i} = \dot{a} + \dot{b} \cdot 10^{\frac{-C/N_{0,i}}{10}} \tag{6.8b}$$

where $C/N_{0,i}$ is the carrier-to-noise ratio of the signal from the i-th satellite which is time dependent, a, b, $\dot{a}$ and $\dot{b}$ are coefficients whose values depend on the assumed environment. Some examples of these coefficients are reported in Table 6.1 [116].

PVT determination applying KF is much smoother and less noisy than the one obtained with LS. This result depends on the fact that KF keeps some memory of the past and does not preform a memory-less one shot computation of the position at each epoch t_k. However, while KF is not much sensitive to random noise, it is more sensitive to biased disturbances that can introduce drifts on the PVT determination and can propagate them in time due to the memory of the filter.

6.2 Quality of PVT determination

In general GNSS applications degrade their performances when the PVT provided by the GNSS receiver is affected by increasing errors and uncertainties that can be particularly harming for safety-of-life critical applications. Remark that the quality of PVT determination, in terms of achieved accuracy, is generally time-varying since it depends on the quality of received signal, which is dependent on the satellite geometry, can be affected by disturbances (ionosphere and its scintillations, MP, etc.) as well as by miss functioning of some satellites. These facts have suggested the study of strategies [108] aiming at recognizing

possible degradation of the accuracy, rising alarms when the integrity of the PVT is negatively affected and looking for mitigation solutions that allow to correct, at least partially, the problem.

It is in this context that RAIM techniques have been elaborated to monitor the integrity of the navigation results [59]. The main goal of RAIM algorithms is to protect users from excessive errors in the navigation output [3], which may cause hazardous outcome if the faulty positions are used. Initially developed for use in aviation, they were classified as algorithms for Aircraft-Based Augmentation System (ABAS). They operate autonomously, using solely data from the receiver to work out the integrity assessment, without relying on external aids, assuming the presence of only one fault at the same time. The structure of RAIM algorithms consist of several features: Fault Detection (FD) mechanism to check the consistency of input measurements and detect possible faults, Exclusion (FDE) mechanism to identify faulty satellites to be excluded, Protection Level (PL) calculation to measure the availability of the navigation solution. Details about RAIM algorithm and its features can be found readily in literatures [59, 3, 70].

To identify degradation in the quality of PVT determination induced by a fault, FD algorithms check for the consistency of the measurements derived using a redundant satellite constellation. This is done running the so-called Global Test [70] (also known as range-residual test) that requires at least five satellites in view. The process of a FD algorithm comes from the statistical detection theory [59] and consists in verifying if a quantity (identified as *test statistic*) exceeds a given threshold. The threshold is chosen so that, in faultless conditions, the *test statistic* has a very low probability to pass it, thus ensuring very low false positive alarms. Faulty conditions instead, increase the values achieved by the *test statistic* that is no longer distributed as in faultless conditions and therefore more likely exceeds the threshold thus allowing for the recognition of the fault.

In literature three main FD algorithms are proposed for LS-based solutions [3, 38, 34] and presented in Chapter 2. On the other hand, FD algorithms for KF-based positioning method have also been recently proposed in [117, 111].

6.2.1 Global Test

When using LS for PVT determination the Global Test can be defined at each epoch k as:

$$\text{Global Test} = \begin{cases} H_0 : E\{\boldsymbol{\epsilon}_k\} = \mathbf{0}, Var\{\boldsymbol{\epsilon}_k\} = \boldsymbol{\Sigma}_k \text{ if } \tau_{global} < T_{global} \\ H_1 : E\{\boldsymbol{\epsilon}_k\} \neq \mathbf{0}, Var\{\boldsymbol{\epsilon}_k\} \neq \boldsymbol{\Sigma}_k \text{ if } \tau_{global} > T_{global} \end{cases} \tag{6.9}$$

where $\boldsymbol{\Sigma}_k$ is the covariance matrix of the pseudorange errors $\boldsymbol{\epsilon}_k$, which are assumed to be normally distributed, τ_{global} and T_{global} are the *test statistic* and detection threshold, respectively. In the residual method, τ_{global} is given by:

$$\tau_{global} = \hat{\boldsymbol{r}}_k^T \boldsymbol{\Sigma}_k^{-1} \hat{\boldsymbol{r}}_k \tag{6.10}$$

where $\hat{\mathbf{r}}_k = \bar{\boldsymbol{H}}_k \boldsymbol{\Delta}\hat{\boldsymbol{u}}_k - \boldsymbol{\Delta}\boldsymbol{\rho}_k$ is the residual between predicted and measured pseudoranges [69]. For Weighted LS (WLS) solution, $\hat{\mathbf{r}}$ is given by:

$$\hat{\mathbf{r}}_k = \bar{\boldsymbol{H}}_k \left(\bar{\boldsymbol{H}}_k^T \boldsymbol{\Sigma}_k^{-1} \bar{\boldsymbol{H}}_k \right)^{-1} \bar{\boldsymbol{H}}_k^T \boldsymbol{\Sigma}_k^{-1} \boldsymbol{\Delta}\boldsymbol{\rho}_k - \boldsymbol{\Delta}\boldsymbol{\rho}_k = -\boldsymbol{R}_k \boldsymbol{\Delta}\boldsymbol{\rho}_k \tag{6.11}$$

In faultless conditions the errors in $\boldsymbol{\epsilon}_k$ are normally distirubuted, thus τ_{global} (which is a sum-square of the errors) follows a central Chi-square distribution with $N_{sat} - p$ DOF, where p is the number of parameters to be estimated, that in our case is 4.

The threshold T_{global}, against which the *test statistic* must be compared, is obtained arbitrarily fixing the probability of false alarm P_{fa} that is perceived acceptable for the faulty free condition. It results that

$$P_{fa} = \int_{T_{global}}^{\infty} f_{\chi^2}(x; N_{sat} - p) dx \tag{6.12}$$

where $f_{\chi^2}(x; K)$ is the central Chi-square probability density function (pdf) with K DOF.

T_{global} can then be derived as [34]:

$$T_{global} = Q_{\chi^2}(1 - P_{fa}, N_{sat} - p) \tag{6.13}$$

where $Q_{\chi^2}(P,K)$ is the quantile function of the probability P of central Chi-square distribution with K degree-of-freedom, while P_{fa} is the probability of false alarm.

Note that τ_{global} and T_{global} depend on the number N_{sat} of available satellites, therefore in general they are function of the epoch k. This dependence has been however omitted in the notation for sake of simplicity, also because no change usually occurs on short time horizon of few minutes.

6.2.2 Kalman filter FD test

When the KF is used for PVT determination it is also possible to monitor the integrity of the achieved results with a consistency test [117] which is conceptually identical to the Global Test previously discussed for the LS PVT determination. In this case the *test statistic* τ_{KF} can be derived from the innovation vector $\hat{\mathbf{d}}_k^T$ of the KF process at the k-th epoch, which can be computed as

$$\hat{\mathbf{d}}_k^T = \boldsymbol{z}_k - \boldsymbol{H}_k \hat{\boldsymbol{x}}_k^- \tag{6.14}$$

while $\mathbf{S}_k$ is the innovation vector covariance matrix, which can be calculated as

$$\mathbf{S}_k = \boldsymbol{H}_k \boldsymbol{P}_k^- \boldsymbol{H}_k^T + \boldsymbol{R}_k \tag{6.15}$$

The *test statistic* τ_{KF} according to [117, 111] is then:

$$\tau_{KF} = \hat{\mathbf{d}}_k^T \boldsymbol{S}_k^{-1} \hat{\boldsymbol{d}}_k \tag{6.16}$$

The consistency test for KF is then defined as [117]:

$$\text{Global Test} = \begin{cases} H_0 : E\left\{\hat{\boldsymbol{d}}_k\right\} = \mathbf{0}, Var\left\{\hat{\boldsymbol{d}}_k\right\} = \boldsymbol{S}_k \text{ if } \tau_{KF} < T_{KF} \\ H_1 : E\left\{\hat{\boldsymbol{d}}_k\right\} \neq \mathbf{0} \text{ or } Var\left\{\hat{\boldsymbol{d}}_k\right\} \neq \boldsymbol{S}_k \text{ if } \tau_{KF} > T_{KF} \end{cases} \tag{6.17}$$

Since in faultless conditions τ_{KF} follows a central Chi-square distribution with $2N_{sat}$ degree-of-freedom (the length of $\boldsymbol{z}_k$) [117], the detection threshold T_{KF} is given by:

$$T_{KF} = Q_{\chi^2}(1 - P_{fa}, 2N_{sat}) \tag{6.18}$$

Remark that, also in this case, τ_{KF} and T_{KF} depend on the number N_{sat} of available satellites and therefore can vary in time. However this dependence is not accounted for in the notation, for sake of simplicity.

6.3 Least Square Fallback algorithms

When MP and possibly other disturbances introduce bias in the error of the PVT determination, such bias can cause drifts in the PVT computed using KF, since biased information is stored in the memory of the filter. It turns out that, while in disturbance-free conditions the KF approach, providing smoothed and accurate data, performs more satisfactorily than the much more noisy LS approach. When the satellite signals are affected by consistent biased error the one-shoot memoryless LS approach is indeed more noisy than the KF, but it is less affected by bias.

These considerations have motivated the creation of a new algorithm, presented in this chapter, called the Least Square Fallback algorithm that combines LS and KF PVT determination reinitializing the KF-based PVT computation using LS when MP degradation is taking place. The main goal of the algorithm is to achieve better positioning stability and accuracy under the effect of MP.

In order to decide when the received signal is degraded and the receiver should switch to LS, two solutions have been envisaged. The first one is based on the innovation computed in the KF, while the second one, which can be used when carrier smoothing is in use, is based on CS detection.

6.3.1 Innovation-based Fallback algorithm (IFB)

As for this first solution, it consists in performing a test formally identical to the Global Test for integrity using the innovation of the KF. In this test the only difference is the value chosen for the threshold T_{fb} against which the *test statistic* τ_{KF} must be compared. The reason for this lies in the fact that the detection of disturbances for integrity monitoring purposes needs to ensure very low false positive rates while accepting relatively large PVT error values.

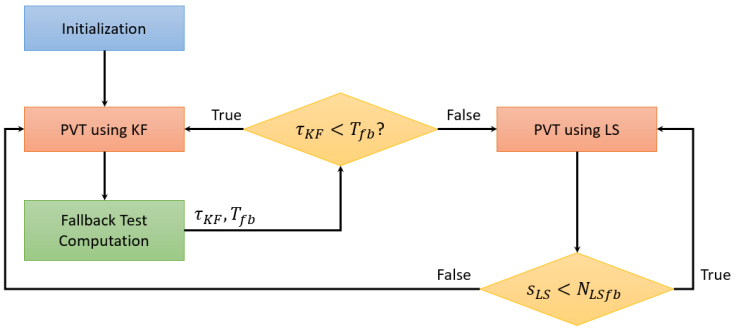

Fig. 6.1 Scheme of the IFB algorithm

On the contrary for the Fallback algorithm relatively high rates of false positive alarms are not critical, while it is important that possible drifts in the PVT, which are identified through an increase of the *test statistic* τ_{KF}, are promptly recognized.

The Fallback Test, to decide whether the receiver should switch to LS, is defined as:

$$\text{Fallback Test} = \begin{cases} H_0(\text{no disturbance}) : E\left\{\hat{\boldsymbol{d}}_k\right\} = \mathbf{0} \text{ if } \tau_{KF} < T_{fb} \\ H_{fb}(\text{presence of disturbances}) : E\left\{\hat{\boldsymbol{d}}_k\right\} \neq \mathbf{0} \text{ if } \tau_{KF} > T_{fb} \end{cases} \tag{6.19}$$

In other words, the Fallback Test assumes that the small degradation (such as MP) can drift the trajectory away from the correct path. When the presence of such degradation is recognized, the receiver switches to LS for N_{LSfb} steps. After running LS for N_{LSfb} steps the receiver switches back to KF again.

The Fallback threshold T_{fb} is derived in the same way as the consistency threshold T_{KF} of FD [70]. T_{fb} is derived from the probability of false alarm $P_{fa,fb}$ that is considered suitable for the fallback algorithm so that:

$$T_{fb} = Q_{\chi^2}(1 - P_{fa,fb}, 2N_{sat}) \tag{6.20}$$

To chose a suitable value for the probability of false alarm $P_{fa,fb}$, it is possible to make use of an experimentally derived ROC curve as better described in Section 6.5.2.

The overall scheme for the LS Fallback algorithm is depicted in Fig. 6.1, where s_{LS} is the counter of LS epochs after fallback decision. After initialization for KF (using LS), the process calculates the positions using KF, as with any normal KF implementation. After each epoch, the Fallback Test Computation block calculates τ_{KF} and T_{fb} following (6.16) and (6.20), using $P_{fa,fb}$, then proceed to the actual Fallback Test. If the test is passed, the next epoch will be processed using KF. Otherwise, the process will fallback to LS for N_{LSfb} steps counted by the counter s_{LS}. After N_{LSfb} steps in LS, the process returns to KF.

6.3.2 Cycle-slip-based fallback algorithm (CSFB)

As previously described, the carrier-smoothing algorithm, implemented with the Hatch Filter, needs to be reset if a CS occurs. To this extend a CS detector is needed. One of the possible detection strategies presented in literature [118] makes use of Doppler data to compute the quantity:

$$\tau_{CSD} = |\Delta\Phi| - \left| \frac{[D(t) - D(t-1)]}{2} dt \right|$$

where $\Delta\Phi$ is the phase variation, in number of cycles, between consecutive epochs, $D(t)$ is the Doppler measurement at epoch t, so that the term $\frac{[D(t)-D(t-1)]}{2} dt$ is the Doppler prediction. In general, the phase variation has to be in agreement with the Doppler prediction between epochs, otherwise a CS occurred.

To take a decision, the indicator τ_{CSD} is compared against a threshold T_{CS}. The Fallback Test, to decide whether the receiver should switch to LS, is defined as:

$$\text{Fallback Test} = \begin{cases} H_0(\text{no CS}): \text{ if } \tau_{CSD} < T_{CS} \\ H_{fb}(\text{presence of CS}): \text{ if } \tau_{CSD} > T_{CS} \end{cases} \tag{6.21}$$

Besides being used to reinitialize the Hatch filter, this test is used to trigger the Fallback algorithm. As for the determination of the threshold T_{CS}, its value can be heuristically derived. The value $T_{CS} = 6$ has been used in the experiments.

6.4 Input data sets

In order to test the properties and the quality of the proposed algorithms while examining them side by side with indicators of PVT performances three different data sets are used. Two of them are simulated data sets while the third is a real data set.

As for the simulated data sets, two tools were used for their generation. Simulated signals were generated using a modified version of the signal generator presented in [67]. This generator, which is developed in MATLAB, in its original version takes two sets of information as input: the nominal trajectory of the mobile receiver for which GNSS signals have to be generated (provided through a google-map-based interface) and the information of the available GNSS satellites for PVT determination (skyplot). As output the generator provides the signal to be fed to the receiver. In its original version the generator provides only MP-free outputs which are useless for the study of the algorithms presented in this paper. Therefore a modified version of the simulator was developed to allow for outputs affected by multipath that fit the needs of the analysis described hereafter. The modified version of the signal generator integrates, together with the above mentioned inputs, also the information characterizing the MP affecting GNSS signals. This last information is provided by a second tool, developed by the German Aerospace Center - DLR, named *Land Mobile Multipath Channel Model* [119] which has been standardized in ITU document [120]. This tool is based on a model which was developed starting from a real data measurement campaign aiming at investigating the way in which different environmental factors (buildings, trees, etc.) affect GNSS signals generating MP and degrading the quality of the signals received by a mobile receiver [119]. With the *Land Mobile Multipath Channel Model*, which is developed in MATLAB, it is possible to provide a nominal trajectory of the moving receiver and customize its surrounding environment including buildings, trees, light poles, etc. The tool is then able to generate MP delay rays and to provide parameters characterizing them. These parameters are fed to the modified version of the signal generator.

Both simulated data sets were generated with sampling frequency of 16.367 MHz, intermediate frequency of 4.123 MHz, using 5 bits for quantization. As for the available satellites the same configuration with 9 satellites was chosen

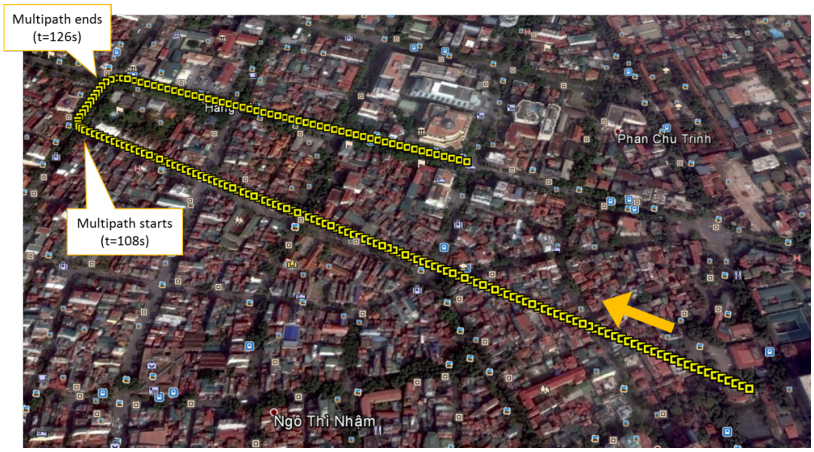

Fig. 6.2 Route of the scenario 1.

for both data sets. The corresponding skyplot is shown in Fig. 6.3. The C/N_0 of the satellites ranged from 37 to 42 dBHz. For the mutipath generation the MP model was setup in urban surrounding mode, with a road width of 15 m and both sides of the road populated with buildings (maximum height 25 m), trees and light posts. The simulated trajectories for both simulated data sets were generated starting from the map of Hanoi, Vietnam and they propose two different scenarios.

6.4.1 Scenario 1

This scenario, whose path is reported in Fig. 6.2 together with the indication of the direction of movement, simulates a vehicle moving at an average speed of 40 km/h along straight roads with only two ninety-degrees sharp curves. Generated data last for 3 minutes (180 seconds). MP affects the signal (on all satellites) from 108 s to 126 s, so that it starts before the first curve and ends before the second one.

6.4.2 Scenario 2

This scenario, whose path is reported in Fig. 6.4 together with the indication of the direction of movement, simulates a vehicle moving at an average speed of 40 km/h along a curved path in an urban environment. Also in this case generated data last for 3 minutes (180 seconds), but MP affects the signal (on

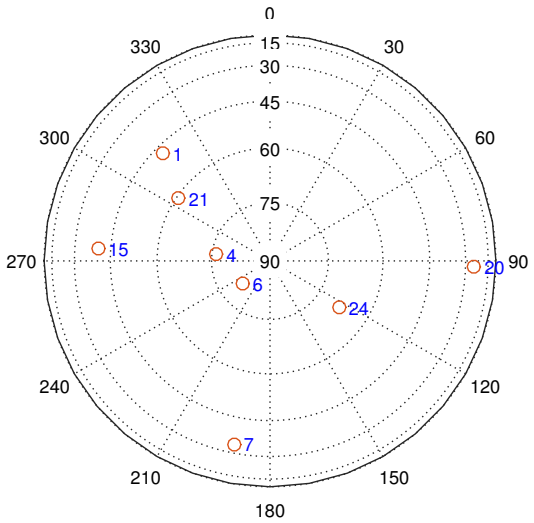

Fig. 6.3 Skyplot of the simulated scenarios.

all satellites) for a longer period: from 108 s to 156 s, that is 30 s longer than in scenario 1.

6.4.3 Real data set

The real data set was recorded on a car moving around the campus of the Polytechnic of Turin, Turin, Italy, using a Septentrio SSRC2 receiver. The path followed by the car for this data collection is reported in Fig. 6.5 where 'A' is the starting point. Data were collected for about 24 minutes. Over this time interval the number of available satellites varied from a maximum of 11 GPS satellites to even less than 4 at some epochs in which Non Line-of-Sight (NLOS) conditions were met thanks to the unfriendly urban environment in which the car was moving along a trajectory featuring sometimes segments with rather clear sky view, but other times segments with high buildings and flyovers which consistently degraded the signals even blocking the view of the sky at some epochs. The receiver had the carrier smoothing function enabled. Fig. 6.6 shows the skyplot with the available satellites at the beginning of the data collection.

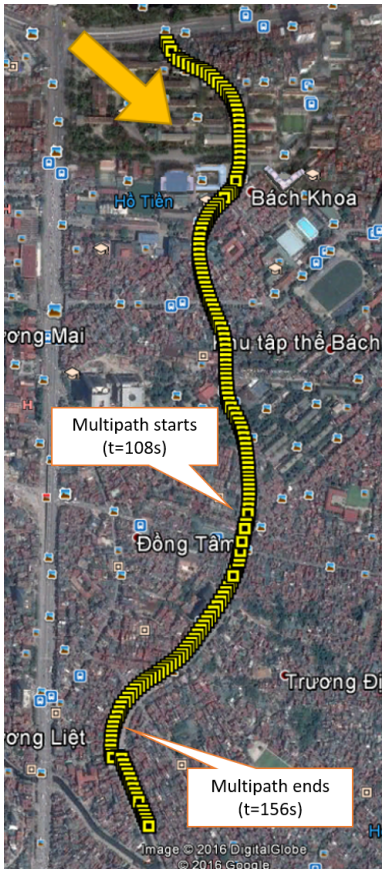

Fig. 6.4 Route of the scenario 2.

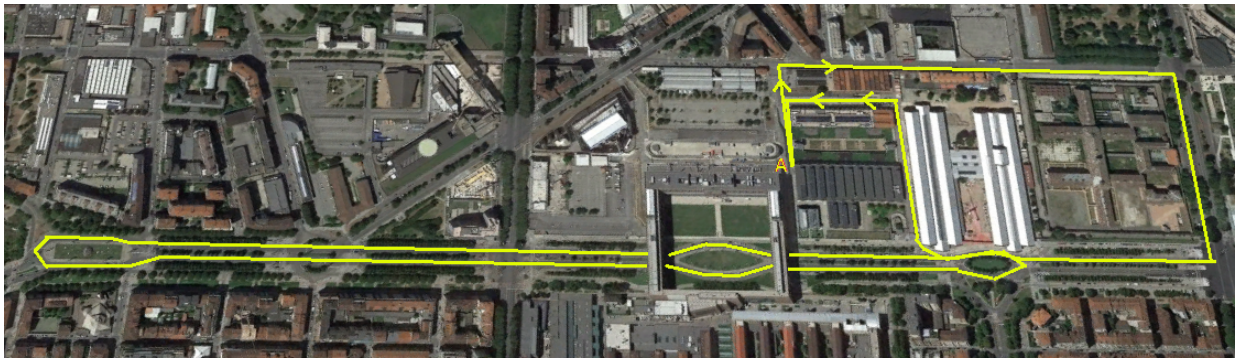

Fig. 6.5 Path of the real data collection starting from point A.

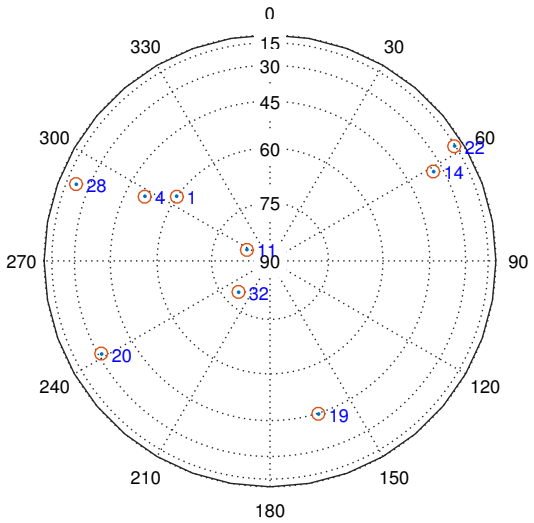

Fig. 6.6 Skyplot of the real data at the beginning of the data collection.

6.5 Performance analysis

The different simulated and measured row data sets were processed with in-house developed software receivers in order to evaluate the performances of different FD indicators and algorithms. The performances of the new PVT algorithms presented were also evaluated.

In the following paragraphs the obtained experimental results are presented and commented.

6.5.1 Fault detection and related indicators

A first analysis carried out with the simulated data consisted in examining the fault detection capability associated to the pseudorange residuals and to the innovation when using LS and KF respectively. Plots of these quantities were derived for two representative satellites (PRN[1] 1 and PRN 7) and are reported in Fig. 6.7, which is relative to scenario 1, and in Fig. 6.8, which is relative to scenario 2. The time interval in which the MP occurs is highlighted in the figures. From these figures it can bee seen that KF, with the innovation, is

[1]Pseudo-Random-Noise (PRN) code spreads the spectrum of the satellite signals and it is used to identify each satellite.

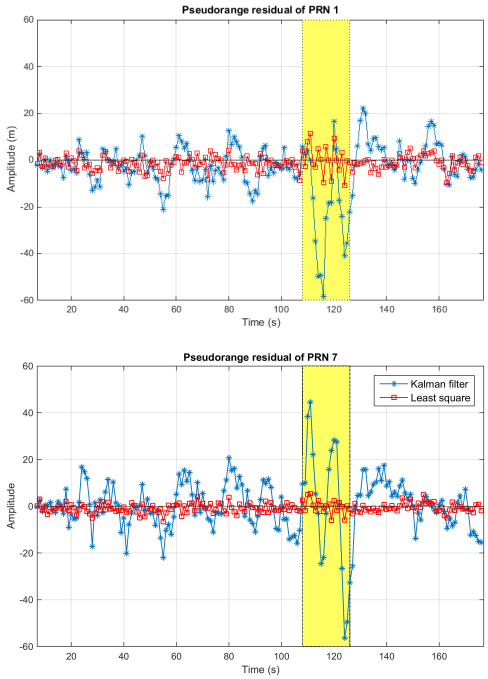

Fig. 6.7 Pseudorange residuals and innovation of satellites PRN 1 (a) and PRN 7 (b) in scenario 1 (MP occurs in the highlighted time window 108-126 s).

much more sensitive to the occurrence of MP. It can be also noted that the effect of MP on the innovation last longer than the MP itself.

The *test statistics* τ_{global} for LS and τ_{KF} for KF are shown in Fig. 6.9, which is relative to scenario 1, and Fig. 6.10, which is relative to scenario 2. From these figures it appears evident that MP does not affect much τ_{global} while it affects consistently τ_{KF} that results to be a very good indicator of MP presence.

It is worth noting that τ_{KF} has been proposed as integrity indicator for FD algorithms [117, 111]. Should such an algorithm be implemented while processing these data sets, assuming a probability of false alarm equal to $6.65 \cdot 10^{-5}$ (which is in the same order of magnitude of the value used in [121]) the resulting threshold would be 21.9 and τ_{KF} would pass it triggering the FDE algorithm. This could result in the exclusion of some satellites that would affect the PVT determination, as presented later.

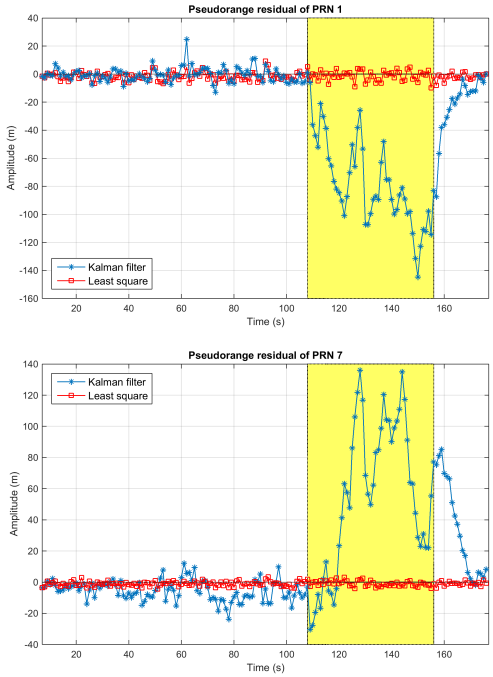

Fig. 6.8 Pseudorange residuals and innovation of satellites PRN 1 (a) and PRN 7 (b) in scenario 2 (MP occurs in the highlighted time window 108-156 s).

6.5.2 Derivation of the threshold T_{fb} for the Innovation-based Fallback (IFB) algorithm

As previously remarked while describing the IFB algorithm in Section 6.3, the threshold T_{fb} to be used to detect MP events should be determined from relation (6.20) properly choosing the probability of false alarm $P_{fa,fb}$.

In order to derive a reasonable value for this probability, the ROC curve relating the probability of detection P_d versus the probability of false alarm $P_{fa,fb}$ has been experimentally derived from the data relative to scenarios 1 and 2.

The derivation has been carried out by varying the values of the input probability of false alarm $P_{fa,fb}$ from 0 to 1, and evaluating, for each of them, the corresponding Fallback threshold T_{fb}(following (6.20)) and the probability of detection P_d. The probability of detection P_d is derived considering only the epochs that are within the intervals in which MP occurs. Such probability is estimated as the ratio between: (i) the number of epochs for which the *test*

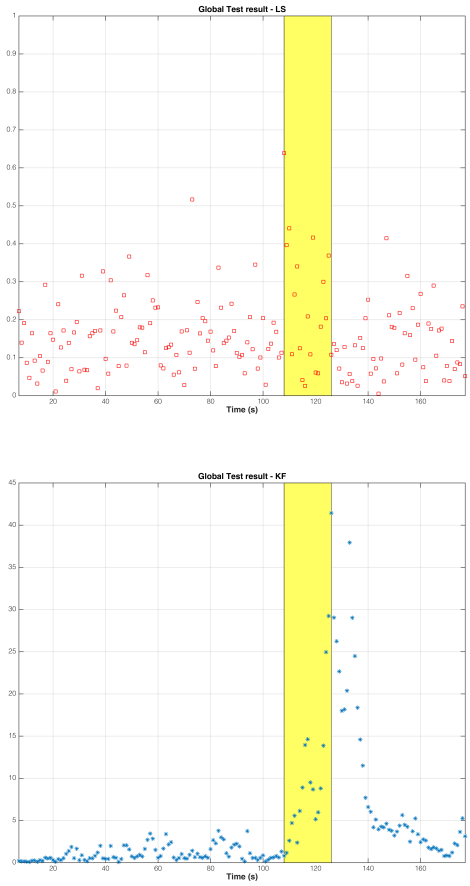

Fig. 6.9 *Test statistic* τ_{global} while using LS (a) and τ_{KF} while using KF (b) in scenario 1 (MP occurs in the highlighted time window 108-126 s).

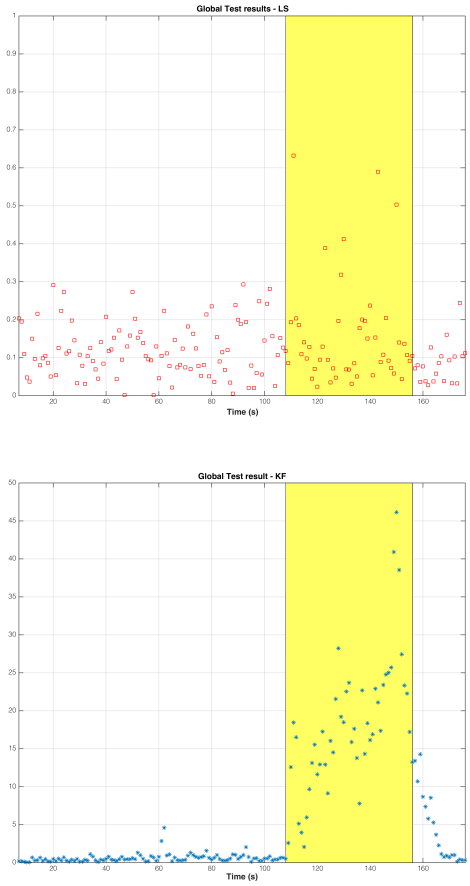

Fig. 6.10 *Test statistic* τ_{global} while using LS (a) and τ_{KF} while using KF (b) in scenario 2 (MP occurs in the highlighted time window 108-156 s).

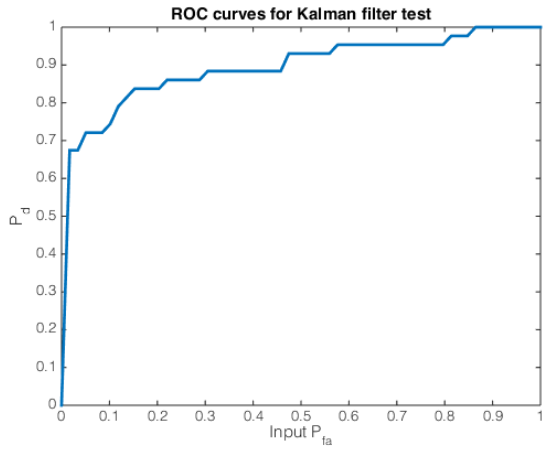

Fig. 6.11 ROC curve reporting the probability of detection P_d against the probability of false alarm P_{fa}.

statistic τ_{KF} is higher that the threshold, (ii) the total number of epochs in the intervals in which MP occurs.

In Fig. 6.11 the obtained ROC curve is depicted.

From this curve the value of 0.3 was chosen for the probability of false alarm $P_{fa,fb}$ to be used in relation (6.20) in order to compute the threshold T_{fb}. This threshold allows the *test statistic* τ_{KF} to detect almost all faults.

6.5.3 Positioning performances of the algorithms

Once the probability of false alarm $P_{fa,fb} = 0.3$ is chosen and the corresponding threshold T_{fb} is computed, it is possible to run the IFB algorithm and compare it with the LS and the KF algorithms. Only one more parameter is needed that is the number N_{LSfb} of epochs in which the PVT is computed using LS before switching back to KF. This number has been set equal to 5 s considering that in general MP last for a while so that it is useless to switch immediately back to KF. However it is not useful to keep too long the LS PVT evaluation in case MP ends, since KF performs better when no MP is present. Actually, if that is not the case, the algorithm will just switch back from KF to LS more times, but without causing any problem.

Using data of scenarios 1 and 2, the position has been deriveded using LS, KF and IFB algorithms. Since simulated data are used, the true path is exactly

known and the results obtained with the different algorithms can be easily compared with it.

In Fig. 6.12 the results relative to scenario 1 are reported. During the initial clean period with no MP, the path derived with KF algorithm, that coincides with the one of the IFB algorithm, is smooth and very close to the true one, while the path derived with LS is noisier. When the MP steps in, positions derived with KF derive away from the true path, while positions derived with LS are still noisy but closer to the true path. The IFB algorithm, switching from KF to LS takes advantage of this fact providing an overall more accurate solution. In Fig. 6.13 the part in which MP occurs is shown enlarged to allow a better comparison of the different results.

The different performances of the algorithms can be even better compared referring to Fig. 6.14 in which the horizontal positioning errors of the different algorithms are split into their East and North components. It can be noted that, when no MP is present, the KF algorithm (and consequently also the IFB algorithm) has in general lower error than the LS algorithm. Also the maximum error of KF is about 7 m compared with about 10 m of LS. On the contrary, when there is MP, KF derives and its error rises up to 20 m in East direction and 40 m in North direction, while LS (and consequently the IFB algorithm that in such conditions is associated to it) has more or less the same performances as in the MP-free time interval.

Results for scenario 2 are shown in Fig. 6.15 and Fig. 6.16. They are qualitatively similar to the ones of scenario 1 showing better performances of KF in MP-free time intervals while in MP-affected time intervals LS works definitely better. Consequently the IFB algorithm, which is switching from FK to LS when MP presence is recognized, takes the advantages of the two algorithms. Quantitatively, in scenario 2 the error of KF algorithm is consistently larger than in scenario 1. Actually in MP-affected time intervals the error rises up to 40 m in East direction and 160 m in North direction. It should also be noted that in scenario 2 the path is curved while in scenario 1 it has two sharp curves, but beside this it is along straight roads where in general KF performs better than along curved paths.

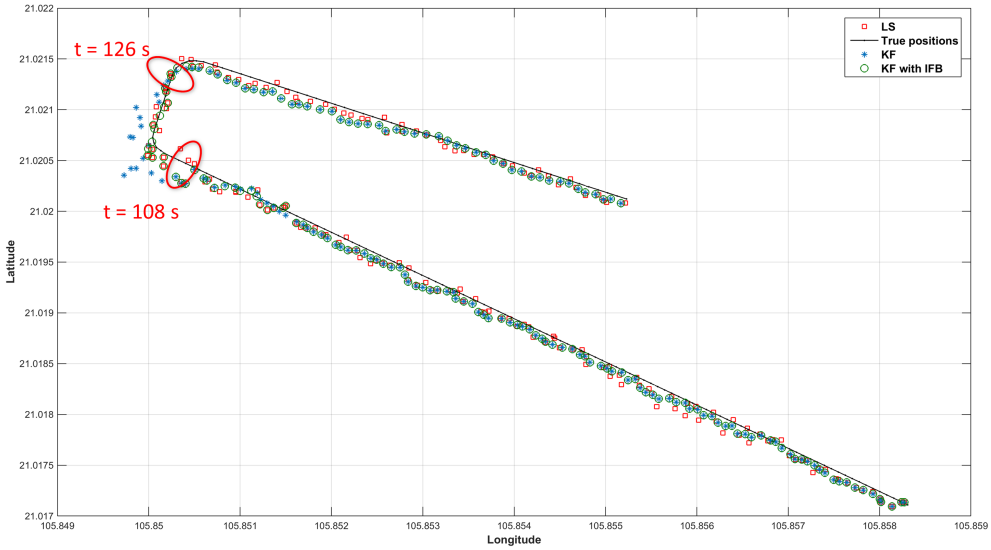

Fig. 6.12 Positioning results for scenario 1

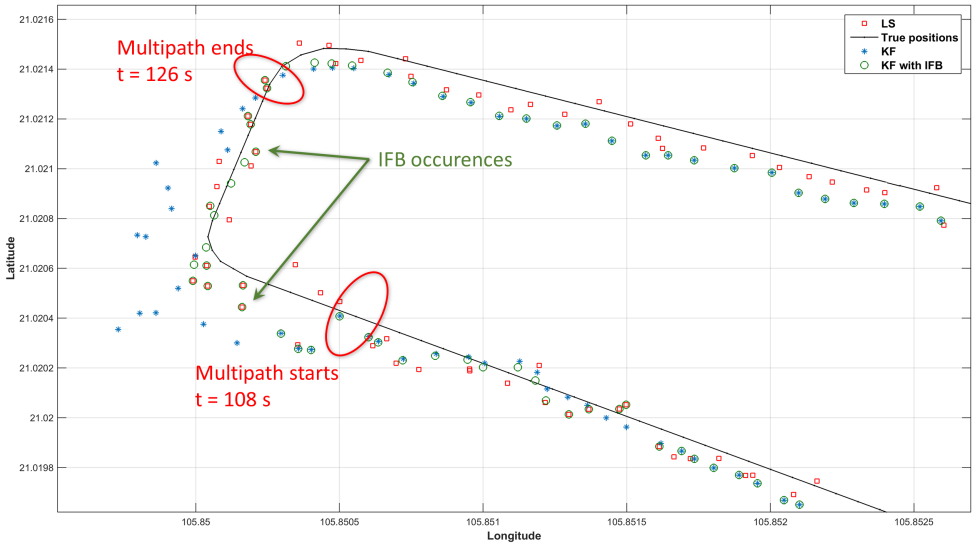

Fig. 6.13 Positioning results for scenario 1 - MP segment

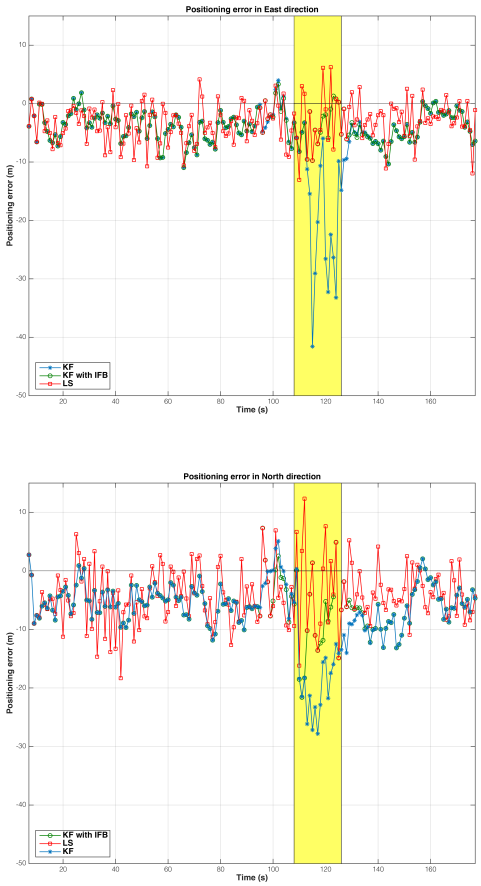

Fig. 6.14 Positioning error for scenario 1 in horizontal plane: (a) East direction, (b) North direction

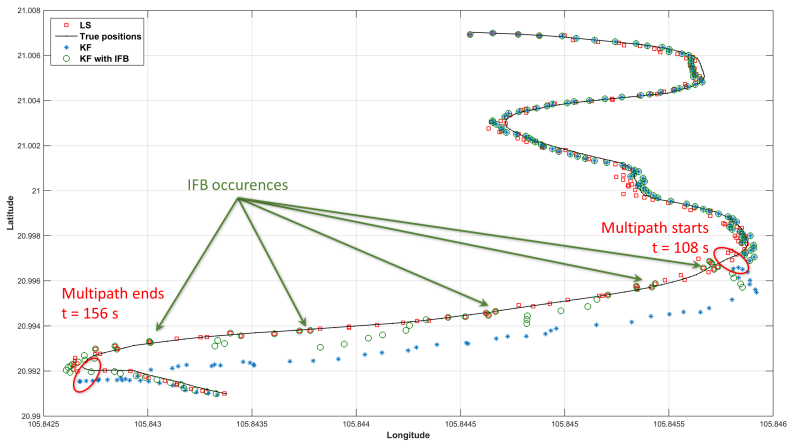

Fig. 6.15 Positioning results for scenario 2

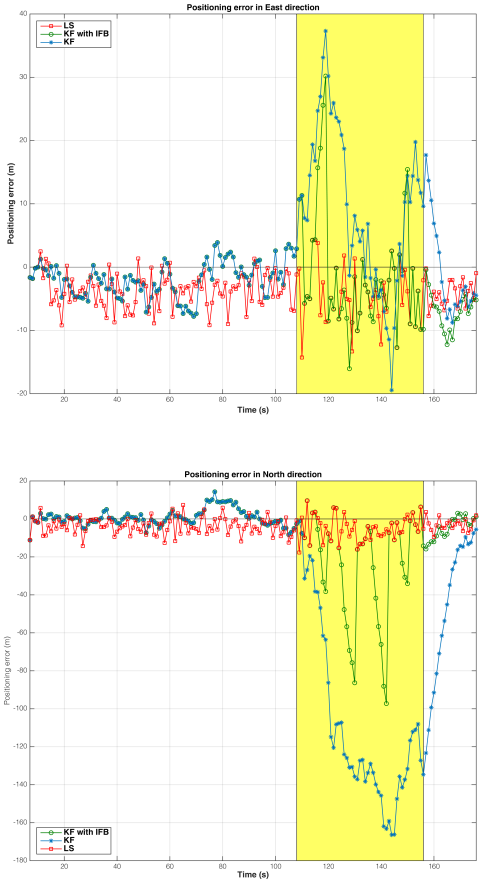

Fig. 6.16 Positioning error for scenario 2 in horizontal plane: (a) East direction, (b) North direction

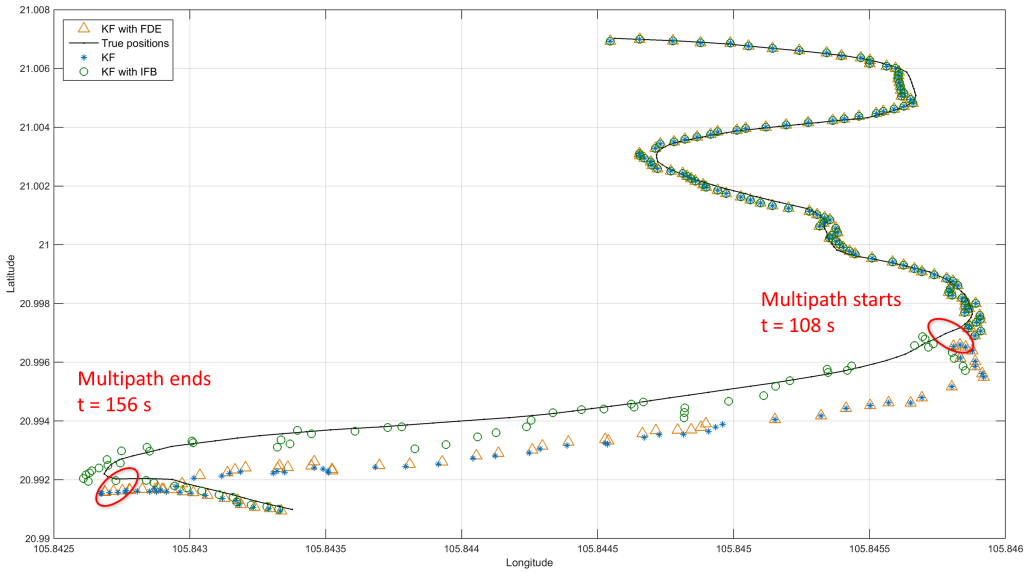

Fig. 6.17 Positioning results for scenario 2 with one satellite excluded

6.5.4 Positioning with satellite exclusion

As discussed before, the *test statistics* τ_{KF}, which is used in some FD algorithms to decide whether faulty conditions are present, is quite sensitive to MP events that could therefore easily trigger FDE algorithms implemented in the receiver (like in the case of some RAIM implementation). If this happens, the receiver does not use the pseudorange relative to the less reliable satellite to derive the PVT with the KF algorithm. While this strategy is implemented to get better PVT results in faulty conditions, when the FDE algorithm is triggered by MP the improvement in PVT determination can be missed as it is shown in Fig. 6.17, in which results of PVT determination using KF algorithms without any satellite exclusion and with the exclusion of one satellite is reported together with the PVT determination using the IFB algorithm and the true path. Results are relative to scenario 2 and show that KF algorithm with and without satellite exclusion provide almost the same outputs, which are less accurate than the IFB algorithm.

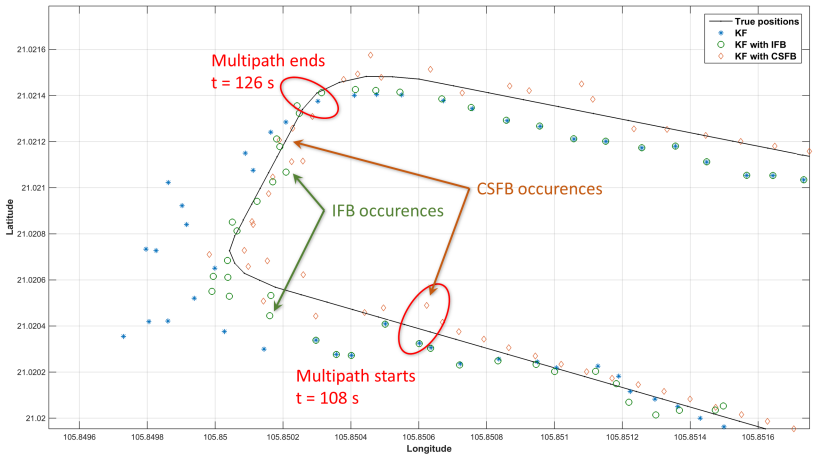

Fig. 6.18 Comparison on navigation solution in latitude and longitude for scenario 1 (MP in the time window 108 s to 126 s).

6.5.5 Carrier-smoothing and CS-fallback algorithm (CSFB) performances

The two simulated data sets of scenarios 1 and 2 were used also to test the performances of the CSFB algorithm. To this extent the length of the carrier smoothing filter was heuristically chosen $N_{HF} = 40$. Data were processed with a different software receiver, written in C language [122] and implementing carrier-smoothing. In order to perform the CSFB algorithm it is necessary to chose the detection threshold T_{CS}. Also this value has been heuristically derived as $T_{CS} = 6$.

In Fig. 6.18 navigation solutions are shown for scenario 1, using different methods: the KF without smoothed pseudoranges, the KF with CSFB algorithm and the KF with IFB algorithm.

In Fig. 6.19 similar results are shown for scenario 2, while in Fig. 6.20 the horizontal positioning errors of the different algorithms are split into their East and North components.

From these results it appears clearly that the CSFB algorithm has quite good performances. Actually it takes advantage of the smoothed input pseudoranges

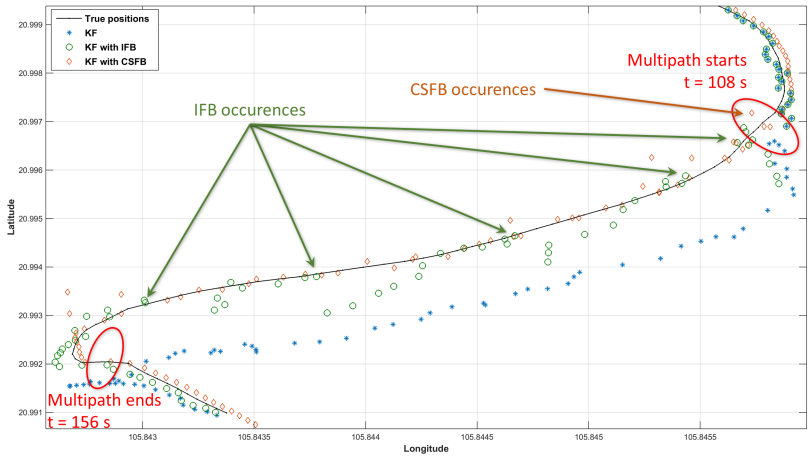

Fig. 6.19 Comparison on navigation solution in latitude and longitude for scenario 2 (MP in the time window 108 s to 156 s).

and, on top of this, with the Fallback mechanism it mitigates the MP effects on KF positioning algorithms.

6.5.6 Real data elaboration

The results relative to the real data set PVT determination are reported in Fig. 6.21. It is possible to observe the effect of the harsh environment in in which the presence of obstacles can cause errors misfitting the internal model of the KF. Such errors are propagated in time by the memory of the filter affecting the overall goodness of PVT. The LS fallback algorithm, instead, provides a reset for the KF whenever the *test statistic* τ_{KF} is over the threshold T_{fb}.

In Fig. 6.22 the *test statistics* τ_{global} for LS and τ_{KF} for KF are shown for the real data sets together with the threshold T_{KF} used by the CSFB these that however appears only when the KF solution is used. Note that this threshold varies in time since the number of available satellites is varying according to the varying masking angle induced on the receiver antenna by the urban environment.

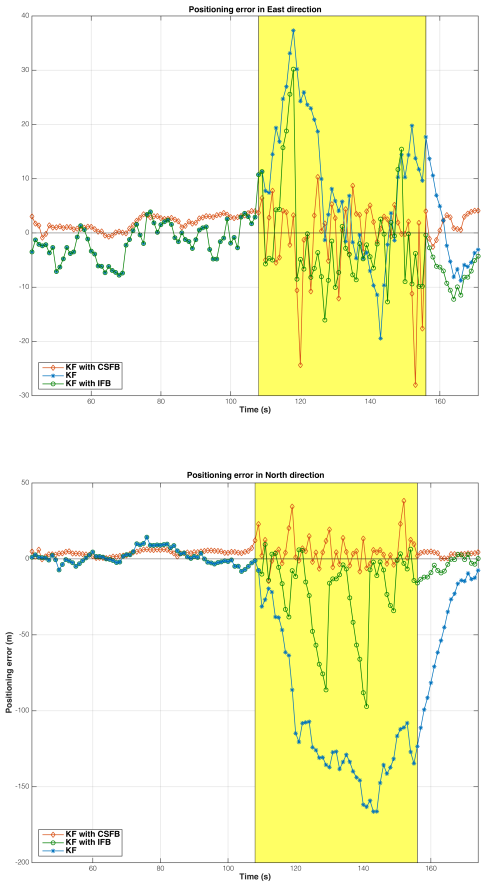

Fig. 6.20 Positioning error with carrier smoothing for scenario 2 in horizontal plane: (a) East direction, (b) North direction

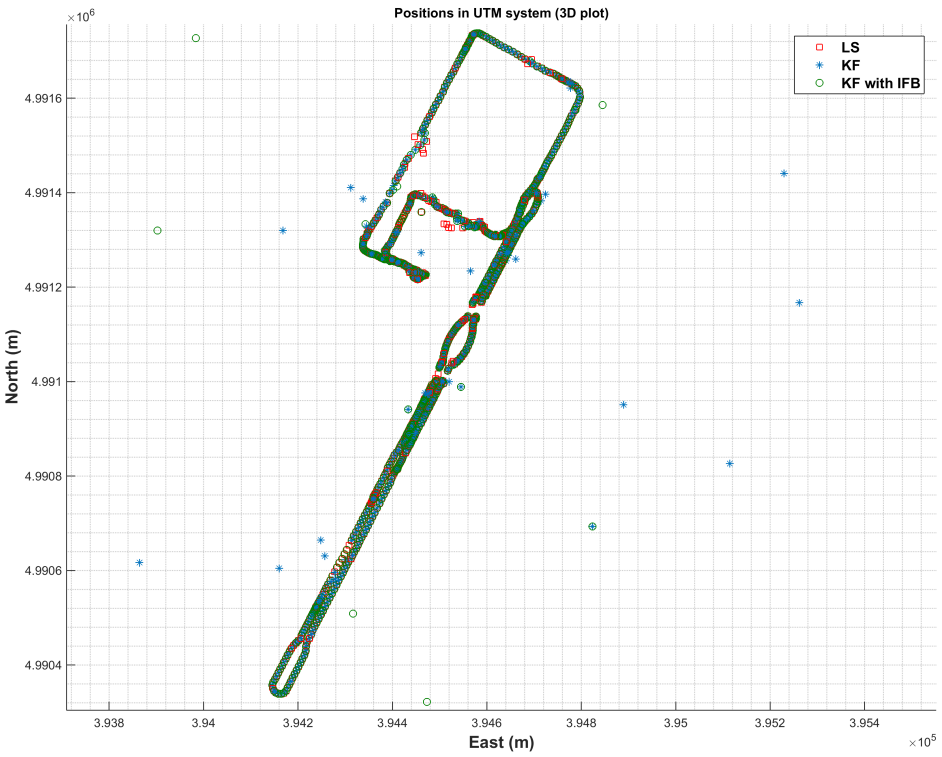

Fig. 6.21 Application of the fallback algorithm to real data.

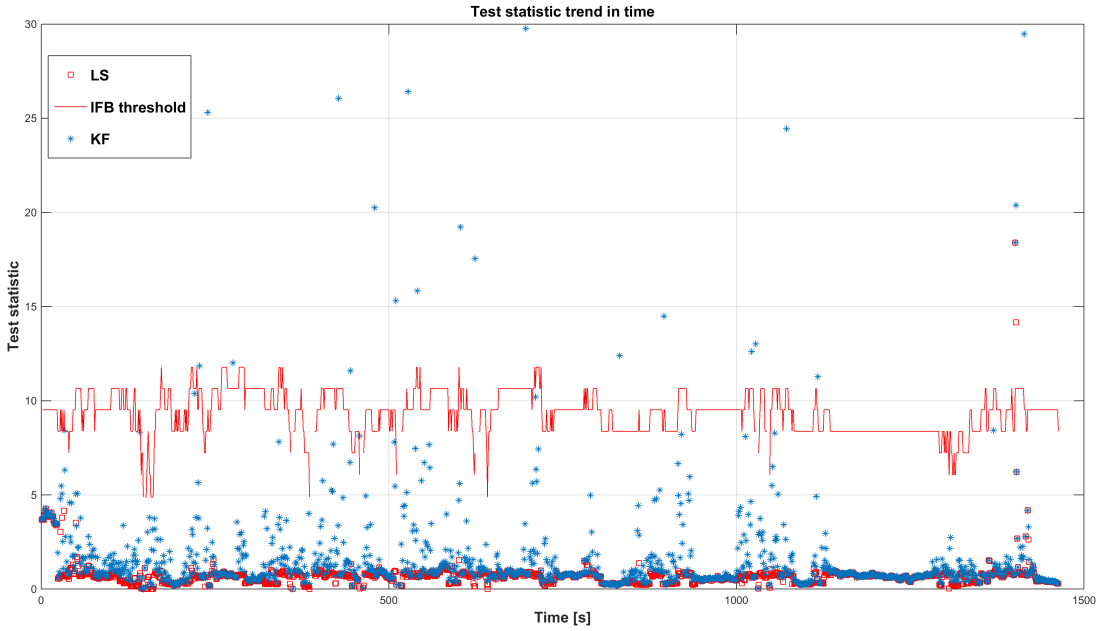

Fig. 6.22 *Test statistic* trend for KF, LS.

6.6 Conclusion

In this chapter we presented two version of a new algorithm aiming at getting MP-resiliant performances when using KF based algorithms for PVT determination. The algorithm mainly consists in switching from KF to LS whenever the presence of MP is detected. The two versions of the algorithm differentiate from each other in terms of the test that is used to identify the MP occurrence. One test is performed using a function derived from the innovation which is available when KF algorithms are used for PVT computation. This test is formally similar to a test proposed for FD but its different purpose impacts on the choice of threshold to be actually used. The second test is based on the CS detection when using carrier smoothing in pseudorange evaluation.

The performance of the proposed algorithm has been tested and compared with the performances of standard LS and KF algorithms. For these tests two simulated data sets and a real data set have been used. Besides, the performances of different indexes commonly used in FD algorithms have also

been computed for the same set of data in order to verify their suitability to identify the occurrence of MP.

The obtained results show that the proposed algorithm performs satisfactorily allowing to combine advantages of KF algorithms, which perform better in the absence of MP, with the advantages of LS, which performs better in MP-affected time intervals.

Conclusions

In this thesis, we discussed about techniques to use against impairments in order to detect it. These techniques use information coming from tracking loops of the receiver. Then, an index to assess the quality of the received signals was presented and used in multipath and spoofing scenarios. The quality index can be used to exclude or to inflate the variance of the pseudorange measurements.

An application of the MP detection algorithm is, for instance, for the reference stations to monitor the environmental changes around the GNSS receiver. A possible situation for reference ground stations and information about these changes are taken from [123]. We suppose a station with an antenna mounted at a certain height from the ground, that is considered as a planar surface. The surface layer around the antenna may change, for example, in case of soil moisture. In fact the reflection coefficient of the soil changes if it is dry or wet and it depends on the elevation angle of the incoming signal and also depends on the polarization of the signal. GPS signal is transmitted with Right Hand Circularly Polarized (RHCP), but the reflections from surfaces could rotate and transform in Left Hand Circularly Polarized (LHCP) or contain both polarizations. An alteration of the reflection coefficient due to rain or to other climatic events may be an additional MP source, also in case the receiver is apparently protected from it.

The last part is dedicated to algorithms devoted to mitigate the effect of multipath by using an hybrid method composed by KF and LS solution. All of these methods are validated by using simulated and real data.

Chapter 3 presented the multipath detector called MPDD. The detector is implemented in a software receiver. Some qualitative comparisons are given between the LAF theory used and the well known MEDLL technique presented

in literature. Then, the structure of the detector is introduced, which is a novel contribution. Then to increase the performance of the detector, in terms of reduction of P_{fa}, the LS problem was modified and a new minimization problem to solve was provided.

The feasibility of a MP detector based on signal processing techniques is possible but its capabilities are limited by the presence of noise. It is important to tune detector's parameters (LAF length, dictionary entries, $mathbfU$ matrix containing the basis signals). Then, another problem to take into account is the of the front-end. The algorithm, in particular the basis signal contained in the $mathbfU$ needs to be calibrated with the correlations shaped by the the Front-end filter used. The algorithm increased the complexity of the receiver architecture.

Chapter 4 focused on the use of the detector to create a quality index called SQI, for each received signal. This index is composed by several kind of measurements those take into account different conditions like the current output of the MPDD, the C/N_0, etc. Therefore, once we get this complete index, we primarly use it to exclude SV but the problem to have worse GDOP could bring a worst position solution due to the insertion of a geometrical error bigger than the error introduced by the MP. Another possible approach is to try inflate the pseudorange variances, by following a chosen model, for the WLS solution and leave the decision of the exclusion to the RAIM with FDE module.

In future another possible use of the SQI is a sort of environment detector. In fact, by a further statistical characterization, it is possible to select different values of pseudorange variances depending on the value of SQI. This could be useful especially for the land environments. In addition to this, find a link between SQI and the computation of PLs.

In Chapter 5 we presented the TJ algorithm, which is able to detect spoofing attacks and mitigate its effects in a GNSS receiver. Furthermore, the algorithm tries to guarantee the continuity and reliability of the system computing the PVT solution by means of a KF using only Doppler measurements. This technique, implemented in the tracking stage of the software receiver, requires high computational load, so in the list of future work, one of the main focus is the reduction of the computational load.The signal processing part, LASSO,

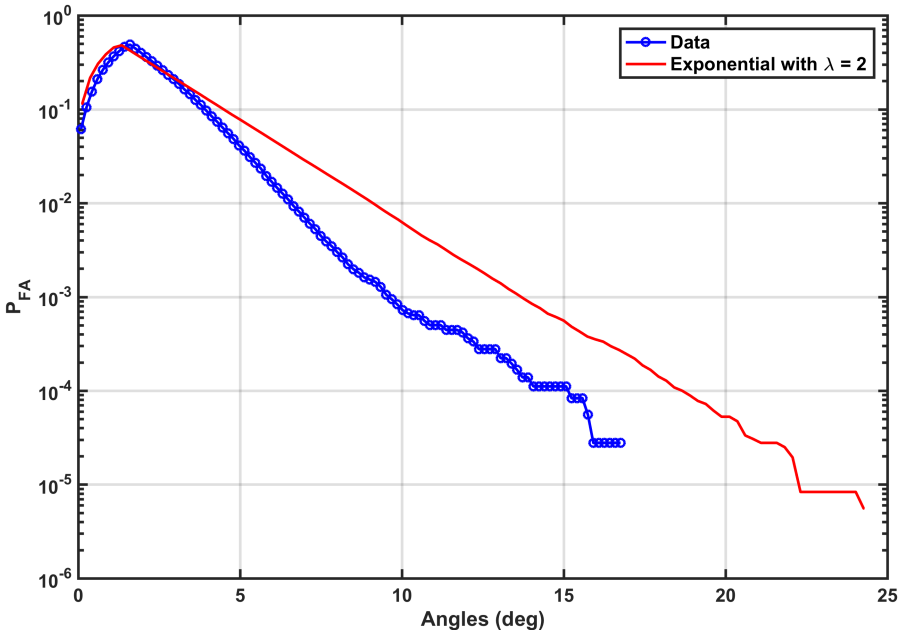

Fig. 6.23 Distributions of the angles between vectors: the circle marker is the empirical distribution from data collection and the continuous line is the exponential distribution with $\lambda = 2$ that overbounds the data.

SQI should be applied to both branches In-Phase and In-Quadrature of the receiver, in order to take into account possible attacks which use relative phase between LOS and spoofer to take control of the receiver while not changing delay or power of the real signal.

The advantages of using decomposition techniques like LAF or LASSO permits to build different decision metric and, in future work, a comparison with new metric will be performed. An example is in Fig. 6.23 where the new metric could be decided by studying the experimental distribution of the angles between the computed vector $\mathbf{w}$ and the $\mathbf{w}_{LOS}$ vector and find a threshold.

Finally in Chapter 6 a simple method to compute the PVT si presented. The method taking into account different test to perform a switch between the KF and LS to reduce the efects of the impairments on the position solution. From the results, this simple algorithms have good performance and the capability to avoid the KF to drift away from the correct solution.

The possible improvement is to optimize the number N_{LSfb} of epochs in which the PVT is computed using LS before switching back to KF. This

number has been set equal to 5 s. In general, if we have both KF and LS solution test statistic at the same time, we could decide to extend N_{LSfb}.

the techniques presented can work with real-time receiver due to the fact that the computational load is sustainable for the current performance of the processors present in the market.

Overall the algorithms presented in this thesis show an evolution from the detection of multipath to the mitigation of its effect in the PVT domain. Some of these techniques are then used to other impairments like spoofing.

References

[1] shift2rail, https://shift2rail.org.

[2] Pratap Misra and Per Enge. Global positioning system: Signals, measurements and performance second edition, 2006.

[3] Elliott D Kaplan and Christopher J Hegarty. *Understanding GPS: principles and applications*. Artech House: Norwood, MA, USA, 2005.

[4] Richard Easton. Who invented the global positioning system?, 2006. online resource: http://www.thespacereview.com/article/626/1.

[5] J. Ventura-Traveset and European Space Agency. *EGNOS: The European Geostationary Navigation Overlay System : a Cornerstone of Galileo*. ESA SP. ESA Publications Division, 2006.

[6] Trilateration. Online resource: http://galleryhip.com/gps-satellite-png.html.

[7] Jaume Sanz, J Juan, and M Hernández-Pajares. GNSS data processing, vol. i: Fundamentals and algorithms. *ESA Communications*, 2013.

[8] ESA. Galileo Begins Servings the Globe. Available at http://www.esa.int/Our_Activities/Navigation/Galileo_begins_serving_the_globe.

[9] U.S. Government. Official u.s. government information about the GPS system. online resource: http://www.gps.gov/systems/gps/control/.

[10] Google opens up GNSS pseudoranges, 2016. Online resource: http://galileognss.eu/google-opens-up-gnss-pseudoranges/.

[11] Navipedia. GNSS signal, 2011. Online resource: http://www.navipedia.net/index.php/GNSS_signal.

[12] K Borre, D.M Akos, N Bertelsen, P Rinder, and S.H. Jensen. A software-defined gps and galileo receiver: a single frequency approach, 2007.

[13] Interface Specification. Navstar gps space segment/navigation user interfaces. Technical report, IS-GPS-200, Rev. D, December 7, 2004, available athttp://www. navcen. uscg. gov/gps/geninfo/IS-GPS-200D. pdf, 2010.

[14] D. V. Sarwate and M. B. Pursley. Crosscorrelation properties of pseudorandom and related sequences. *Proceedings of the IEEE*, 68(5):593–619, May 1980.

[15] GPS Joint Program Office (prepared by ARINC Research). Icd-gps-200 cgps interface control document, 1991.

[16] R. Gold. Optimal binary sequences for spread spectrum multiplexing (corresp.). *IEEE Transactions on Information Theory*, 13(4):619–621, October 1967.

[17] Galileo Open Service, Signal in Space Interface Control Document (OS-SIS-ICD), 2016.

[18] S. Bancroft. An algebraic solution of the gps equations. *IEEE Transactions on Aerospace and Electronic Systems*, AES-21(1):56–59, Jan 1985.

[19] Thomas Pany, B Riedl, J Winkel, T Wórz, R Schweikert, H Niedermeier, S Lagrasta, G López-Risueño, and D Jiménez-Baños. Coherent integration time: the longer, the better. *Inside GNSS*, 4(6):52–61, 2009.

[20] Mohamed Sahmoudi and René Landry Jr. Multipath mitigation techniques using maximum-likelihood principle. *Inside GNSS*, 3(8):24–29, 2008.

[21] Navipedia. Multipath, 2011. Online resource: http://www.navipedia.net.

[22] A. J. Van Dierendonck, P. Fenton, and T. Ford. Theory and performance of narrow correlator spacing in a gps receiver. In *Proceedings of the 1992 National Technical Meeting of The Institute of Navigation*, pages 115–124, San Diego, CA, January 1992.

[23] R. D. J. van Nee. The multipath estimating delay lock loop. In *IEEE Second International Symposium on Spread Spectrum Techniques and Applications*, pages 39–42, Nov 1992.

[24] R. D. J. van Nee, J. Siereveld, P. C. Fenton, and B. R. Townsend. The multipath estimating delay lock loop: approaching theoretical accuracy limits. In *Position Location and Navigation Symposium, 1994., IEEE*, pages 246–251, Apr 1994.

[25] M. Irsigler. *Multipath Propagation, Mitigation and Monitoring in the Light of Galileo and the Modernized GPS*. 2008.

[26] Lawrence R Weill. Multipath mitigation using modernized gps signals: how good can it get? In *ION GPS 2002: 15 th International Technical Meeting of the Satellite Division of The Institute of Navigation*, 2002.

[27] M Fantino, A Molino, and M Nicola. N-gene gnss receiver: Benefits of software radio in navigation. In *Proceedings of the European Navigation Conference-Global*, 2009.

[28] L. Lo Presti, E. Falletti, M. Nicola, and M. T. Gamba. Software defined radio technology for GNSS receivers. In *2014 IEEE Metrology for Aerospace (MetroAeroSpace)*, pages 314–319, May 2014.

[29] M. T. Gamba, M. Nicola, and E. Falletti. Performance assessment of an arm-based dual-constellation gnss software receiver. In *2015 International Conference on Location and GNSS (ICL-GNSS)*, pages 1–6, June 2015.

[30] Karl Kovach. Continuity- the hardest gnss requirement of all. In *ION GPS-98*, pages 2003–2020, 1998.

[31] Washington Y Ochieng, Knut Sauer, David Walsh, Gary Brodin, Steve Griffin, and Mark Denney. Gps integrity and potential impact on aviation safety. *The journal of navigation*, 56(01):51–65, 2003.

[32] Navipedia. Integrity. Online resource: http://www.navipedia.net/index.php/Integrity.

[33] Waas precision approach metrics: Accuracy, integrity, continuity and availability. Online resource: http://waas.stanford.edu/metrics.html.

[34] B. W. Parkinson and J. J. Spilker. *Chapter 5: Receiver Autonomous Integrity Monitoring Global Positioning System: Theory and Applications*. American Institute of Aeronautics and Astronautics, USA, 1996.

[35] Dr Young Lee and C. Lee. Analysis of range and position comparison methods as a means to provide GPS integrity in the user receiver. In *In Proceedings of the Annual Meeting of the Institute of Navigation (ION), Seattle, WA, june 24-26*, pages 1–4, 1986.

[36] BRADFORD W. PARKINSON and PENINA AXELRAD. Autonomous GPS integrity monitoring using the pseudorange residual. *NAVIGATION*, 35(2):255–274, 1988. [CrossRef].

[37] MARK A. STURZA. Navigation system integrity monitoring using redundant measurements. *NAVIGATION*, 35(4):483–501, 1988. [CrossRef].

[38] R. Grover Brown. A baseline GPS RAIM scheme and note on the equivalence of three RAIM methods. *NAVIGATION*, 39(3):301–316, 1992. [CrossRef].

[39] GROVER BROWN and PATRICK Y. C. HWANG. Gps failure detection by autonomous means within the cockpit. *Navigation*, 33(4):335–353, 1986.

[40] R Grover Brown and Paul McBurney. Self-contained gps integrity check using maximum solution separation. *Navigation*, 35(1):41–53, 1988.

[41] Alison K Brown. Receiver autonomous integrity monitoring using a 24-satellite gps constellation. In *Institute of Navigation, Technical Meeting*, pages 256–262, 1987.

[42] Juan Blanch, Alex Ene, Todd Walter, and Per Enge. An optimized multiple hypothesis raim algorithm for vertical guidance. In *in Proceedings of the ION GNSS 2007, Fort*. Citeseer, 2007.

[43] S. Haykin. *Adaptive filter theory*. Prentice-Hall: Upper Saddle River, NJ, USA, 1986.

[44] Mattia Berardo and Letizia Lo Presti. GNSS multipath detector based on linear adaptive filter. In *In Proceedings of the 28th International Technical Meeting of The Satellite Division of the Institute of Navigation (ION GNSS+ 2015), Tampa, Florida*, pages 3077–3083, 2015.

[45] M. Berardo and S. Ugazio. Multipath distance detector algorithm (MPDD): Enhancement and application to galileo signals. In *2016 IEEE Metrology for Aerospace (MetroAeroSpace)*, pages 579–584, June 2016.

[46] S. Ugazio, L. Lo Presti, and E. Falletti. Multipath mitigation using linear adaptive filtering techniques. In *In Proceedings of 26th International Technical Meeting of the Satellite Division of the Institute of Navigation (ION GNSS), Nashville, TN, USA, 16-20 Sep*, 2013.

[47] Xin Chen, F. Dovis, Senlin Peng, and Y. Morton. Comparative studies of GPS multipath mitigation methods performance. *Aerospace and Electronic Systems, IEEE Transactions on*, 49(3):1555–1568, July 2013. [CrossRef].

[48] S. Ugazio and L. Lo Presti. Effects of colored noise in linear adaptive filters applied to GNSS multipath detection. In *In Proceedings of Design and Architectures for Signal and Image Processing (DASIP), Cagliari, Italy, 8-10 October*, pages 126–133, Oct 2013.

[49] S. Ugazio and L. Lo Presti. Effects of noise correlation on least squares filtering in multipath detection for GNSS. In *In Proceedings of the 21st European Signal Processing Conference (EUSIPCO), Marrakech, Morocco, 9-13 Sept.*, pages 1–5, Sept 2013.

[50] Amandeep Singh Sappal Garima Malik. Adaptive equalization algorithms: An overview. *IJACSA*, 2(3):62–67, 2011. [CrossRef].

[51] Monson H. Hayes. *Adaptive Filtering (chapter 9). In Statistical Digital Signal Processing and Modeling*. John Wiley & Sons, Inc., New York, NY, USA, 1st edition, 1996.

[52] E. Falletti, D. Margaria, and B. Motella. Educational library of GNSS signals for navigation. *Coordinates*, pages 30–34, August 2009.

[53] M. Irsigler, J. A. Avila-Rodriguez, and G. Hein. Criteria for GNSS multipath performance assessment. In *Proceedings of the 18th International Technical Meeting of the Satellite Division of The Institute of Navigation (ION GNSS 2005), Long Beach, CA*, pages 2166–2177, Sept 2005.

[54] Stephen Boyd and Lieven Vandenberghe. *Convex optimization*. Cambridge university press: New York, USA, 2004.

[55] Katherine L. Monti. Folded empirical distribution function curves-mountain plots. *The American Statistician*, 49(4):342–345, 1995.

[56] James E Gentle. Computational statistics, 2009.

[57] Sergio Benedetto and Ezio Biglieri. *Principles of Digital Transmission: With Wireless Applications*. Kluwer Academic Publishers, Norwell, MA, USA, 1999.

[58] Mattia Berardo and Letizia Lo Presti. On the use of a signal quality index applying at tracking stage level to assist the raim system of a gnss receiver. *Sensors*, 16(7):1029, 2016.

[59] B.W. Parkinson and J.J. Spilker. *Progress in Astronautics and Aeronautics: Global Positioning System: Theory and Applications*, volume 2. American Institute of Aeronautics & Astronautics, Washington DC, USA, 1996.

[60] R. GROVER BROWN and PAUL W. McBURNEY. Self-contained GPS integrity check using maximum solution separation. *NAVIGATION*, 35(1):41–53, 1988. [CrossRef].

[61] N. A. Tmazirte, M. E. E. Najjar, J. A. Hage, C. Smaili, and D. Pomorski. Fast multi fault detection exclusion approach for gnss integrity monitoring. In *In Proceedings of 17th International Conference on Information Fusion (FUSION), Salamanca, Spain, 7-10 July*, pages 1–6, July 2014.

[62] Frank M Schubert, Jan Wendel, Francis Soualle, Michael Mink, Sébastien Carcanague, Rigas Ioannides, Paolo Crosta, and Massimo Crisci. Integrity of navigation for land users: Study concept and simulator architecture. In *In Proceedings of 7th ESA Workshop on Satellite Navigation Technologies, Navitec 2014, At Noordwijk, The Netherlands, 3-5 December*, 2014.

[63] R Eric Phelts, Todd Walter, and Per Enge. Toward real-time SQM for WAAS: improved detection techniques. In *In Proceedings of the 16th International Technical Meeting of the Satellite Division of the Institute of Navigation (ION GNSS+ 2003), Portland, OR, USA, 23 September*, pages 2739–2749, 2003.

[64] Robert Eric Phelts. *Multicorrelator techniques for robust mitigation of threats to GPS signal quality*. PhD thesis, Stanford University, 2001.

[65] M. Rao and G. Falco. How can pseudorange measurements be generated from code tracking? *Inside GNSS magazine*, 7(1):26–33, 01/2012 2012. [CrossRef].

[66] M. Pini, G. Falco, and L.L. Presti. *Estimation of Satellite-User Ranges Through GNSS Code Phase Measurements (chapter 5). In* Global Navigation Satellite Systems: Signal, Theory and Applications*; Shuanggen Jin.* INTECH Open Access Publisher, Rijeka, Croatia, 2012.

[67] Nguyen Dinh Thuan, Ta Hai Tung, and Lo Presti Letizia. A software based multi-if output simulator. In *In Proceedings of International Symposium of GNSS (IS-GNSS), Kyoto, Japan, 16-19 November*, 2015.

[68] Emanuela Falletti, Marco Pini, and Letizia Lo Presti. Are carrier-to-noise algorithms equivalent in all situations? *INSIDE GNSS*, pages 20–27, 2010. [CrossRef].

[69] Kai Borre. GPS easy suite II, easy13 raim. *Inside GNSS*, 4:48–51, 2009. [CrossRef].

[70] Heidi Kuusniemi and Timo Jokitalo. *Indoor and Weak Signal Navigation (chapter 12). In* GNSS: Applications and Methods*, 1st ed.; S. Gleason and D. Gebre-Egziabher (Eds.).* Artech House: Norwood, MA, USA, 2009.

[71] Heidi Kuusniemi. *User-level reliability and quality monitoring in satellite-based personal navigation.* PhD thesis, 2005.

[72] Variances of GPS phase observations: The sigma-ϵ model. *GPS Solutions*, 2(4), 1999. [CrossRef].

[73] Burkhard Schaffrin. Reliability measures for correlated observations. *Journal of Surveying Engineering*, 123(3):126–137, 1997. [CrossRef].

[74] D. Margaria and E. Falletti. A novel local integrity concept for gnss receivers in urban vehicular contexts. In *In Proceedings of the IEEE/ION Position, Location and Navigation Symposium, Monterey, CA, USA, 5–8 May*, pages 413–425, May 2014.

[75] D. Margaria and E. Falletti. Proof-of-concept of the local integrity approach: Prototype implementation and performance assessment in an urban context. In *In Proceedings of 2015 International Conference on Location and GNSS (ICL-GNSS), Gothenburg, Sweden*, pages 1–6, June 22-24 June 2015.

[76] Jason H. Rife. The effect of uncertain covariance on a chi-square integrity monitor. *NAVIGATION*, 60(4). [CrossRef].

[77] D. A. Sanou and R. Jr. Landry. Analysis of GNSS interference impact on society and evaluation of spectrum protection strategies. *Positioning*, 4(2):169–182, 2013.

[78] F. Dovis, editor. *GNSS Interference Threats and Countermeasures.* GNSS Technology and Applications. Artech House, Norwood, MA, 2015.

[79] Ali Jafarnia-Jahromi, Ali Broumandan, John Nielsen, and Gérard Lachapelle. GPS vulnerability to spoofing threats and a review of anti-spoofing techniques. *International Journal of Navigation and Observation*, 2012, June 2012.

[80] Mark L Psiaki and Todd E Humphreys. GNSS spoofing and detection, 2016.

[81] M. Pini, B. Motella, L. Pilos, L. Vesterlund, D. Blanco, F. Lindstrom, and C. Maltoni. Robust on-board ship equipment: the TRITON project. In *Proceedings of the 10th International Symposium Information on Ships*, Hamburg, Germany, September 2014.

[82] UT Austin Researchers Successfully Spoof an $80 million Yacht at Sea, 2013. Available on line.

[83] T. E. Humphreys, B. A. Ledvina, M. L. Psiaki, B. W. O'Hanlon, and Jr. P. M. Kitner. Assessing the spoofing threat. *GPS World*, 20(1):28–38, January 2009.

[84] T. E. Humphreys, J. A. Bhatti, D. P. Shepard, and K. D. Wesson. The Texas Spoofing Test Battery: Toward a Standard for Evaluating GPS Signal Authentication Techniques. In *Proc. of the 25th Int. Tech. Meeting of The Satellite Division of the Institute of Navigation (ION GNSS 2012)*, Nashville, TN, September 2012.

[85] D. M. Akos. Who's Afraid of the Spoofer? GPS/GNSS Spoofing Detection via Automatic Gain Control (AGC). *Journal of the Institute of Navigation*, 59(4), Winter 2012.

[86] P. Y. Montgomery and T. E. Humphreys and B. M. Ledvina. Receiver-autonomous spoofing detection: experimental results of a multi-antenna receiver defense against a portable civil GPS spoofer. In *Institute of Navigation Int. Tech. Meeting (ITM 2009)*, Anaheim, CA, January 2009.

[87] P. Y. Montgomery, T. E. Humphreys, and B. M. Ledvina. A multi-antenna defense: Receiver-autonomous GPS spoofing detection. *Inside GNSS*, 4(2):40–46, April 2009.

[88] A. Broumandan S. Daneshmand, A. Jafarnia-Jahromi and G. Lachapelle. A low complexity GNSS spoofing mitigation technique using a double antenna array. *GPSWorldMagazine*, 22(12):44 – 46, 2011.

[89] N.A. White, P.S. Maybeck, and S.L. DeVilbiss. Detection of interference/jamming and spoofing in a DGPS-aided inertial system. *Aerospace and Electronic Systems, IEEE Transactions on*, 34(4):1208–1217, Oct 1998.

[90] Peter F. Swaszek, Scott A. Pratz, Benjamin N. Arocho, Kelly C. Seals, and Richard J. Hartnett. GNSS spoof detection using shipboard imu measurements. *Proceedings of the 27th International Technical Meeting of The Satellite Division of the Institute of Navigation (ION GNSS+), Tampa, Florida*, pages 745–758, sep 2014.

[91] P. Papadimitratos and A. Jovanovic. GNSS-based positioning: Attacks and countermeasures. In *Military Communications Conference, 2008. MILCOM 2008. IEEE*, pages 1–7, Nov 2008.

[92] L. Heng, D. B. Work, and G.X. Gao. Cooperative GNSS Authentication. Reliability from Unreliable Peers. *Inside GNSS*, 8(5):70–75, September/October 2013.

[93] H. V. de Castro, G. van der Maarel, and E. Safipour. The Possibility and Added-value of Authentication in future Galileo Open Signal. In *23rd Int. Tech. Meeting of the Satellite Division of The Institute of Navigation*, Portland, OR, September 2010.

[94] Cheng Xi-jun, Xu Jiang-ning, Cao Ke-jin, and Wang Jie. An authenticity verification scheme based on hidden messages for current civilian GPS signals. In *Computer Sciences and Convergence Information Technology, 2009. ICCIT '09. Fourth International Conference on*, pages 345–352, Nov 2009.

[95] A. Jafarnia-Jahromi, A. Broumandan, J. Nielsen, and G. Lachapelle. GPS spoofer countermeasure effectiveness based on signal strength, noise power and C/N0 observables. *International Journal of Satellite Communications and Networking*, 30(4):181–191, 2012.

[96] F. Dovis, X. Chen, A. Cavaleri, and K. Ali. Detection of spoofing threats by means of signal parameters estimation. In *Proc. of the 24th Int. Tech. Meeting of The Satellite Division of the Institute of Navigation (ION GNSS 2011)*, Portland, OR, September 2011.

[97] K. Ali, E. Garbin Manfredini, and F. Dovis. Vestigial signal defense through signal quality monitoring techniques based on joint use of two metrics. In *presented at the Position Location and Navigation Symposium 2014 (PLANS)*, Monterey, CA, May 2014.

[98] E. Garbin Manfredini, F. Dovis, and B. Motella. Signal quality monitoring for discrimination between spoofing and environmental effects, based on multidimensional ratio metric tests. In *Proceedings of the 2015 International Technical Meeting of The Institute of Navigation ION GNSS+ 2015*, Tampa, FL (USA), September 2015. Institute of Navigation.

[99] T. E. Humphreys, B. M. Ledvina, M. L. Psiaki, B. W. O'Hanlon, and Kintner Jr. Assessing the spoofing threat: development of a portable gps civilian spoofer. In *Proc. of the 21st Int. Tech. Meeting of the Satellite*

Division of The Institute of Navigation (ION GNSS 2008), Savannah,GA, September 2008.

[100] Robert Tibshirani. Regression shrinkage and selection via the lasso. *Journal of the Royal Statistical Society. Series B (Methodological)*, 58(1):267–288, 1996.

[101] K. D. Wesson, B. L. Evans, and T. E. Humphreys. A combined symmetric difference and power monitoring GNSS anti-spoofing technique. In *Proceeding of the 1st IEEE Global Conference on Signal and Information Processing*, Austin, TX, December 2013.

[102] Thomas Blumensath and Mike E Davies. Iterative thresholding for sparse approximations. *Journal of Fourier Analysis and Applications*, 14(5-6):629–654, 2008.

[103] Carlos Ramirez, Vladik Kreinovich, and Miguel Argaez. Why ℓ_0 is a good approximation to ℓ_0: A geometric explanation. *Journal of Uncertain Systems*, 7(3):203–207, 2013.

[104] Trevor Hastie, Robert Tibshirani, and Jerome Friedman. *The elements of statistical learning: data mining, inference and prediction*. Springer, 2 edition, 2009.

[105] C. Soussen, J. Idier, Junbo Duan, and D. Brie. Homotopy based algorithms for ℓ_0 -regularized least-squares. *Signal Processing, IEEE Transactions on*, 63(13):3301–3316, July 2015.

[106] Robert Grover Brown and Patrick YC Hwang. *Introduction to random signals and applied Kalman filtering: with MATLAB exercises and solutions*, volume 1. John Wiley and Sons, third edition, 1997.

[107] N.I. Ziedan. *GNSS Receivers for Weak Signals*. Artech House Space Technology and Applications. Artech House, 2006.

[108] Khurram Ali, Xin Chen, Fabio Dovis, David De Castro, and Antonio J. Fernández. Multipath estimation in urban environments from joint gnss receivers and lidar sensors. *Sensors*, 12(11):14592–14603, 2012.

[109] D. M. Franco-Patiño, G. Seco-Granados, and F. Dovis. Signal quality checks for multipath detection in GNSS. In *2013 International Conference on Localization and GNSS (ICL-GNSS)*, pages 1–6, June 2013.

[110] Z. Shengkang, W. Hongbo, Y. Jun, and H. Leiming. GPS short-delay multipath estimation and mitigation based on least square method. *Journal of Systems Engineering and Electronics*, 20(5):954–961, Oct 2009.

[111] Ralf Ziebold, Luis Lanca, and Michailas Romanovas. On fault detection and exclusion in snapshot and recursive positioning algorithms for maritime applications. *European Transport Research Review*, 9(1):1, 2016.

[112] Emanuela Falletti, Marco Rao, and Simone Savasta. *The Kalman Filter and Its Applications in GNSS and INS*, pages 709–751. John Wiley and Sons, Inc., 2011.

[113] X. Tang, G. Falco, E. Falletti, and L. Lo Presti. Practical implementation and performance assessment of an extended kalman filter-based signal tracking loop. In *2013 International Conference on Localization and GNSS (ICL-GNSS)*, pages 1–6, June 2013.

[114] M. Linderoth, K. Soltesz, A. Robertsson, and R. Johansson. Initialization of the kalman filter without assumptions on the initial state. In *2011 IEEE International Conference on Robotics and Automation*, pages 4992–4997, May 2011.

[115] G. Falco, M. Nicola, and E. Falletti. Constellation-aware method for computing the covariance matrix of gnss measurements. In *2016 European Navigation Conference (ENC)*, pages 1–8, May 2016.

[116] Heidi Kuusniemi. *User-Level Reliability and Quality Monitoring in Satellite-Based Personal Navigation*. Tampere University of Technology, 2005.

[117] Andreas Wieser, Mark G Petovello, and Gérard Lachapelle. Failure scenarios to be considered with kinematic high precision relative GNSS positioning. In *Proceedings ION GNSS*, page 6. Citeseer, 2004.

[118] Guochange Xu. *GPS: Theory, Algorithms and Applications*. Springer, 2007.

[119] Andreas Lehner and Alexander Steingass. A novel channel model for land mobile satellite navigation. In *Institute of Navigation Conference ION GNSS*, pages 13–16, 2005.

[120] ITU. Propagation data required for the design of earth-space land mobile telecommunication systems, 2009.

[121] D. Salós, A. Martineau, C. Macabiau, B. Bonhoure, and D. Kubrak. Receiver autonomous integrity monitoring of gnss signals for electronic toll collection. *IEEE Transactions on Intelligent Transportation Systems*, 15(1):94–103, Feb 2014.

[122] E. Falletti, D. Margaria, M. Nicola, G. Povero, and M. T. Gamba. N-fuels and soprano: Educational tools for simulation, analysis and processing of satellite navigation signals. In *2013 IEEE Frontiers in Education Conference (FIE)*, pages 303–308, Oct 2013.

[123] JOHN J. BRAUN KRISTINE M. LARSON, ERIC E. SMALL and VALERY U. ZAVOROTNY. Environmental sensing: a revolutionary in GNSS applications. *Inside GNSS*, July 2014.